Flow and Reactive Transport Processes in Porous Media

by

Emmanuel Adoliwine Amikiya

Thesis presented in partial fulfilment of the requirements for the degree of Master of Science at Stellenbosch University

Department of Mathematical Sciences,
Applied Mathematics Division,
University of Stellenbosch,
Private Bag X1, Matieland 7602, South Africa.

Supervisor: Professor Mapundi K. Banda

December 2013

Declaration

By submitting this thesis electronically, I declare that the entirety of the work contained therein is my own, original work, that I am the owner of the copyright thereof (unless to the extent explicitly otherwise stated) and that I have not previously in its entirety or in part submitted it for obtaining any qualification.

Signature: .....

Emmanuel Adoliwine Amikiya

Date: December 2013

Abstract

Flow and Reactive Transport Processes in Porous Media

Emmanuel Adoliwine Amikiya

Department of Mathematical Sciences,

Applied Mathematics Division,

University of Stellenbosch,

Private Bag X1, Matieland 7602, South Africa.

Thesis: MSc

December 2013

Flow and reactive transport of chemical species is a very common phenomenon that occurs in natural and artificial systems. However in this study, the topic is related to acid mine drainage in the South African mining environment. Due to the hazards associated with acid mine drainage, prevention or treatment of mine effluent water before discharging to receiving waters and other environments is a necessity. A new time-dependent mathematical model is developed for a passive treatment method, based on multi-scale modelling of the coupled physico-chemical processes such as diffusion, convection, reactions and filtration, that are involved in the treatment process. The time-dependent model is simulated on a two-dimensional domain using finite volume discretization to obtain chemical species distributions.

Uittreksel

Vloei en Reagerende Transportproses in Poreuse Media

*("**Flow and Reactive Transport Processes in Porous Media**")*

Emmanuel Adoliwine Amikiya

Departement Wiskundige Wetenskappe,
Afdeling Rekenaarwetenskap,
Universiteit van Stellenbosch,
Privaatsak X1, Matieland 7602, Suid Afrika.

Tesis: MSc

Desember 2013

Vloei en reagerende transport van chemiese spesies is 'n baie algemene verskynsel wat in natuurlike en kunsmatige stelsels plaasvind. In hierdie studie is die onderwerp egter verwant aan suurmyndreinering in die Suid-Afrikaanse mynbou-omgewing. As gevolg van die gevare wat verband hou met suurmyndreinering, is die voorkoming of die behandeling van die afval-mynwater voor dit in opvangswaters en ander omgewings beland 'n noodsaaklikheid. 'n Nuwe tydafhanklike wiskundige model vir 'n passiewe behandelingsmetode is ontwikkel. Dit is gebaseer op die multi-skaal modulering van gekoppelde fisies-chemiese prosesse soos diffusie, konveksie, reaksies en filtrasie, wat by die behandelingsproses betrokke is. Die tydafhanklike model word gesimuleer op 'n twee-dimensionele domein met behulp van eindige volume diskretisasie om die verspreiding van chemiese spesies te bepaal.

Acknowledgements

I would like to express my sincere gratitude to the following people and organisations ...

Prof. Mapundi K. Banda

Prof. Franscois Smit

Dr. Maret Cloete

Dr. Sonia Woudberg

Miss Azra Adams

Mr. Ocansey Evans Doe

Marina Van Heyningen

Mr. Amoaku Gordon

Mr. Tshokotsha Mvuyisi Humphrey

Mr. Nbiyanvanga Mamana

AIMS.

Dedications

This document is dedicated to Akolgo Amaliyinga Augustina Amikiya

Contents

List of Figures

List of Tables

Nomenclature

Constants

$g = 9.81\,\mathrm{m/s^2}$

$\pi = \frac{22}{7}$

Scalar variables

C_k	Mass concentration of chemical species	$[\mathrm{g/m^3}]$
n_c	Particle number concentration	$[\mathrm{m^{-3}}]$
P_O	Partial pressure of oxygen	$[\mathrm{atm}]$
T_s	Temperature of limestone	$[^{\circ}\mathrm{C}]$
P_{CO_2}	Partial pressure of carbon dioxide	$[\mathrm{atm}]$
T_e	Temperature of effluent water	$[^{\circ}\mathrm{C}]$
Φ, ϕ	Generalized scalar variables	$[\,]$
R_{CaCo_3}	Rate of calcite dissolution	$[\mathrm{mol/m^3 s}]$

Vectors and Tensors

$\mathbf{v_e}$	Microscopic velocity of effluent water	$[\mathrm{m/min}]$
$\mathbf{v}$	Macroscopic velocity of effluent water	$[\mathrm{m/min}]$

$\bar{\mathbf{D}}$	Dispersion tensor	[ ]
$\bar{\sigma}$	Stress tensor	[ ]
δ	Identity tensor	[ ]
$\bar{\tau}$	Viscous stress tensor	[ ]

Parameters

K_{H^+}	Neutralization constant	$[\mathrm{min}^{-1}]$
K_{Ca^+}	Precipitation constant	$[\mathrm{m}^3/\mathrm{mol\ min}]$
K_{sp}	Pure calcite dissolution-precipitation equilibrium constant	[ ]
K_{eq}	Dissolution-precipitation equilibrium constant	[ ]
η_{Ca^+}	Calcium ion activity coefficient	[ ]
η_{H^+}	Hydrogen ion activity coefficient	[ ]
$\eta_{HCO_3^-}$	Hydrocarbonate ion activity coefficient	[ ]
θ_f	Favourable fractional surface coverage	[ ]
θ_u	Unfavourable fractional surface coverage	[ ]
ε_f	Porosity	[ ]
K_{dep}	Deposition rate constant	$[\mathrm{min}^{-1}]$
ρ_e	Microscopic density of effluent water	$[\mathrm{g/m}^3]$
$\rho_s,\ \rho_l$	Microscopic density of limestone	$[\mathrm{g/m}^3]$
$(Cp)_e$	Specific heat capacity of effluent water	[J/KgC]
$(Cp)_s$	Specific heat capacity of limestone	[J/KgC]

Other symbols

$\langle\rangle$	Superficial average
$\langle\rangle^f$	Intrinsic phase average
RHS	Right hand side
AMD	Acid mine drainage

Subscripts

u	Unfavourable
f	Favourable
k, i	Chemical species
l	Limestone
p	Particle
c	Concentration
e	Effluent water
s	Solid phase

Chapter 1

Introduction to Acid Mine Drainage

Acid mine drainage (AMD) refers to a pollutant that is generated in abandoned mines by the oxidation of sulphur minerals, and enters the environment as polluted water [4]. The polluted water generally consist of an acid, dissolved metals including Aluminium (Al), Mercury (Hg) and Manganese (Mn) and other chemical compounds [54, 4, 63].

Mostly, AMD is generated by the oxidation of sulphur minerals that have been exposed to air and water, by mining activities [54, 4, 63]. The most common sulphur mineral is pyrite (FeS_2). This mineral is available on the earth's surface but in smaller quantities, thus due to the limited quantities, it is consumed in reactions in a short time [54, 4, 63]. The amount of acid produced is not enough to result in a hazardous pollutant [54, 4, 63].

However, in the mining environment and during mining processes, rocks are crushed resulting in the exposure of more pyrite [54, 4, 63]. When it rains or when water is supplied, chemical reactions take place and more acid is produced, thus resulting in a highly concentrated acid.

The high concentration of the acid allows the water to dissolve more chemical metal-containing minerals [54, 4, 63]. The dissolution of the water-soluble metal-containing minerals releases metallic ions into the acidic water, thus causing further contamination. Formation of acid and subsequent pollution of water caused by crushed rocks at the surface of the earth is commonly called acid rock drainage (ARD) or acid mine drainage (AMD) [54, 4, 63].

Moreover, as mining continues more rocks are crushed and deep vertical voids, long horizontal voids or large shallow voids called mines are created within the earth. These openings are filled with air and exposed to water sources. The surfaces or walls of the openings contain pyrite in larger quantities as compared with the quantity on the earth's surface, thus with the availability of water from rain or dew, reactions occur along the walls of the mines, resulting in the production of a high concentrated contaminant. Figure 1.1 is a picture of a typical large-scale mine where the mineral of interest is distributed widely in shallow depths. Highly efficient machines are used for large-scale mining in such places where the mineral of interest is distributed widely in shallow depths. These machines create large shallow voids that can store large quantities of water.

Figure 1.1: A picture of a typical large-scale mine [63].

Moisture and air within the mines are the cause of the reactions which lead to the con-

taminant production. When the mines are full during heavy rains or due to water supplied from other sources, some of the contaminants that are less dense than water are transported to the earth's surface and even transported further away from the mining environment by run-off. Figure 1.2 shows a mine that is almost filled with contaminated water. It can also be observed in Figure 1.2 that the sludge is not separated from the water by sedimentation. This implies that the density of the sludge (colloidal particles) is not greater than that of water.

Figure 1.2: A mine filled with acid mine drainage. The source of this picture is [63].

The contaminants carried from the production region reduces in concentrations as the flow and transportation take place. The reduction in concentration are due to physical and chemical processes such as filtration, deposition or chemical transformation. From the pictures in Figure 1.3, it can be observed that the sludge (metal precipitates) have been deposited along the drain (flow domain).

Figure 1.3: Pictures showing deposited contaminants along drains.

Figure 1.4: Pictures showing environmental hazards caused by AMD. The source of these pictures is [63].

AMD is really a serious environmental problem that can affect every life on earth. It is produced in one area and spread to other areas. As the acid has a corrosive effect, the hard metals dissolved by the acid are toxic to living organism [54]. If the acid water drains into surface streams or the biotic environment, there would be a very great ecological impact, including those shown in Figure 1.4 [63]. The pictures shown in Figure 1.4 show simple

effects of mine effluent water on the vegetation. One of the effects of mine effluent water which affects human life directly is the pollution of water bodies that provide portable water for human consumption.

Deposits of the precipitates (sludge) also "*jeopardize the integrity*" of urban infrastructure [63]. Figure 1.5 shows a decant of the contaminant. When the situation in Figure 1.5 occurs in settlements, the beautiful appearances of houses, stadia, parks and gardens will be destroyed.

Figure 1.5: A picture showing deposited contaminants. The source of this picture is [63].

Due to the hazardous nature of this pollutant efforts are made to prevent its occurrence or treat the mine effluent water. South Africa is currently facing AMD problems in some of its mining sites including Mpumalanga and KwaZulu-Natal Coal fields, Witwatersrand fields and O'Kiep Copper district [63].

As a matter of urgency, a team of experts was set-up to assess the problem and provide efficient solution measures [63]. The team of experts assessed the potential risks associated with the AMD problem and identified mine flooding to have potential of causing;

- Contamination of shallow groundwater resources, which is required for human consumption and Agricultural purpose [63].
- *"Geotechnical impacts, such as the flooding of underground infrastructure in areas where water rises close to urban area"* [63].
- *"Increased Seismic activity which could have a moderate localised effect on property and infrastructure"* [63].

The team also identified *"decant of AMD to the environment"* to have a potential of causing:

- *"Serious negative ecological impacts"* [63].
- *"Regional impacts on major river systems"* [63].
- *"Localised flooding in low-lying areas"* [63].

The team of experts proposed a management approach which includes prevention and management of the decant, using ingress control measures and treating the effluent water [63].

Prevention and management of the decant involves preventing the mines from filling up. Keeping the mines partially full will prevent the transportation and deposition of contaminants to other environments including settlements. The team also stated that the source of water does not come from rain only, but *"groundwater seeping into the workings, surface streams that lose water to shallow mine workings, open surface workings, seepage from mine residue deposits and losses from water, sewage and storm-water reticulation systems"* [63]. Creating canals to redirect surface waters, and sealing of mine-cracks are ingress control methods [63].

The team also mentioned that even if all ingress control and preventive measures are implemented AMD will still occur in the mines. Therefore, treatment of the effluent water is a necessity. Treatment of the effluent water involves neutralizing the acid, precipitating the ferrous ions and other metals present. Treatment methods can be classified into active, passive, or *"in situ"* [63].

The team of experts provided many recommendations in their report, one of them is neutralization of effluent water pumped out of mines. The process of neutralization should also address high iron and other metal concentrations [63]. The treatment process that is recommended by the team, is a passive treatment method called Open Limestone Channel (OLC) treatment.

In our study, we provide a mathematical model that accounts for the flow and reactive transport of the contaminants in the open limestone channel treatment method. The goal of our study is to derive a model that can predict spatial distributions of the contaminants and the change in species concentrations with time. Mathematical modelling of the phenomenon is based on multi-scale modelling. Our model consists of a system of partial differential equations that represent energy, chemical species and momentum transport equations. The following simplifying assumptions are used:

1. The flow domain is limestone.
2. The density, viscosity and specific heat capacity for the carrier fluid are used to approximate corresponding parameters for effluent water, and are considered constant.
3. The limestone is homogeneous, isotropic, and has constant parameters.
4. The flow is single-phase, incompressible and in the laminar regime. There is no-slip at the fluid-solid interface.
5. In the flow domain, the pH of the effluent water is less than 3.5.

In Chapter 1, a brief introduction to acid mine drainage is provided. A summary of a report written by a team of experts on the state of South Africa with regards to the

acid mine drainage problem is also provided. The goal of the study and some simplifying assumptions are introduced.

In Chapter 2, the composition of mine effluent water is ascertained from a review of pyritic systems. Physical and chemical processes in the passive treatment method called open limestone channel (OLC) is discussed. Kinetic data (required for closure of the model in Chapter 3 is obtained from a review of literature.

In Chapter 3, the continuum approaches for modelling fluid flows on and through materials are used to derive a system of partial differential equations. A complete model is obtained by closure of the partial differential equations with kinetic data that resulted from discussions on chemical kinetics of calcite dissolution, oxidation of ferrous ions and filtration.

In Chapter 4, the finite volume discretization method is used to discretize the partial differential equations on a rectangular domain. Central differencing, Upwind and hybrid schemes are used for approximating the coefficients in the linear systems. The finite difference scheme is used to obtain implicit and explicit time marching schemes.

In Chapter 5, numerical schemes are verified by comparing solutions obtained by the central differencing, upwind and hybrid schemes to an analytical solution. The code used for our experiments is validated by three test examples. Numerical experiments are carried out for coupled uniform flow, energy and contaminant transport. The investigations are based on Peclet number.

We conclude our discussion in Chapter 6 based on our results. A recommendation is also provided based on our results. Future research topics are provided.

Chapter 2

Chemical Kinetics in AMD Generation and Treatment

In this Chapter, we review literature on the chemical processes that are involved in acid mine drainage. The kinetics of pyritic oxidation which lead to AMD is provided in the first paragraph. Treatment methods for contaminated water are discussed in the second paragraph, and chemical reactions involved in the treatment method are discussed.

2.1 Oxidation of pyrite

Pyrite is among the most common reactive sulphite minerals found on the earth's surface [33, 15]. Weathering of this mineral contributes to electron cycling [33, 15] and the resulting current from the electron cycling is often used to derive processes such as formation of acid mine drainage [33, 45, 15], mobilization and redox cycling of metals in sediments from mining and other environments [33, 40, 66, 2], degradation of pollutants [33, 52], reduction of aqueous trace metal complexes to form ore deposits [33, 17, 32], nutrient and metal cycling at oxic-anoxic boundaries on lake bottoms and in estuaries [33, 67]. The oxidation of pyrite has special importance in technological applications ranging from hydrometallurgy [33, 39] to solar energy conversion [33, 22].

Oxidation of pyrite takes place in moist air and oxygenated aqueous solutions. When pyrite is exposed to moist air, the oxidation that occurs is called atmospheric oxidation, and when the oxidation occurs in a solution, it is called aqueous oxidation [47, 13]. A review of the atmospheric and aqueous oxidation is given in [47, 13]. The major oxidation product in the oxidation reaction is sulphate ions. Iron oxy-hydroxide ($FeOOH$), iron hydroxide ($Fe(OH)_3$) and iron oxide (FeO) are other products from the atmospheric oxidation [47, 62].

The oxidation of pyrite is a complicated chemical process that has not yet been understood very well. The products of oxidation vary from one pyritic system to another due to varying environmental and reaction conditions [47]. The mineral pyrite occurs naturally in varieties, which undergo different oxidation processes [15, 55]. While some researchers in [15] are of the view that the oxidation is an electrochemical process, other researchers [50, 47] are of the view that the oxidation is a chemical-controlled process. Despite the diverging view-points, the oxidation of pyrite can be explained by four chemical reactions that appear in most of the studies related to pyritic oxidation or acid mine drainage. These chemical reactions include [54, 18, 16]:

- Oxidation of pyrite by oxygen which occurs by the chemical Equation 2.1.1;

$$2FeS_{2(s)} + 7O_{2(g)} + 2H_2O_{(l)} \longrightarrow 2{Fe^{2+}}_{(aq)} + 4{SO_4^{2-}}_{(aq)} + 4{H^+}_{(aq)}. \tag{2.1.1}$$

- Oxidation of ferrous ions which occurs by the chemical Equation 2.1.2;

$$4{Fe^{2+}}_{(aq)} + 4{H^+}_{(aq)} + O_{2(g)} \longrightarrow 4{Fe^{3+}}_{(aq)} + 2H_2O_{(l)}. \tag{2.1.2}$$

- Precipitation of iron hydroxide which occurs by the chemical Equation 2.1.3;

$${Fe^{3+}}_{(aq)} + 3H_2O_{(l)} \longrightarrow {Fe(OH)_3}_{(s)} + 3{H^+}_{(aq)}. \tag{2.1.3}$$

- Oxidation of pyrite by ferric ions which occurs by the chemical Equation 2.1.4;

$$FeS_{2(s)} + 14Fe^{3+}{}_{(aq)} + 8H_2O_{(l)} \longrightarrow 15Fe^{2+}{}_{(aq)} + 2SO_4^{2-}{}_{(aq)} + 16H^{+}{}_{(aq)}. \quad (2.1.4)$$

The generalized reaction pathway given by chemical Equations 2.1.1 to 2.1.4 is a summary of overall chemical reactions that are identified in any pyritic system, but not a set of elementary reactions as expected in any reaction mechanism [18]. Thus the individual reactions in the pathway may occur as reaction mechanisms depending on the reaction environmental conditions [18].

Moreover, according to [8, 47, 13, 62] and from the generalized oxidation reaction pathway, the major oxidants in pyritic systems are ferric ions and oxygen. Oxidation of pyrite by ferric ions is slow as compared with the oxygen oxidation, but the presence of *Thiobacillus ferrooxidan* can greatly increase the rate of ferric ion oxidation [18, 34, 1]. Since the bacteria present depends on oxygen and also, since ferric ions do not occur naturally as with oxygen, then the initiator and sustainer of the pathway is the oxygen oxidation of pyrite which is given by chemical Equation 2.1.1 [18, 50, 16].

According to [18], the location of pyrite determines whether the given chemical reaction 2.1.1 can occur or not, and how fast the reaction will occur. It is argued in [18] that, if the pyrite is immersed in deep water where there is no oxygen then oxygen supply to the surface of the pyrite will not be possible. The recorded cases of pyritic oxidation are gob piles, strip pits, spoil banks and underground mines. These examples provide supporting evidence that pyritic oxidation by oxygen is vital for sustaining the oxidation pathway [18]. The air circulation in such pyritic systems is suitable and fairly consistent, thus reaction 2.1.1 will always occur as long as water and pyrite is available.

After the oxygen oxidation reaction given by Equation 2.1.1 has occurred, excess water supplied (by rain, seepage and rivers) to the reaction environment washes the oxidation products (and other metals present) to form a solution. A fraction of the ferrous ions produced in the pyritic oxidation are oxidized by oxygen to form ferric ions when the pH is below three (3), chemical complexes or Ligands [16, 4]. The oxidation of ferrous ions is given by chemical Equation 2.1.2. Many researchers [18, 33, 10, 3, 54] predict this reaction step as the slowest, thus implying the rate-determining step in the generalized

pathway. This reaction step can be catalysed by *Thiobacillus ferrooxidans*, which survives in a very acidic solution (pH less than 2) [16, 18, 54]. The abiotic oxidation of ferrous ion to ferric iron is dominant at higher pH values [16, 18, 4].

The major product from the ferrous oxidation reaction given by Equation 2.1.2 is ferric ions. This product also undergoes reaction in two ways depending on the pH of the solution [59, 54, 16, 4]. It forms iron hydroxide precipitates when the pH of the solution is greater or equal to 3.5 [4, 16, 54]. The chemical equation describing the formation of iron hydroxide is Equation 2.1.3. For greater pH values (pH greater than 3.5), the ferrous oxidation product is iron hydroxide instead of ferric ions given by chemical Equation 2.1.2.

Another chemical reaction involving ferric ions is the oxidation of pyrite to form ferrous ions, sulphate ions and hydrogen ions (H^+) [4, 16, 47]. This reaction is parallel to the precipitation reaction given by Equation 2.1.2. The chemical equation describing the ferric ion oxidation of pyrite is Equation 2.1.4.

The degree to which mine waters are polluted depends on the quantity of pyrite that has been oxidized, and the rate of pollution of mine waters depends on the rate of oxidation of pyrite. In addition to the rate of oxidation of pyrite, the rate of generation of AMD depends on the presence or absence of acid neutralising minerals [18]. The contaminants in mine effluent water are the products of pyritic oxidation and chemical metals from dissolved minerals, however in our discussion, the effluent water contaminants are oxidation products from the generalized reaction pathway only. Table 2.1 contains the chemical species in the mine effluent water.

Index (k)	1	2	3	4	5	6	7	8
Species	H^+	Fe^{3+}	Fe^{2+}	$Fe(OH)_3$	SO_4^{2-}	Ca^{2+}	O_2	HCO_3^-
Concentration (C_k)	C_1	C_2	C_3	C_4	C_5	C_6	C_7	C_8

Table 2.1: A table of chemical species involved in AMD.

2.2 Effluent water treatment

Treatment methods for mine effluent water can be categorized as active or passive methods [25]. The generalized procedure for treating effluent water consists of three physico-chemical unit operations such as neutralization of acid, oxidation of iron and sludge removal [9].

The active treatment method involves adding neutralizing agents directly to polluted water bodies. The active treatment method requires monitoring and sophisticated equipment. It is also not an efficient method for metal removal. In addition it is expensive. Therefore, budget reduction, equipment failure and changes in weather conditions could result in serious problems (e.g kill fish) [25].

The passive treatment method combines many pH-raising techniques and metal removal techniques. The pH raising techniques involve using chemicals such as limestone or lime, and using bacteria to raise the pH of effluent water. It is expensive to initiate but not operation-intensive as compared with active treatment [25]. The passive treatment method may involve periodic maintenance [25]. There are many passive treatment methods, however, each method has its advantages and disadvantages. Some of the passive treatment methods include limestone dumping, limestone dosing, anoxic limestone drain (ALD), anaerobic Wetland, aerobic wetland successive alkalinity producing systems (SAPS), leach bed and open limestone channel (OLC) [25].

Among the passive treatment methods, Open Limestone Channel is of interest in our study. The open limestone channel treatment method involves allowing the effluent water to flow through a drain containing limestone [25]. This method is very convenient at undulating locations where natural gradients exist (e.g hills, mountains) [25]. It is convenient for removing chemical metals and raising the pH of the effluent water. It is designed in a special way to allow oxygen supply to the effluent water and to sustain acid neutralization [25]. Figure 2.1 contains pictures of limestone drains. The chemical and physical processes that occur in the open limestone channel treatment include oxidation of iron, neutralizing of acid and filtration. Kinetic data related to these physical and chemical processes is required in our modelling study. Such information is usually deter-

mined by laboratory experiments. However, we review literature in the following sections of this Chapter to obtain the kinetic data.

Figure 2.1: Open limestone channels for treating mine effluent water [49].

2.3 Oxidation of ferrous ions in aqueous solution

Oxidation of metallic ions is an important chemical reaction in nature and chemical technological applications (including water-treatment) [59]. A review of studies conducted on the oxidation process is given by [58]. According to [58, 59], the oxidation of iron has been extensively studied in homogeneous solutions containing acids.

The extensive studies have yielded valuable information with regards to the reaction mechanism between ferrous ions and oxygen, but have not yielded information that specifically applies to bicarbonate-containing water (water containing CO_3^{2-} compounds or ions) [58].

A sequence of steps by which the oxidation of ferrous iron proceeds was suggested in 1935, these steps include [58]:

$$Fe^{2+} + O_2 \leftrightarrows Fe^{3+} + HO_2 \tag{2.3.1}$$

$$Fe^{2+} + HO_2 \longrightarrow Fe^{3+} + H_2O_2, \tag{2.3.2}$$

$$Fe^{2+} + H_2O_2 \longrightarrow Fe^{3+} + HO + H_2O, \tag{2.3.3}$$

$$Fe^{2+} + HO \longrightarrow Fe^{3+} + H_2O. \tag{2.3.4}$$

By observing the chemical Equations 2.3.1 to 2.3.4, it can be noticed that the reactions are not balanced with respect to hydrogen ions. The reason for the omission is that, the objectives of the researchers at that time (1935), did not include dependence of the oxidation process on hydrogen ions [58]. The rate determining step was predicted to be reaction 2.3.1, and the oxidation rate was predicted to be first order with respect to Fe^{2+} ion concentration or dissolved oxygen concentration. The rate law for reaction 2.3.1 is given by:

$$\frac{d[Fe^{2+}]}{dt} = -K_o[Fe^{2+}]P_{O_2}. \tag{2.3.5}$$

where K_o is the rate constant for the reaction and P_{O_2} is the partial pressure of oxygen.

Moreover, the rate of a reaction depends on environmental factors. One of the environmental factors that affects ferrous ion oxidation is the nature of anions present in the solution. According to [58], the rate of oxidation increases proportionally to increasing affinity of the anions for ferric ions [58]. The rate of ferrous oxidation has been measured in experiments involving different anions in acidic solutions. According to [58], results show a decreasing rate in sulphate and hydroxide solutions. The rate law 2.3.5 does not apply in a solution containing perchlorate and sulphate ions [58]. It has been determined by experiment that there is a second order dependence on the ferrous ion concentration in an acidic solution containing sulphate ions [58, 59, 20]. The second order rate law is given by [14, 61]:

$$\frac{d[Fe^{2+}]}{dt} = -K_o[Fe^{2+}]^2P_{O_2}. \tag{2.3.6}$$

In addition to anions, substances that catalyse decomposition of anions especially peroxides in the presence of charcoal, ferrous iron-platinum, and cupric salts, increase the rate of oxidation [58].

Another environmental factor is the pH of the aqueous solution. In very acidic media the rate of ferrous oxidation does not depend on the pH of the solution [14, 59]. However, the rate of oxidation depends strongly on pH in less acidic media. At neutral pH, the rate of oxidation is given by:

$$\frac{d[Fe^{2+}]}{dt} = -K_o[Fe^{2+}]P_{O_2}[H^+]^{-2}. \tag{2.3.7}$$

In bicarbonate solutions, the rate of iron oxidation is affected by solubility of ferrous and ferric iron [58]. Ferrous compounds are observed in experimental studies to be more soluble than ferric compounds [58], based on this observation it has been proposed that $Fe(OH)_{3(s)}$ co-exist with aqueous $Fe(OH)_3$ [58]. Experimental results confirmed that during the oxidation process, colloidal ferric hydroxide is formed under suitable conditions but do not have any effect on the rate of oxidation [58]. In bicarbonate solutions, the rate of ferrous iron oxidation is given by [58]:

$$\frac{d[Fe^{2+}]}{dt} = -K_o[Fe^{2+}]P_{O_2}[OH^-]^2, \tag{2.3.8}$$

where $[OH^-]$ is concentration of hydroxyl (OH^-) ions in the solution.

Furthermore, catalysts especially Cu^{2+} and anions which form complexes with ferric ions are observed to increase the rate of oxidation significantly, while small concentrations of Fe^{3+}, and SO_4^{2-} have no effect on the reaction rate [58].

From the discussion in this section, one can conclude that the oxidation of ferrous ion is a complicated chemical process. The effluent water is an acidic medium, thus the rate law given by Equations 2.3.5 and 2.3.6 could be used to describe the ferrous oxidation process in the effluent water. However, since the limestone is an alkaline medium and the flow occurs through it, then the rate law given by Equation 2.3.7 could also be used to approximately describe the ferrous oxidation process. None of the three rate laws 2.3.5, 2.3.6 and 2.3.7 provides an exact description to the problem under investigation.

A mathematical model for a passive treatment method is proposed by [20]. The model applies to a case where the effluent water flows on a limestone bed. According to [20], the oxidation of ferrous ions to ferric ions is a reversible reaction which results in the production of hydrogen ions. Thus the water becomes more acidic when ferrous oxidation

occurs. A generalized rate law for ferrous oxidation reaction in mine effluent water has been proposed by [20]. This generalized reaction rate law is given by [20]:

$$I_b = S_3 = -k_{fR} C_3^4 C_1^4 P_{O_2} + k_{bR} C_2^4, \tag{2.3.9}$$

where k_{fR}, k_{bR} are, respectively, the forward and backward reaction rate constants.

This rate law 2.3.9 may be a better choice for our study, however, its high order and dependence on four variables makes it complicated and expensive for computational reasons. As part of simplicity, we choose the rate law 2.3.5 for our study. The species concentrations in the rate law 2.3.9 are measured in moles per unit volume, however, we will use mass concentration in this work. Thus we convert the molar concentration in 2.3.9 to mass concentration by dividing the molar concentration of each species by its molecular weight. The partial pressure is expressed in concentration by using Henry's constant. Rearanging the results, we obtain:

$$S_3 = \frac{dC_3}{dt} = -K_o C_3 C_7, \tag{2.3.10}$$

where K_o includes Henry's constant.

2.4 Formation of ferric ions

With reference to chemical Equation 2.3.2, the stoichiometric ratio of ferrous to ferric ions is one to one. Thus the rate of formation of ferric ion is equal and opposite to the rate of oxidation of ferrous ions. Thus we obtain:

$$S_2 = \frac{dC_2}{dt} = -\frac{dC_3}{dt} = K_o C_3 C_7. \tag{2.4.1}$$

2.5 Rate of oxygen consumption

With reference to chemical Equation 2.3.2, the stoichiometric ratio of ferrous to oxygen is one to four. Thus the rate of oxygen consumption is equal one-fourth of the rate of

ferrous oxidation. Thus we obtain:

$$S_7 = \frac{dC_7}{dt} = -0.25K_oC_3C_7. \tag{2.5.1}$$

2.6 Filtration of $Fe(OH)_3$

$Fe(OH)_3$ is described by [58] as colloidal. Thus in this section, we discuss filtration models for colloids that will be used later in our transport model.

Physical and chemical heterogeneities of the transporting medium greatly affect the filtration process [44]. The rate of filtration of colloids is expressed in number concentration by [44]:

$$\frac{\partial n_c}{\partial t} = -\frac{\theta_L}{\pi d_p^2}\frac{\partial \theta}{\partial t}, \tag{2.6.1}$$

where n_c is the colloidal particle-number concentration, d_p is the radius of the colloidal particle, t is time, and θ is the fractional surface coverage of the colloidal particles. Deposition of the colloidal particle can occur at favourable and unfavourable parts of the collector (grain of limestone). A patch-wise model that accounts for deposition at favourable and unfavourable parts is given by [44]:

$$\frac{\partial \theta}{\partial t} = \lambda_L\frac{\partial \theta_f}{\partial t} + (1-\lambda_L)\frac{\partial \theta_u}{\partial t}, \tag{2.6.2}$$

where θ_u, θ_f represent unfavourable and favourable fractional surface coverages on the collector. λ_L is a parameter that accounts for chemical heterogeneity.

The rate of deposition or release at the favourable and unfavourable parts of the collector are given by [44]:

$$\frac{\partial \theta_f}{\partial t} = \pi d_p^2 K_{dep,f} n_c \mathcal{B}(\theta_f) - K_{det,f} n_c \mathcal{R}(\theta_f), \tag{2.6.3}$$

and

$$\frac{\partial \theta_u}{\partial t} = \pi d_p^2 K_{dep,u} n_c \mathcal{B}(\theta_u) - K_{det,u} n_c \mathcal{R}(\theta_u). \tag{2.6.4}$$

Subscripts f, u indicate favourable and unfavourable, K_{dep}, K_{det} represent colloid deposition and release rate constants, and $\mathcal{B}(\theta), \mathcal{R}(\theta)$ represent dynamic blocking and release functions defined by [44]:

$$\mathcal{B}(\theta) = 1 - a_1\left(\frac{\theta}{\theta_{max}}\right) + a_2\left(\frac{\theta}{\theta_{max}}\right)^2 + a_3\left(\frac{\theta}{\theta_{max}}\right)^3, \tag{2.6.5}$$

where θ_{max} is the maximum attainable surface coverage. The dynamic blocking function accounts for the effects of deposited colloids on the rate of deposition [44]. The coefficients a_1, a_2, a_3 must be determined empirically or theoretically [44].

The deposition rate constant is a function of single-collector efficiency, defined by [44]:

$$K_{dep} = \frac{\alpha_f \eta_0 \varepsilon_f \mathbf{v}}{4}, \tag{2.6.6}$$

where α_f is the collision efficiency, ε_f is the porosity of limestone, $\mathbf{v}$ is the velocity of the colloidal particle and η_0 is the favourable single-collector efficiency.

We take the chemical heterogeneity parameter as one (i. e. $\lambda_L = 1$) and assume that there is no particle release after deposition. Thus the resulting Equations 2.6.2 and 2.6.3 are combined to obtain:

$$\frac{\partial \theta}{\partial t} = \pi d_p^2 K_{dep,f} \mathcal{B}(\theta_f) n_c. \tag{2.6.7}$$

Substituting 2.6.7 into Equation 2.6.1, we obtain:

$$\frac{\partial n_c}{\partial t} = -\theta_L K_{dep,f} \mathcal{B}(\theta_f) n_c. \tag{2.6.8}$$

Furthermore, we convert the number concentration (n_c) into mass concentration (C_4) by multiplying Equation 2.6.8 by the mass of colloidal particles. Thus we obtain:

$$S_4 = \frac{\partial C_4}{\partial t} = -\theta_c \theta_L K_{dep,f} \mathcal{B}(\theta_f) C_4, \tag{2.6.9}$$

where θ_c is a coupling parameter for measuring the surface area available for $Fe(OH)_3$ attachment.

2.7 Calcite dissolution and precipitation

Limestone is an aggregate of many chemical compounds but the dominant compound is calcite. In our discussion, we assume that the limestone consist of calcite only, this assumption conforms to the homogeneity assumption of the flow domain. When the acidic water passes through limestone, the calcite dissolves [58]. In this section, the chemical equations and the rate of dissolution of calcite is discussed.

According to [38], studies were conducted by [42] on the "dissolution of calcite in $CO_2 - H_2O$ solution, using pH -stat and free drift methods, over pH ranges from about $2 - 7$, P_{CO_2} from 0.0003 to 0.97 atm, and temperature from 5^o to 60^oC." Results from the study indicate that, three reactions occur simultaneously on the surface of the calcite. These reactions include:

$$CaCO_3 + H^+ \rightleftharpoons Ca^{2+} + HCO_3^-, \tag{2.7.1}$$

$$CaCO_3 + H_2CO_3 \rightleftharpoons Ca^{2+} + 2HCO_3^-, \tag{2.7.2}$$

$$CaCO_3 + H_2O \rightleftharpoons Ca^{2+} + HCO_3^+ + OH^-. \tag{2.7.3}$$

The proposed dissolution mechanism given by Equations 2.7.1 to 2.7.3 implies that the dissolution of calcite is not caused by hydrogen ions only, but also caused by the water (H_2O) and carbonic acid H_2CO_3 which is produced during the dissolution process. However, among the dissolution reactions, calcite dissolution by H^+ is greater than H_2CO_3 and H_2O [38].

According to [38], the rate law that was proposed for the dissolution of calcite in the experiment is given by:

$$\begin{aligned} R_{CaCO_3} = {} & K_{H^+}[H^+]^* + K_{H_2CO_3}[H_2CO_3]^* + K_{H_2O}[H_2O]^* \\ & - K_{Ca^{2+}}[Ca^{2+}]^*[H_2CO_3^-]^*, \end{aligned} \tag{2.7.4}$$

where $K_{H^+}, K_{H_2CO_3}, K_{H_2O}$ are the forward reaction rate constants in chemical Equations 2.7.1, 2.7.2, 2.7.3, respectively. $K_{Ca^{2+}}$ is the backward reaction rate constant which depends on temperature and partial pressure of carbon dioxide (P_{CO_2}). $[i]^*$ indicates

activity of the chemical species i. The value of $K_{Ca^{2+}}$ is given by [38]:

$$K_{Ca^{2+}} = \frac{K*_{H_2CO_3}}{K_{sp}}\left[K*_{H^+} + \frac{1}{[H^+]^*}\left(K_{H_2CO_3}[H_2CO_3]^* + K_{H_2O}[H_2O]^*\right)\right], \tag{2.7.5}$$

where $K*_{H_2CO_3}$ is the second dissociation constant for carbonic acid, $K*_{H^+}$ is a first-order mechanistic rate constant for H^+ attacks, and K_{sp} is the calcite equilibrium constant for the chemical reaction:

$$CaCO_3 \rightleftharpoons Ca^{2+} + CO_3^{2-}. \tag{2.7.6}$$

The rate law given by Equation 2.7.4 determines the net rate of dissolution of calcite under the given experimental conditions. Table 2.2 contains numerical values of the reaction constants that are involved in the dissolution process.

K_{H^+}	$K_{H_2CO_3}$	K_{H_2O}	$\log K_{sp}$	$\log K*_{H_2CO_3}$
0.051	$3.45 \times \exp(-5)$	$1.19 \times \exp(-7)$	-8.475	-6.351

Table 2.2: Rate constants for calcite dissolution in units of cm/s given by [38].

However, from the Table 2.2, the numerical values for the reaction constants $K_{H_2CO_3}$ and $K_{H_2CO_3}$, are small. Thus the effects of terms $K_{H_2CO_3}[H_2CO_3]$ and $K_{H_2O}[H_2O]$ are small. The sum $K_{H_2CO_3}[H_2CO_3]^* + K_{H_2O}[H_2O]^*$ in the rate law given by Equation 2.7.4 will be negligible when the activities $[H_2CO_3]^*$ and $K_{H_2O}[H_2O]^*$, are small. In our discussion, we neglect the sum $K_{H_2CO_3}[H_2CO_3]^* + K_{H_2O}[H_2O]^*$ and obtain a simplified rate law given by:

$$R_{CaCO_3} = K_{H^+}[H^+]^* - K_{Ca^{2+}}[Ca^{2+}]^*[HCO_3^-]^*. \tag{2.7.7}$$

The implication of neglecting the contribution $K_{H_2CO_3}[H_2CO_3]^* + K_{H_2O}[H_2O]^*$ is that, calcite dissolution by carbonic acid and water which are described by chemical Equations 2.7.2 and 2.7.3 are not significant. Thus the only chemical equation that describes the dissolution of calcite in our discussion is Equation 2.7.1.

By chemical Equation 2.7.1, dissolution of calcite by the acid is a reversible reaction. The forward reaction is called dissolution and the backward reaction is called precipitation [36]. Dissolution is dominant when there is low concentration of Ca^{2+} and HCO_3^-, and

high concentrations of $CaCO_3$ and H^+ ions [36]. Precipitation is dominant when there is high concentrations of Ca^{2+} and HCO_3^- ions and low concentrations of $CaCO_3$ and H^+ ion [36]. When the concentrations of reactants are equal to the concentrations of product equilibrium is established and neither dissolution or precipitation occurs. Thus the rate law given by Equation 2.7.7 becomes:

$$\begin{aligned} K_{H^+}[H^+]^* - K_{Ca^{2+}}[Ca^{2+}]^*[HCO_3^-]^* &= 0, \\ \Longrightarrow \frac{[Ca^{2+}]^*[HCO_3^-]^*}{[H^+]^*} &= \frac{K_{H^+}}{K_{Ca^{2+}}}, \end{aligned} \tag{2.7.8}$$

where $\frac{K_{H^+}}{K_{Ca^{2+}}} = K_C$ is the equilibrium constant of the chemical reaction Equation 2.7.1. For consistency, we express the left hand side of Equation 2.7.8 in concentration instead of ion activity. This is achieved by multiplying Equation 2.7.8 by activity coefficients [16, 59, 58]. Thus we obtain:

$$\frac{\eta_{Ca^{2+}}[Ca^{2+}]\eta_{HCO_3^-}[HCO_3^-]}{\eta_{H^+}[H^+]} = \frac{K_{H^+}}{K_{Ca^{2+}}}, \tag{2.7.9}$$

where $\eta_{HCO_3^-}, \eta_{Ca^{2+}}$ and η_{H^+} are the activity coefficients for HCO_3^-, Ca^{2+} and H^+, respectively. Let $\eta_{eq} = \frac{\eta_{H^+}}{\eta_{Ca^{2+}}\eta_{HCO_3^-}}$, then Equation 2.7.9 becomes:

$$\frac{[Ca^{2+}][HCO_3^-]}{[H^+]} = K_{eq} \tag{2.7.10}$$

where $K_{eq} = \eta_{eq}K_C$, which has a dimension of $[L^3M^{-1}T^{-1}]$.

2.7.1 Analytical solution to calcite dissolution rate law

The features of the reversible reaction 2.7.1 can be illustrated graphically by solving the calcite dissolution rate law given by Equation 2.7.7. In this section, we derive an analytical solution of the rate law. Let $[H^+]_0, [Ca^{2+}]_0$ and $[HCO_3^-]_0$ be the initial concentrations of the species H^+, Ca^{2+} and HCO_3^-, respectively. If the concentrations in the acidic solution at a later time are $[H^+], [Ca^{2+}]$ and $[HCO_3^-]$, then the change in species concentration denoted by χ, is given by:

$$\chi = [H^+]_0 - [H^+] = [Ca^{2+}] - [Ca^{2+}]_0 = [HCO_3^-] - [HCO_3^-]_0. \tag{2.7.11}$$

By rearranging Equation 2.7.11, the species concentrations at any time is given by:

$$[H^+] = [H^+]_0 - \chi, \tag{2.7.12}$$

$$[Ca^{2+}] = [Ca^{2+}]_0 + \chi, \tag{2.7.13}$$

and

$$[HCO_3^-] = [HCO_3^-]_0 + \chi. \tag{2.7.14}$$

The summary of the dissolution reaction progress and the changes in species concentration with time, is given by Table 2.3.

	$CaCO_3$	+	H^+	$\rightleftharpoons$	Ca^{2+}	+	HCO_3^-
Initial conc.:	0		$[H^+]_0$		$[Ca^{2+}]_0$		$[HCO_3^-]_0$
Later conc.:	χ		$-\chi$		$+\chi$		$+\chi$
Resultant:			$[H^+]_0 - \chi$		$[Ca^{2+}]_0 + \chi$		$[HCO_3^-]_0 + \chi$

Table 2.3: Calcite dissolution and species concentrations at any time.

To proceed with the derivation, we substitute Equations 2.7.12, 2.7.13 and 2.7.14 into Equation 2.7.7, and express the ion activities as functions of concentration. Thus we obtain:

$$\begin{aligned} R_{CaCO_3} &= K_{H^+}\eta_{H^+}\Big([H^+]_0 - \chi\Big) \\ &\quad - K_{Ca^{2+}}\eta_{HCO_3^-}\eta_{Ca^{2+}}(([Ca^{2+}]_0 + \chi)([HCO_3^-]_0 + \chi)). \end{aligned} \tag{2.7.15}$$

Let $K_f = K_{H^+}\eta_{H^+}$ and $K_b = K_{Ca^{2+}}\eta_{HCO_3^-}\eta_{Ca^{2+}}$. Expanding and rearranging Equation 2.7.15, we have:

$$\begin{aligned} \frac{d\chi}{dt} &= K_f[H^+]_0 - K_b[Ca^{2+}]_0[HCO_3^-]_0 \\ &\quad + (-K_f - K_b[Ca^{2+}]_0 - K_b[HCO_3^-]_0)\chi - K_b\chi^2. \end{aligned} \tag{2.7.16}$$

Let

$$\alpha_1 = K_f[H^+]_0 - K_b[Ca^{2+}]_0[HCO_3^-]_0,$$

and

$$\alpha_2 = -(K_f + K_b[Ca^{2+}]_0 + K_b[HCO_3^-]_0).$$

Then Equation 2.7.16 becomes:

$$\frac{d\chi}{dt} = \alpha_1 + \alpha_2\chi - K_b\chi^2. \tag{2.7.17}$$

Rearranging Equation 2.7.17, we have:

$$\frac{d\chi}{\alpha_1 + \alpha_2\chi - K_b\chi^2} = dt. \tag{2.7.18}$$

The roots of $\alpha_1 + \alpha_2\chi - K_b\chi^2$ are given by:

$$\Theta_1 = \chi = \frac{-\alpha_2 - \sqrt{\alpha_2^2 + 4K_b\alpha_1}}{-2K_b}, \tag{2.7.19}$$

and

$$\Theta_2 = \chi = \frac{-\alpha_2 + \sqrt{\alpha_2^2 + 4K_b\alpha_1}}{-2K_b}. \tag{2.7.20}$$

Thus by substituting Equations 2.7.19 and 2.7.20 into Equation 2.7.18, we obtain:

$$\begin{aligned}(\chi - \Theta_1)(\chi - \Theta_2) &= \left(\chi - \frac{-\alpha_2 - \sqrt{\alpha_2^2 + 4K_b\alpha_1}}{-2K_b}\right)\left(\chi - \frac{-\alpha_2 + \sqrt{\alpha_2^2 + 4K_b\alpha_1}}{-2K_b}\right) \\ &= \chi^2 - \frac{\alpha_2 - \sqrt{\alpha_2^2 + 4K_b\alpha_1}}{2K_b}\chi - \frac{\alpha_2 + \sqrt{\alpha_2^2 + 4K_b\alpha_1}}{2K_b}\chi \\ &+ \frac{\alpha_2^2 - \alpha_2^2 - 4K_b\alpha_1}{4K_b^2} \\ &= \chi^2 - \frac{\alpha_2}{K_b}\chi - \frac{\alpha_1}{K_b}\end{aligned} \tag{2.7.21}$$

Therefore, by Equation 2.7.21: $\alpha_1 + \alpha_2\chi - K_b\chi^2 = -K_b(\chi - \Theta_1)(\chi - \Theta_2)$. Substituting into Equation 2.7.18, we obtain:

$$\frac{d\chi}{(\chi - \Theta_1)(\chi - \Theta_2)} = -K_b\ dt. \tag{2.7.22}$$

Since Equation 2.7.22 is an ordinary differential equation, it can be integrated to obtain a solution. However, we first need to express the integrand in partial fractions, thus we write:

$$\frac{1}{(\chi-\Theta_1)(\chi-\Theta_2)} = \frac{P}{(\chi-\Theta_1)} + \frac{Q}{(\chi-\Theta_2)}, \tag{2.7.23}$$

where P and Q are arbitrary constants. Comparing both sides of Equation 2.7.23, we have:

$$P(\chi-\Theta_2) + Q(\chi-\Theta_1) = 1,$$

when $\chi = \Theta_2$, we have:

$$Q = \frac{1}{(\Theta_2-\Theta_1)}.$$

And when $\chi = \Theta_1$, we have:

$$P = \frac{1}{(\Theta_1-\Theta_2)}.$$

Now substituting P and Q into Equation 2.7.22, we obtain:

$$\frac{d\chi}{(\chi-\Theta_1)(\Theta_1-\Theta_2)} - \frac{d\chi}{(\chi-\Theta_2)(\Theta_1-\Theta_2)} = -K_b\ dt. \tag{2.7.24}$$

Integrating both sides of Equation 2.7.24, we have:

$$\begin{aligned}
&\Big(\frac{1}{(\chi-\Theta_1)(\Theta_1-\Theta_2)} - \frac{1}{(\chi-\Theta_2)(\Theta_1-\Theta_2)}\Big)d\chi = -K_b\ dt. \\
\Longrightarrow &\frac{1}{(\Theta_1-\Theta_2)}\Big(\int \frac{d\chi}{(\chi-\Theta_1)} - \int \frac{d\chi}{(\chi-\Theta_2)}\Big) = \int -K_b\ dt. \\
\Longrightarrow &ln|\chi-\Theta_1| - \ln|\chi-\Theta_2| = -Kb(\Theta_1-\Theta_2)t + R
\end{aligned} \tag{2.7.25}$$

where R is an integration constant. Initially when $t = 0$, there is no change in concentration since no reaction has occurred, thus $\chi(0) = 0$. Substituting $\chi(0) = 0$ into Equation 2.7.25, we obtain $R = ln(\frac{\Theta_1}{\Theta_2})$. By substituting $R = ln(\frac{\Theta_1}{\Theta_2})$ into Equation 2.7.25, we obtain a more specific solution as:

$$\begin{aligned}
&\ln(\chi-\Theta_1) - ln(\chi-\Theta_2) = -K_b(\Theta_1-\Theta_2)t + ln(\frac{\Theta_1}{\Theta_2}), \\
\Longrightarrow &\ln(\frac{(\chi-\Theta_1)}{(\chi-\Theta_2)}) = -K_b(\Theta_1-\Theta_2)t + ln(\frac{\Theta_1}{\Theta_2}), \\
\Longrightarrow &\frac{(\chi-\Theta_1)}{(\chi-\Theta_2)} = \frac{\Theta_1}{\Theta_2}\exp^{-K_b(\Theta_1-\Theta_2)t}.
\end{aligned} \tag{2.7.26}$$

Multiplying both sides of Equation 2.7.26 by $(\chi - \Theta_2)$, we have:

$$(\chi - \Theta_1) = (\chi - \Theta_2)\frac{\Theta_1}{\Theta_2}\exp^{-K_b(\Theta_1-\Theta_2)t}. \tag{2.7.27}$$

Expanding and rearranging Equation 2.7.27, we obtain:

$$\chi\left(1 - \frac{\Theta_1}{\Theta_2}\exp^{-K_b(\Theta_1-\Theta_2)t}\right) = \Theta_1 - \Theta_1\exp^{-K_b(\Theta_1-\Theta_2)t}. \tag{2.7.28}$$

Dividing both sides of Equation 2.7.28 by $\left(1 - \frac{\Theta_1}{\Theta_2}\exp^{-K_b(\Theta_1-\Theta_2)t}\right)$ and simplifying, we obtain:

$$\chi = \frac{\Theta_1\Theta_2\left(1 - \exp^{-K_b(\Theta_1-\Theta_2)t}\right)}{\Theta_2 - \Theta_1\exp^{-K_b(\Theta_1-\Theta_2)t}}. \tag{2.7.29}$$

Therefore the concentration of the chemical species at any time is given by:

$$[H^+] = [H^+]_0 - \frac{\Theta_1\Theta_2\left(1 - \exp^{-K_b(\Theta_1-\Theta_2)t}\right)}{\Theta_2 - \Theta_1\exp^{-K_b(\Theta_1-\Theta_2)t}}, \tag{2.7.30}$$

$$[Ca^{2+}] = [Ca^{2+}]_0 + \frac{\Theta_1\Theta_2\left(1 - \exp^{-K_b(\Theta_1-\Theta_2)t}\right)}{\Theta_2 - \Theta_1\exp^{-K_b(\Theta_1-\Theta_2)t}}, \tag{2.7.31}$$

$$[HCO_3^-] = [HCO_3^-]_0 + \frac{\Theta_1\Theta_2\left(1 - \exp^{-K_b(\Theta_1-\Theta_2)t}\right)}{\Theta_2 - \Theta_1\exp^{-K_b(\Theta_1-\Theta_2)t}}. \tag{2.7.32}$$

The graphs in Figure 2.2 are generated from the analytical solution using data from [58].

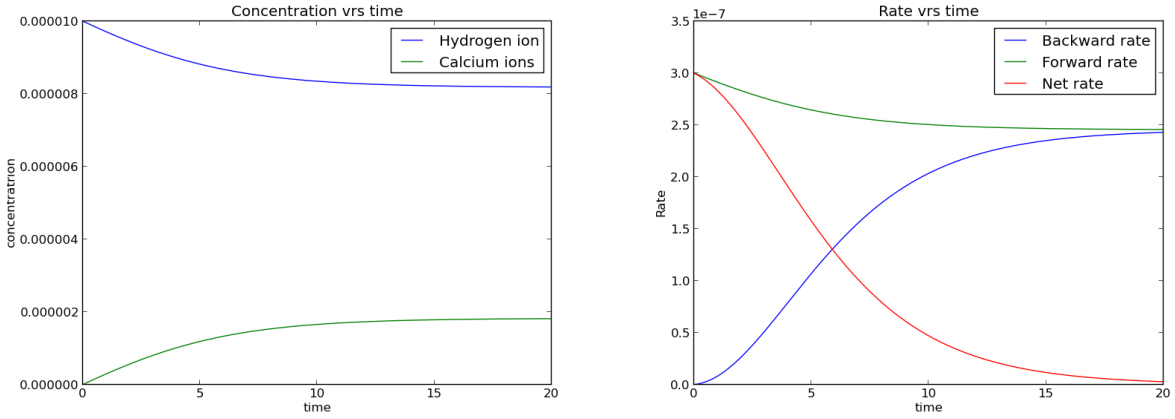

Figure 2.2: Species concentration profiles and dissolution-rate profiles for reaction 2.7.1.

The graph at the left hand side of Figure 2.2 shows the species concentration profile with time. The data used for generating the graphs contain a high concentration of hydrogen ions. It can be observed that while the concentration of H^+ (a reactant) decreases with time, the concentration of Ca^{2+} (which is a product) increases with time until equilibrium is achieved. The graph at the right hand side of Figure 2.2 shows the dissolution-rate profile in time. It can be observed that, while the rate of forward reaction is highest at the beginning of the reaction, the rate of backward reaction is lowest at the beginning of the reaction. It can also be observed that while the rate of forward reaction decreases until equilibrium is achieved the rate of backward reaction increases with time until equilibrium is achieved. It can also be observed that the net rate of reaction is highest at the beginning but decreases to zero when equilibrium is achieved.

2.7.2 Equilibrium concentrations of chemical species

At the beginning of the chemical reaction 2.7.1, no products are formed and very small amounts are available in the aqueous solution (mine effluent water), thus as defined previously, let the initial concentration of HCO_3^-, Ca^{2+} be given by $[HCO_3^-]_0, [Ca^{2+}]_0$ and the concentration of H^+ which is a reactant be given by $[H^+]_0$. At equilibrium, the concentration of the H^+ ions is the sum of the initial concentrations and the change that occurred later as the reaction proceeded. Since the stoichiometric coefficients of HCO_3^-, Ca^{2+} and H^+ ions are equal to one, the equilibrium concentration of the chemical species is given by:

$$[H^+]_{eq} = [H^+]_0 - \chi, \tag{2.7.33}$$

$$[HCO_3^-]_{eq} = [HCO_3^-]_0 + \chi, \tag{2.7.34}$$

$$[Ca^{2+}]_{eq} = [Ca^{2+}]_0 + \chi. \tag{2.7.35}$$

Thus substituting Equations 2.7.33, 2.7.34 and 2.7.35 into Equation 2.7.10, we obtain:

$$\begin{aligned}
&\frac{([Ca^{2+}]_0+\chi)([HCO_3^-]_0+\chi)}{[H^+]_0-\chi}=K_{eq},\\
\Longrightarrow&\chi^2+\Big([Ca^{2+}]_0+[HCO_3^-]_0+K_{eq}\Big)\chi-[H^+]_0K_{eq}=0,\\
\Longrightarrow&\chi=\frac{-\Big([Ca^{2+}]_0+[HCO_3^-]_0+K_{eq}\Big)\pm\sqrt{\Big([Ca^{2+}]_0+[HCO_3^-]_0+K_{eq}\Big)^2+4[H^+]_0K_{eq}}}{2}.
\end{aligned} \tag{2.7.36}$$

The value of $\Big([Ca^{2+}]_0+[HCO_3^-]_0+K_{eq}\Big)$ is always positive, and since the concentration of H^+ must be positive so that the solution can be physically realistic, the discriminant is always positive, i. e.

$$\sqrt{\Big([Ca^{2+}]_0+[HCO_3^-]_0+K_{eq}\Big)^2+4[H^+]_0K_{eq}}\geq 0.$$

Thus the solution that will avoid negative concentration values is:

$$\chi=\frac{-\Big([Ca^{2+}]_0+[HCO_3^-]_0+K_{eq}\Big)+\sqrt{\Big([Ca^{2+}]_0+[HCO_3^-]_0+K_{eq}\Big)^2+4[H^+]_0K_{eq}}}{2} \tag{2.7.37}$$

Therefore, combining Equations 2.7.37 and 2.7.35, the equilibrium concentration of Ca^{2+} is given by:

$$[HCO_3^-]_{eq}=[Ca^{2+}]_0+\frac{-\Big([Ca^{2+}]_0+[HCO_3^-]_0+K_{eq}\Big)+\sqrt{\Big([Ca^{2+}]_0+[HCO_3^-]_0+K_{eq}\Big)^2+4[H^+]_0K_{eq}}}{2}. \tag{2.7.38}$$

By combining Equations 2.7.37 and 2.7.34, the equilibrium concentration of HCO_3^- is given by:

$$[HCO_3^-]_{eq}=[HCO_3^-]_0+\frac{-\Big([Ca^{2+}]_0+[HCO_3^-]_0+K_{eq}\Big)+\sqrt{\Big([Ca^{2+}]_0+[HCO_3^-]_0+K_{eq}\Big)^2+4[H^+]_0K_{eq}}}{2}, \tag{2.7.39}$$

By combing Equations 2.7.37 and 2.7.33, the equilibrium concentration of H^+ is given by:

$$[H^+]_{eq} = [H^+]_0 - \frac{-\left([Ca^{2+}]_0 + [HCO_3^-]_0 + K_{eq}\right) + \sqrt{\left([Ca^{2+}]_0 + [HCO_3^-]_0 + K_{eq}\right)^2 + 4[H^+]_0 K_{eq}}}{2}. \tag{2.7.40}$$

2.7.3 Modifications to the dissolution-precipitation rate law

The rate law given by Equations 2.7.7 is a function of three arguments and each argument is a function of other variables. The expressions for the rate law arguments are given by Equation 2.7.30. At each time point, all the arguments must be evaluated first before the rate can be computered. If the arguments are involved in other reactions, then the system becomes a large complicated network. However, the network system can be decoupled by using stoichiometric transformation. In this section, we modify the rate law 2.7.7 to obtain a decoupled set of equations describing the same rate law.

If the equilibrium concentration of HCO_3^- or Ca^{2+} is known, the rate law given by Equation 2.7.7 can be reduced to a two-variable-dependent expression. According to [23], the rate of precipitation (backward reaction rate) can be approximated by:

$$K_{Ca^{2+}}[Ca^{2+}]^*[HCO_3^-]^* \approx 2K_{Ca^{2+}}\left([Ca^{2+}]^*\right)^2, \tag{2.7.41}$$

and

$$K_{Ca^{2+}}[Ca^{2+}]^*[HCO_3^-]^* \approx 2K_{Ca^{2+}}\left([HCO_3^-]^*\right)^2. \tag{2.7.42}$$

The approximations 2.7.41 and 2.7.42 are verified in experiments involving pure water and calcite interactions. By substituting Equation 2.7.41 into Equation 2.7.7, the calcite dissolution rate law becomes:

$$R_{CaCO_3} = K_{H^+}[H^+]^* - 2K_{Ca^{2+}}\left([Ca^{2+}]^*\right)^2. \tag{2.7.43}$$

Substituting Equation 2.7.42 into Equation 2.7.7, the calcite dissolution and precipitation rate law is also given by:

$$R_{CaCO_3} = K_{H^+}[H^+]^* - 2K_{Ca^{2+}}\left([HCO_3^-]^*\right)^2. \tag{2.7.44}$$

At equilibrium $R_{CaCO_3} = 0$ and the activities/concentrations of HCO_3^- and Ca^{2+} ions are the respective equilibrium activities/concentrations. Thus applying this boundary condition to Equations 2.7.43 and 2.7.44 and rearranging the results, we obtain [23]:

$$2K_{Ca^{2+}} = \frac{K_{H^+}[H^+]^*}{\left([Ca^{2+}]_{eq}\right)^2}, \tag{2.7.45}$$

and

$$2K_{Ca^{2+}} = \frac{K_{H^+}[H^+]^*}{\left([HCO_3^-]_{eq}\right)^2}. \tag{2.7.46}$$

Substituting Equation 2.7.45 into Equation 2.7.43, we obtain [23]:

$$R_{CaCO_3} = K_{H^+}[H^+]^*\left(1 - \frac{\left([Ca^{2+}]^*\right)^2}{\left([Ca^{2+}]_{eq}\right)^2}\right), \tag{2.7.47}$$

and by substituting Equation 2.7.46 into Equation 2.7.44, we obtain:

$$R_{CaCO_3} = K_{H^+}[H^+]^*\left(1 - \frac{\left([HCO_3^-]^*\right)^2}{\left([HCO_3^-]_{eq}\right)^2}\right). \tag{2.7.48}$$

The modified rate laws given by Equations 2.7.47 and 2.7.48 are compared with the original rate law 2.7.7 in Figure 2.3.

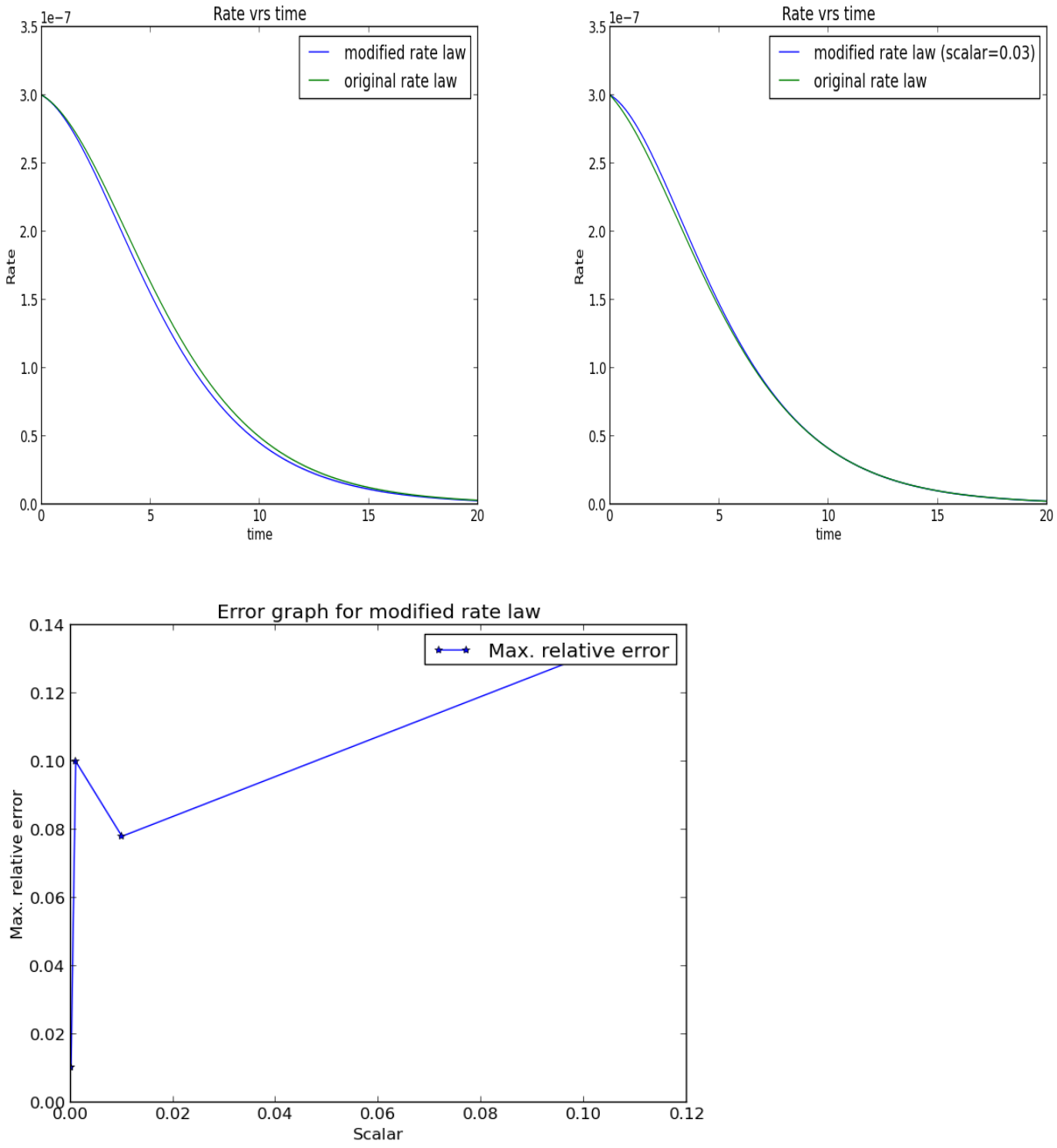

Figure 2.3: Comparing the modified rate law with the original rate law 2.7.7.

The modified rate law under estimates the original rate law with a maximum relative error of 13%. However, the error depends on the ratio between initial activities/concentrations of H^+ and products (Ca^{2+}, HCO_3^-). For any initial activities/concentrations

$[HCO_3^-]_0$, $[H^+]_0$, and $[Ca^{2+}]_0$ a scalar ratio α_{sca}, can be defined such that:

$$[H^+]_0 + [Ca^{2+}]_0 = \alpha_{sca}[H^+]_0. \tag{2.7.49}$$

Equation 2.7.49 can be rearranged to obtain:

$$\alpha_{sca} = \frac{[H^+]_0 + [Ca^{2+}]_0}{[H^+]_0}. \tag{2.7.50}$$

To investigate the relationship between the scalar (α_{sca}) and the accuracy of the modified rate law, the scalar α_{sca} and maximum relative error was calculated from different input data values for $[HCO_3^-]_0, [H^+]_0$, and $[Ca^{2+}]_0$. Table 2.4, contains the measured values for α_{sca} and the maximum relative error. The third graph in Figure 2.3 illustrates the relationship between the scalar α_{sca} and the maximum relative error. By comparing the graph at the left hand side with the graph at the right hand side of Figure 2.3, one can notice the effect of the scalar α_{sca}.

Scalar (α_{sca})	**Maximum relative error**
0.10000	0.1308
0.01000	0.0780
0.00100	0.1000
0.00010	0.1019
0.00001	0.01021

Table 2.4: Relationship between error and the ratio of reaction products and reactants.

However, the problem under consideration concerns nature and we can not control the input data. Thus the modified rate laws given by Equations 2.7.47 and 2.7.48 are not suitable for our discussion.

Furthermore, we express Equation 2.7.7 in concentrations instead of activities, thus we obtain:

$$R_{CaCO_3} = K_f[H^+] - K_b[HCO^-][Ca^{2+}]. \tag{2.7.51}$$

By rearranging Equation 2.7.12, the change in concentration χ, is given by:

$$\chi = [H^+]_0 - [H^+]. \tag{2.7.52}$$

Substituting Equation 2.7.52 into Equations 2.7.13 and 2.7.14, we obtain:

$$[Ca^{2+}] = [Ca^{2+}]_0 + [H^+]_0 - [H^+], \tag{2.7.53}$$

and

$$[HCO_3^-] = [HCO_3^-]_0 + [H^+]_0 - [H^+]. \tag{2.7.54}$$

By substituting Equations 2.7.53 and 2.7.54 into Equation 2.7.51, we obtain:

$$\begin{aligned} R_{CaCO_3} &= K_f[H^+] \\ &\quad - K_b\Big([HCO_3^-]_0 + [H^+]_0 - [H^+]\Big)\Big([Ca^{2+}]_0 + [H^+]_0 - [H^+]\Big). \end{aligned} \tag{2.7.55}$$

Expanding and simplifying Equation (2.7.55), we obtain:

$$R_{CaCO_3} = K_b[H^+]^2 + \alpha_3[H^+] - \alpha_4, \tag{2.7.56}$$

where:

$$\alpha_3 = K_f + K_b\Big([H^+]_0 + [HCO_3^-]_0\Big) + K_b\Big([H^+]_0 + [Ca^{2+}]_0\Big), \tag{2.7.57}$$

and

$$\alpha_4 = K_b\Big([H^+]_0 + [HCO_3^-]_0\Big)\Big([H^+]_0 + [Ca^{2+}]_0\Big). \tag{2.7.58}$$

Equation 2.7.56 is a modified rate law for the calcite dissolution reaction. This rate law 2.7.56 is a function of H^+ ion concentration only.

Similarly, we will obtain a modified rate law that is a function of Ca^{2+} ion concentration only. We express the change in concentration χ, in terms of Ca^{2+} ion concentration, thus:

$$\chi = [Ca^{2+}] - [Ca^{2+}]_0. \tag{2.7.59}$$

Substituting Equation 2.7.59 into Equations 2.7.12 and 2.7.14, we obtain:

$$[H^+] = [H^+]_0 - [Ca^{2+}] + [Ca^{2+}]_0 \tag{2.7.60}$$

and

$$[HCO_3^-] = [HCO_3^-]_0 + [Ca^{2+}] - [Ca^{2+}]_0. \tag{2.7.61}$$

By substituting Equations 2.7.60 and 2.7.61 into Equation 2.7.51, and after expansion and simplification, we obtain:

$$R_{CaCO_3} = \alpha_5 - \alpha_6[Ca^{2+}] - K_b[Ca^{2+}]^2, \tag{2.7.62}$$

where:

$$\alpha_5 = K_f\Big([H^+]_0 + [Ca^{2+}]_0\Big), \tag{2.7.63}$$

and

$$\alpha_6 = \Big(K_f + K_b[H^+]_0 - K_b[Ca^{2+}]_0\Big). \tag{2.7.64}$$

Equation 2.7.62 is also a modified rate law for the calcite dissolution reaction. This rate law 2.7.56 is a function of Ca^{2+} ion concentration only. Since the mole ratio of Ca^{2+} and HCO_3^- ions is one to one, in Equation 2.7.62 we replace $[Ca^{2+}]$ by $[HCO_3^-]$ and $[Ca^{2+}]_0$ by $[HCO_3^-]_0$. Thus modification to the calcite dissolution rate law 2.7.51 with respect to HCO_3^- ion concentration is given by:

$$R_{CaCO_3} = \alpha_7 - \alpha_8[HCO_3^-] - K_b[HCO_3^-]^2, \tag{2.7.65}$$

where:

$$\alpha_7 = K_f\Big([H^+]_0 + [HCO_3^-]_0\Big), \tag{2.7.66}$$

and

$$\alpha_8 = \Big(K_f + K_b[H^+]_0 - K_b[HCO_3^-]_0\Big). \tag{2.7.67}$$

In Figure 2.4, we compare the modified rate laws given by Equations 2.7.56, 2.7.62 and 2.7.65 to the original rate law 2.7.51.

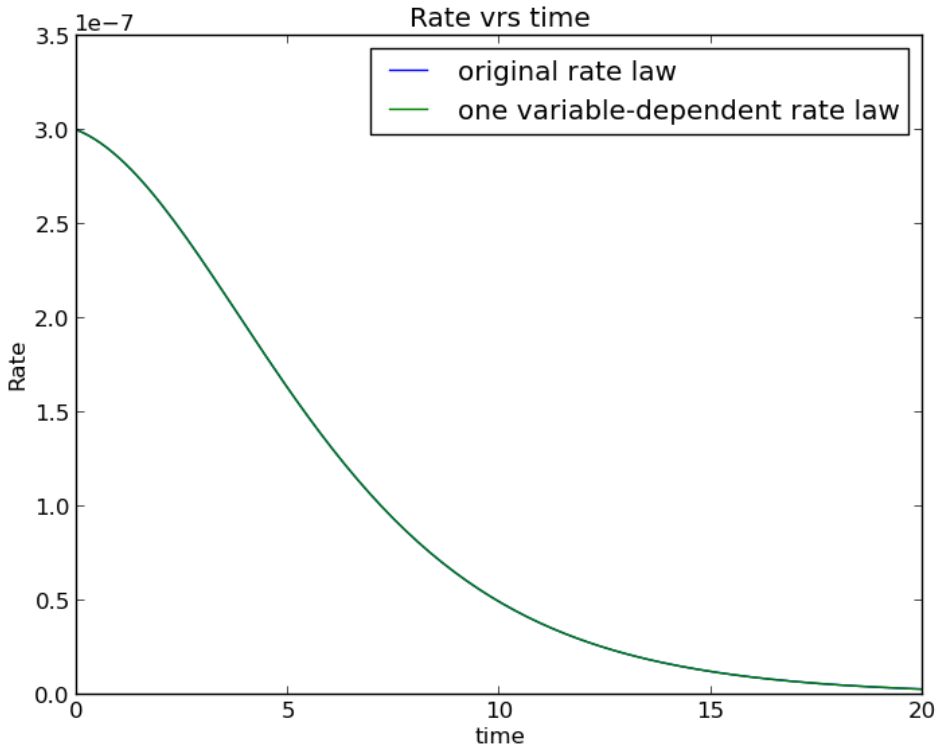

Figure 2.4: Comparing modified rate laws 2.7.56, 2.7.62 and 2.7.65 and the original rate law given by Equation 2.7.51.

From Figure 2.4, we observe that the modified rate laws given by Equations 2.7.56, 2.7.62 and 2.7.65 are exactly the same as the original rate law 2.7.51. Any one of the modified Equations 2.7.56, 2.7.62 and 2.7.65 depends on one variable only, thus can be used for decoupling a system of equations. The accuracy does not depend on initial inputs as with the earlier modification.

The dissolution-precipitation reaction that has been discussed takes place in an aqueous solution. However, the dissolution-precipitation reaction in the open limestone channel treatment method takes place at an interface. Interface reactions depend on concentrations of solutes and the surface area of the dissolving solid [36]. The surface area measures the probability that the dissolving solid (calcite) is available for reaction. We will modify the rate law for calcite dissolution-precipitation reaction derived for the aqueous case (given by Equation 2.7.51), to obtain a calcite dissolution-precipitation rate law for the

interface reaction case. If there is no surface area dissolution does not occur but precipitation can still occur, thus the surface area only affects the rate of forward reaction. We propose a first-order dependence of the rate of dissolution on the specific surface area of the limestone. However, since filtration of $Fe(OH)_3$ will prevent dissolution, the surface area available for hydrogen ion attachment and reaction is given by $(1-\theta_c)\mathcal{B}(\theta_f)\theta_L$. Therefore, the modified calcite dissolution rate law for the interface reaction is given by:

$$R_{CaCO_3} = K_f\big((1-\theta_c)\mathcal{B}(\theta_f)\big)\theta_L[H^+] - K_b[Ca^{2+}][HCO_3^-]. \tag{2.7.68}$$

The molar concentration rate law is converted to the mass concentration rate law:

$$R_{CaCO_3} = 100(1-\theta_c)\mathcal{B}(\theta_f)\theta_L C_1 - 0.04098361 K_b C_6 C_8. \tag{2.7.69}$$

2.8 Rate of hydrogen ion consumption

From the dissolution reaction given by Equation 2.3.1, the mole ratio of hydrogen and calcite is one to one, thus the rate of consumption of the hydrogen ions is equal to the rate of dissolution of calcite. Thus we obtain:

$$S_1 = -K_f\big((1-\theta_c)\mathcal{B}(\theta_f)\big)\theta_L[H^+] + K_b[Ca^{2+}][HCO_3^-]. \tag{2.8.1}$$

Converting the molar concentrations to mass concentrations, we obtain:

$$S_1 = -K_f\big((1-\theta_c)\mathcal{B}(\theta_f)\big)\theta_L C_1 + 0.00040984 K_b C_6 C_8. \tag{2.8.2}$$

2.9 Rate of calcium ion formation

From the dissolution reaction given by Equation 2.3.1, the mole ratio of calcium and calcite is one to one, implying that the rate of formation of the calcium ions is equal to the rate of dissolution of calcite. Thus we obtain:

$$S_6 = K_f\big((1-\theta_c)\mathcal{B}(\theta_f)\big)\theta_L[H^+] - K_b[Ca^{2+}][HCO_3^-]. \tag{2.9.1}$$

We convert the molar concentration rate law 2.9.1 to the mass concentration rate law:

$$S_6 = 40K_f\big((1-\theta_c)\mathcal{B}(\theta_f)\big)\theta_L C_1 - 0.0164K_b C_6 C_8. \tag{2.9.2}$$

2.10 Rate of HCO_3^- formation

From the dissolution reaction given by Equation 2.3.1, the mole ratio of HCO_3^- and calcite is one to one, thus the rate of formation of the HCO_3^- is equal to the rate of consumption of hydrogen ions. Thus we obtain:

$$S_8 = K_f\big((1-\theta_c)\mathcal{B}(\theta_f)\big)\theta_L[H^+] - K_b[Ca^{2+}][HCO_3^-]. \tag{2.10.1}$$

We convert the molar concentration rate law 2.10.1 to the mass concentration rate law:

$$S_8 = 61K_f\big((1-\theta_c)\mathcal{B}(\theta_f)\big)\theta_L C_1 - 0.025K_b C_6 C_8. \tag{2.10.2}$$

2.11 Summary

In this Chapter, the composition of mine effluent water is obtained by reviewing literature on pyritic systems. Kinetic data for the physico-chemical processes in the OLC treatment is obtained. A decoupling technique is developed based on stoichiometry. The rate at which species are produced or consummed is obtained from the kinetic data.

Chapter 3

Mathematical Modelling of AMD in Limestone

Material bodies that have multiphase structures with one of the phases being solid are called porous media [69, 70, 7]. The solid phase is distributed throughout the entire structure, and the other phases (which include one or more fluid phases, e.g. water and oil) occupy spaces called void or pore space within the structure. Porous media exist naturally or artificially. Examples are bread, lungs, kidneys, sand, soil and foam [7, 69, 70].

The porous medium considered in this work is a porous rock called limestone. Some porous rocks are composed of particles that are cemented together (e.g. sandstone), such rocks are said to be consolidated [12]. Other types of porous rocks have pore-spaces that were created by evolution of gases during crystallization or by leaching. Examples of such rocks include limestone and dolomites [12]. The pore-spaces in such porous rocks are channels called vugs [12, 11]. According to [11], the vugs occupy tiny volumes in the rocks and are usually narrow and interconnected, thus porosity of vugular limestone is typically low but their permeabilities are high.

Furthermore, not all limestones are vugular. Some were formed by cementation of limestone particles [12]. Such limestones can also be called consolidated. The limestone in our study is unconsolidated.

There are two broad steps for describing transport phenomena in porous media. These steps are microscopic and macroscopic approaches [69]. The microscopic approach is a statistical approach that accounts for the mean behaviour of a molecular system. The macroscopic approach is also a statistical approach used to circumvent complicated geometrical problems and large length scale problems.

In this Chapter 3, we give detailed derivations of both microscopic and macroscopic models.

3.1 Microscopic model

In this section, a generalized microscopic transport equation is derived by conserving fluid mass through a control volume. Mass, momentum and energy transport equations are deduced from the general conservation equation. Figure 3.1 shows a simple three-dimensional control volume in rectangular coordinates.

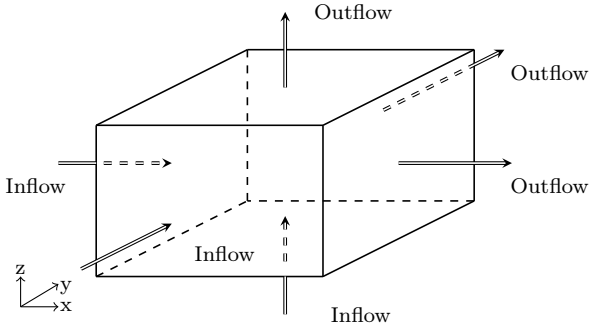

Figure 3.1: A simple control volume.

3.1.1 General conservation equation

An extensive property is a property that is integrable in space and time [7]. In our study, we refer to an extensive property as a mass dependent quantity. Examples include concentration, energy, density and momentum. Let G, denote an amount of such a property in a fluid.

Consider an infinitesimal control volume dV_f, (located inside a fluid of volume V_f) in which a property with density Φ, is moving through it in time t, with velocity $\mathbf{v}$, in a fixed rectangular coordinate system.

The amount of property (∂G) within the small volume dV_f, inside the volume V_f, of the fluid is given by:

$$\partial G = \Phi dV_f. \tag{3.1.1}$$

The total mass of the property inside the whole volume of fluid that occupies a region W, is given by the following integral equation:

$$G(W,t) = \iiint_W \Phi dV_f, \tag{3.1.2}$$

for the sake of simplicity, we shall write the volume integral as $\int_W \Phi dV_f$, instead of $\iiint_W \Phi dV_f$.

We shall now consider total efflux across the boundaries of the volume occupied by the fluid. Let ∂S_f be a small area element with outward unit normal $\mathbf{n}$, which is the boundary of the volume of fluid and let $\mathbf{J}$ be a vector of the convective fluxes of the property G, across the boundaries of the fluid volume i.e.

$$\mathbf{J} = \Phi \mathbf{v_e}. \tag{3.1.3}$$

Then the net flow of the property across the boundaries of volume V_f, is given by:

$$inflow - outflow = -\oint \mathbf{J} \cdot \mathbf{n} \partial S_f. \tag{3.1.4}$$

However, the rate of change of the amount of property inside the volume is equal to the difference between the amount that flows in and the amount that flows out, thus we have:

$$\frac{\partial}{\partial t} G(W,t) = -\oint \mathbf{J} \cdot \mathbf{n} \partial S_f, \tag{3.1.5}$$

The divergence theorem states that:

$$\oint \mathbf{f} \cdot \mathbf{n} dA = \int_W \nabla \cdot \mathbf{f} dV, \tag{3.1.6}$$

where $\mathbf{f}$ is any differentiable vector, dA, dV are infinitesimal area and volume elements, respectively [7]. Applying this theorem, we have:

$$\oint \mathbf{J} \cdot \mathbf{n} dS_f = \int_W \nabla \cdot \mathbf{J} dV_f,$$

thus Equation 3.1.5 becomes:

$$\begin{aligned} &\frac{\partial}{\partial t} G(W,t) + \int_W \nabla \cdot \mathbf{J} dV_f = 0, \\ \implies &\int_W \frac{\partial \Phi}{\partial t} dV_f + \int_W \nabla \cdot \mathbf{J} dV_f = 0, \\ \implies &\int_W \left[\frac{\partial \Phi}{\partial t} + \nabla \cdot \mathbf{J} \right] dV_f = 0. \end{aligned} \tag{3.1.7}$$

The general conservation equation in integral form for the extensive property in a fluid of volume V_f, is given by Equation 3.1.7. However, by the continuum approach we implicitly assumed that the domain is continuous and the properties are differentiable, our interest is to know the instantaneous changes of the property at specific points of the domain. Since we arbitrarily chose the infinitesimal volume, Equation 3.1.7 holds (is true) only if the integrand is zero. Thus due to our interest in obtaining differential equations, we extract the integrand as the differential form of the conservation equation, thus we obtain:

$$\frac{\partial \Phi}{\partial t} + \nabla \cdot \mathbf{J} = 0. \tag{3.1.8}$$

This Equation 3.1.8 is called a microscopic equation and it applies to every point inside the volume of fluid. However, this equation does not describe a situation where there are sources or sinks inside the fluid volume. To account for sources and sinks which appear in the form of reactions and deposition within the volume, we shall include the term S_Φ, in Equation 3.1.8.

Furthermore, we shall identify microscopic coordinates in the microscopic equations by attaching ($'$) to each microscopic independent variable. Thus Equation 3.1.8 is rewritten as follows:

$$\frac{\partial \Phi}{\partial t'} + \nabla' \cdot \mathbf{J} = S_\Phi. \tag{3.1.9}$$

3.1.2 Microscopic mass transport equation

When the general property G, is taken as the fluid mass, the density Φ, is the mass density of the fluid. Let ρ_e be the mass density of the effluent water, then;

$$\Phi = \rho_e. \tag{3.1.10}$$

The mass flux across the control volume boundaries is obtained by substituting Equation 3.1.10 into Equation 3.1.3, thus we obtain:

$$\mathbf{J} = \rho_e \mathbf{v_e}, \tag{3.1.11}$$

where $\mathbf{v_e}$ is the mass average effluent water velocity vector. Let the amount of mass produced or used in the control volume be S_{ρ_e}, then the source term in the general Equation 3.1.9 is given by:

$$S_\Phi = S_{\rho_e}. \tag{3.1.12}$$

By substituting $\Phi = \rho_e$, $S_\Phi = S_{\rho_e}$, and $\mathbf{J} = \rho_e \mathbf{v_e}$ into Equation 3.1.9, the microscopic mass balance for the effluent water is given by:

$$\frac{\partial \rho_e}{\partial t'} + \nabla' \cdot \rho_e \mathbf{v_e} = S_{\rho_e}. \tag{3.1.13}$$

Equation 3.1.13 states that the rate of increase in mass of the fluid inside the control volume is a result of mass fluxes across the boundaries of the control volume and mass sources or sinks inside the control volume. Equation 3.1.13 applies when the fluid is homogeneous (single phase and single component) [7].

3.1.3 Microscopic momentum transport equation

When the property G, is momentum, the density Φ, is the momentum density. However, momentum of the fluid is the product of mass and velocity of the fluid, therefore momentum density which is simply the momentum of the fluid per unit volume is;

$$\Phi = \rho_e \mathbf{v_e}. \tag{3.1.14}$$

Momentum is transported by the convective fluid motion across the boundaries of the control volume, thus by substituting Equation 3.1.14 into Equation 3.1.3 the convective flux $\mathbf{J}$, is given by;

$$\mathbf{J} = \rho_e \mathbf{v_e} \mathbf{v_e}, \tag{3.1.15}$$

Substituting Equations 3.1.14 and 3.1.15 into the general conservation Equation 3.1.9, we obtain:

$$\frac{\partial \rho_e \mathbf{v_e}}{\partial t'} + \nabla' \cdot \rho_e \mathbf{v_e} \mathbf{v_e} = S_\Phi. \tag{3.1.16}$$

Equation 3.1.16 states that the rate of change in momentum of the fluid inside the control volume is equal to the net (resultant) force acting on it (fluid). The forces acting on the fluid can broadly be classified as body forces and surface forces. While the body forces act throughout the fluid, the surface forces act on the surface of the fluid. The surface forces include pressure and viscous forces and the body force is assumed to be due to gravity only. Thus splitting the source term into the body force part and surface force part, we have:

$$\frac{\partial \rho_e \mathbf{v_e}}{\partial t'} + \nabla' \cdot \rho_e \mathbf{v_e} \mathbf{v_e} = \nabla' \cdot \bar{\sigma} + \mathbf{F_b}, \tag{3.1.17}$$

where $\bar{\sigma}$ is a tensor describing the stress on the fluid and $\mathbf{F_b}$ body force per unit volume [7, 36, 51]. The stress tensor is given mathematically by:

$$\bar{\sigma} = -p_e \delta + \bar{\tau}, \tag{3.1.18}$$

where Kronecker delta δ, represents a unit tensor, p_e represents static pressure and $\bar{\tau}$ represents the viscous stress tensor. The body force density (body force per unit volume) $\mathbf{F_b}$, which is due to gravity is given by [7, 51, 36]:

$$\mathbf{F_b} = \rho_e \mathbf{g}, \tag{3.1.19}$$

where $\mathbf{g}$ is the gravitational force per unit mass. Substituting Equations 3.1.19 and 3.1.18 into Equation 3.1.17, we obtain:

$$\frac{\partial \rho_e \mathbf{v_e}}{\partial t'} + \nabla' \cdot \rho_e \mathbf{v_e} \mathbf{v_e} = \nabla' \cdot (-p_e \delta + \bar{\tau}) + \rho_e \mathbf{g}. \tag{3.1.20}$$

Expanding the right hand side of Equation 3.1.20, we have:

$$\frac{\partial \rho_e \mathbf{v_e}}{\partial t'} + \nabla' \cdot \rho_e \mathbf{v_e} \mathbf{v_e} = -\nabla' p_e + \nabla' \cdot \bar{\tau} + \rho_e \mathbf{g}. \tag{3.1.21}$$

It has been shown (by [7, 51, 36, 69]) that the divergence of the viscous stress tensor $(\nabla' \cdot \bar{\tau})$, can be expressed as:

$$\nabla' \cdot \bar{\tau} = \nabla' \cdot \mu_e \nabla' \mathbf{v_e} + \nabla' \mathbf{v_e} \cdot \nabla' \mu_e + \mu_e \nabla' (\nabla' \cdot \mathbf{v_e}) \tag{3.1.22}$$

where μ_e represents viscosity of the fluid. By assumption, the viscosity of the mine effluent water is constant, implying that;

$$\nabla' \mathbf{v_e} \cdot \nabla' \mu_e = 0. \tag{3.1.23}$$

We also assume that the fluid is incompressible (no volume changes due to pressure changes), thus;

$$\mu_e \nabla' \nabla' \cdot \mathbf{v_e} = 0. \tag{3.1.24}$$

Substituting Equation 3.1.22 into Equation 3.1.21 and using information from Equations 3.1.24 and 3.1.23, the microscopic momentum transport equation is given by:

$$\frac{\partial \rho_e \mathbf{v_e}}{\partial t'} + \nabla' \cdot \rho_e \mathbf{v_e} \mathbf{v_e} = -\nabla' p_e + \nabla' \cdot \mu_e \nabla' \mathbf{v_e} + \rho_e \mathbf{g}. \tag{3.1.25}$$

3.1.4 Microscopic energy transport equation

The energy in the control volume is given by the sum of the kinetic and internal energies. When the property G, is energy, then Φ is the energy density. The kinetic energy density (K_e) is given by:

$$K_e = \frac{\rho_e v_e^2}{2}, \tag{3.1.26}$$

where $v_e^2 = \mathbf{v_e} \cdot \mathbf{v_e}$. Let E_n, be the internal energy density, then the total energy density in the control volume is given by:

$$\Phi = E_n + \frac{\rho_e v_e^2}{2}. \tag{3.1.27}$$

By substituting Equation 3.1.27 into Equation 3.1.3, the convective energy flux across the boundaries of the control volume is given by:

$$\mathbf{J} = \left(E_n + \frac{\rho_e v_e^2}{2} \right) \mathbf{v_e}. \tag{3.1.28}$$

Let the energy source or sink term be S_T. Thus, substituting Equations 3.1.27 and 3.1.28 into the general conservation Equation 3.1.9, we obtain:

$$\frac{\partial\left(E_n + \frac{\rho_e v_e^2}{2}\right)}{\partial t'} + \nabla' \cdot \left(E_n + \frac{\rho_e v_e^2}{2}\right)\mathbf{v_e} = S_T. \tag{3.1.29}$$

Equation 3.1.29 states that the rate at which energy changes in the control volume is equal to the sum of convective transfer and other transfers (S_T) [26, 35]. The other forms of energy transfers include work done by body and surface forces, heat generation from energy sources S_{TT}, and conductive transfer [26, 35]. The work done by body forces (W_b) is given by [26, 35, 51]:

$$W_b = \mathbf{v_e} \cdot \rho_e \mathbf{g}. \tag{3.1.30}$$

Work done by the surface forces (W_s) is given by [51, 26, 35]:

$$W_s = \nabla \cdot \bar{\sigma} \cdot \mathbf{v_e}. \tag{3.1.31}$$

Energy transfer by conduction is given by Fourier's law which states that the heat flux across a surface is directly proportional to the temperature gradient [51]. Mathematically, Fourier's law states that:

$$\mathbf{q_c} = -\kappa_e \nabla T_e, \tag{3.1.32}$$

where $\mathbf{q_c}$ is the heat flux, κ_e is the constant of proportionality called thermal conductivity, and T_e is temperature. By Fourier's law, the net energy flux by conduction into the control volume is given by [26]:

$$-\nabla \cdot \mathbf{q_c} = -\nabla' \cdot -\kappa_e \nabla T_e, \tag{3.1.33}$$

the negative sign indicates heat flow from high to low temperature.

Combining Equations 3.1.30, 3.1.31, 3.1.33, the heat source term (S_{TT}) and substituting the result in the right hand of Equation 3.1.29 we obtain:

$$\frac{\partial\left(E_n + \frac{\rho_e v_e^2}{2}\right)}{\partial t'} + \nabla' \cdot \left(E_n + \frac{\rho_e v_e^2}{2}\right)\mathbf{v_e} = \nabla' \cdot \kappa_e \nabla' T_e + S_{TT} + \nabla' \cdot \bar{\sigma} \cdot \mathbf{v_e} + \mathbf{v_e} \cdot \rho_e \mathbf{g}. \tag{3.1.34}$$

Equation 3.1.34 is the energy transport equation obtained by the energy conservation law. However, it can be split into a dissipative part and work done by forces. Since

our interest is the dissipative part, we subtract the part describing work done by forces. Taking a dot product of the fluid velocity and the momentum Equation 3.1.25, we obtain:

$$\frac{\partial \frac{\rho_e v_e^2}{2}}{\partial t'} + \nabla' \cdot \frac{\rho_e v_e^2}{2} \mathbf{v_e} = \mathbf{v_e} \cdot \nabla' \cdot \bar{\sigma} + \mathbf{v_e} \cdot \rho_e \mathbf{g}. \tag{3.1.35}$$

Equation 3.1.35 describes kinetic energy transport only. Subtracting Equation 3.1.35) from Equation 3.1.34, the part describing internal energy transport is given by:

$$\begin{aligned} \frac{\partial E_n}{\partial t'} + \nabla' \cdot E_n \mathbf{v_e} &= \nabla' \cdot \kappa_e \nabla T_e + S_{TT} + \nabla' \cdot \bar{\sigma} \cdot \mathbf{v_e}) - \mathbf{v_e} \cdot \nabla' \cdot \bar{\sigma}, \\ &= \nabla' \cdot \kappa_e \nabla' T_e + S_{TT} + \bar{\sigma} \cdot \nabla' \cdot \mathbf{v_e}, \\ &= \nabla' \cdot \kappa_e \nabla' T_e + S_{TT} - p_e \nabla' \cdot \mathbf{v_e} + \bar{\tau} \cdot \nabla' \cdot \mathbf{v_e}. \end{aligned} \tag{3.1.36}$$

The last term in Equation 3.1.36 accounts for the irreversible viscous dissipation of energy [26]. Thermodynamically, E_n is defined as [26]:

$$E_n = \rho_e h_e - p_e, \tag{3.1.37}$$

where h_e is enthalpy. Substituting Equation 3.1.37 into Equation 3.1.36 and rearranging, we obtain:

$$\frac{\partial \rho_e h_e}{\partial t'} + \nabla' \cdot (\rho_e h_e \mathbf{v_e}) = \nabla' \cdot \kappa_e \nabla' T_e + S_{TT} - \frac{\partial p_e}{\partial t'} - \nabla' \cdot p_e \mathbf{v_e} - p_e \nabla' \cdot \mathbf{v_e} + \bar{\tau} \cdot \nabla' \cdot \mathbf{v_e}. \tag{3.1.38}$$

In the case of constant pressure, the enthalpy h_e is given by [21, 26]:

$$h_e = (C_p)_e T_e \tag{3.1.39}$$

where $(C_p)_e$ heat capacity at constant pressure. Thus substituting Equation 3.1.39 into Equation 3.1.38, the energy transport equation further reduces to the following:

$$\frac{\partial \rho_e (C_p)_e T_e}{\partial t'} + \nabla' \cdot (\rho_e (C_p)_e T_e \mathbf{v_e}) = \nabla' \cdot \kappa_e \nabla' T_e + S_{TT} + \bar{\tau} \cdot \nabla' \cdot \mathbf{v_e}. \tag{3.1.40}$$

The energy transport equation for our study will account for the conductive and convective energy transfer in the fluid phase, and conduction in solid phase with a source term. Therefore, energy transport by the fluid phase is given by:

$$\frac{\partial \rho_e (C_p)_e T_e}{\partial t'} + \nabla' \cdot (\rho_e (C_p)_e T_e \mathbf{v_e}) = \nabla' \cdot \kappa_e \nabla' T_e + S_{TT}, \tag{3.1.41}$$

and energy transport by the solid phase is given by:

$$\frac{\partial \rho_s (C_p)_s T_s}{\partial t'} = \nabla' \cdot \kappa_s \nabla' T_s, \tag{3.1.42}$$

where $\kappa_s, T_s, (C_p)_s,$ and ρ_s are the thermal conductivity, temperature, specific heat capacity at constant pressure, and density of the solid.

3.1.5 Flow development

The mass conservation Equation 3.1.13 is also called continuity Equation. Employing the continuity Equation 3.1.13 and the momentum Equation 3.1.25, a Newtonian fluid flowing freely (outside a porous domain) can be described. We only discuss a case where the effluent water flows between two fixed, parallel and impermeable walls separated by some distance (see Figure 3.2). This type of flow is commonly called Plane Poiseuille flow.

For such a flow, a uniform entrance velocity profile changes until the velocity profile is parabolic (in a 2-D flow case) or the fluid exits the domain, this is called flow development [29, 35]. Figure 3.3 illustrates flow development in the empty channel.

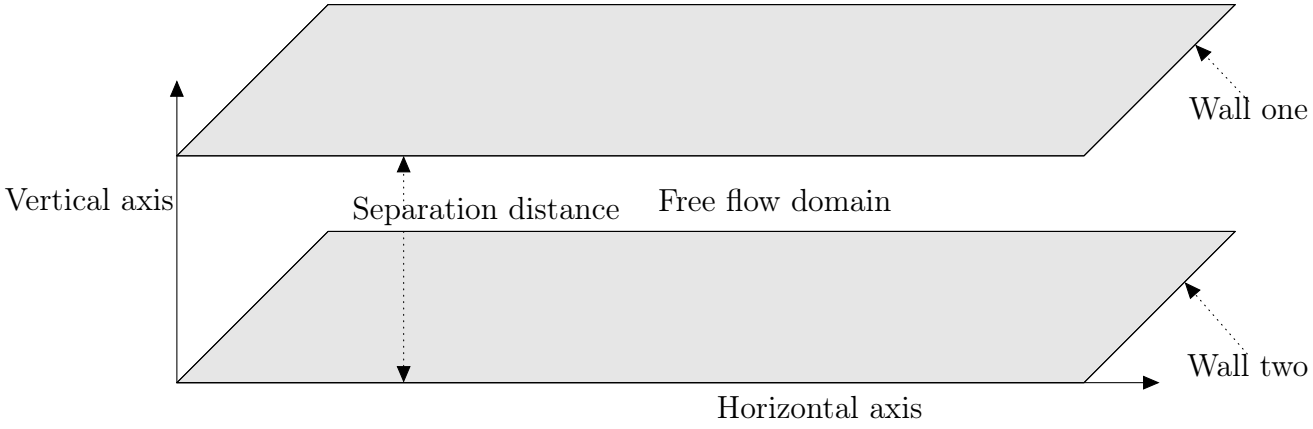

Figure 3.2: A simple free flow domain.

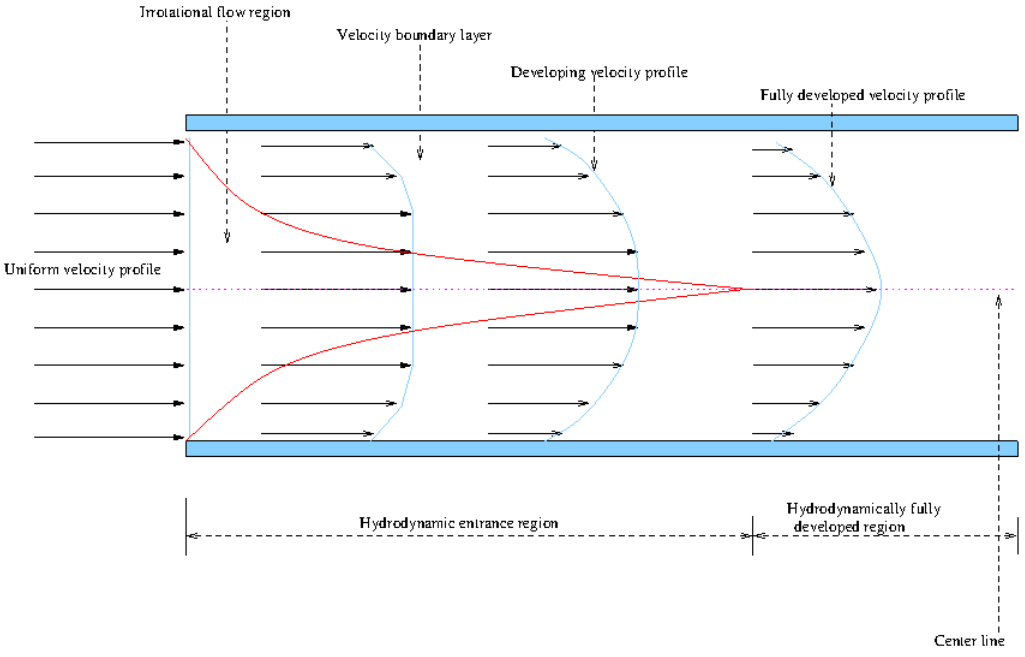

Figure 3.3: A schematic illustrating flow development.

Moving fluid particles come to a complete stop when in contact with a boundary (wall), this is called no-slip [29, 35]. The stationary fluid particles in contact with the wall also cause adjacent fluid particles to come to a stop due to fluid friction. To conserve fluid mass in the flow process, the fluid velocity at the mid-section of the domain increases, thus establishing a velocity gradient and destroying the uniform profile [29, 35]. The region where the fluid particles are at rest is called the boundary layer [35, 29]. The flow is divided into two regions due to the boundary layer formation, i.e. the "boundary layer" region and the "irrotational (core)" flow region [35, 29].

The boundary layer thickness increases in the flow direction until both boundary layers (at each wall) merge at the center of the domain. The region between the domain inlet and the point where the boundary layers intersect is called the entrance region, and the length of the entrance region is called entrance length [29, 35]. Fluid flow in the entrance region is called hydrodynamically developing flow. The region beyond the entrance region is called fully developed region [29, 35]. In the fully developed region the velocity profile is parabolic and there is no further changes in the profile [29].

Flow development can be described by solving steady forms of Equation 3.1.13 and Equation 3.1.25. Figures 3.4 and 3.5 are graphs of horizontal velocity component against vertical distance, for specific horizontal distances.

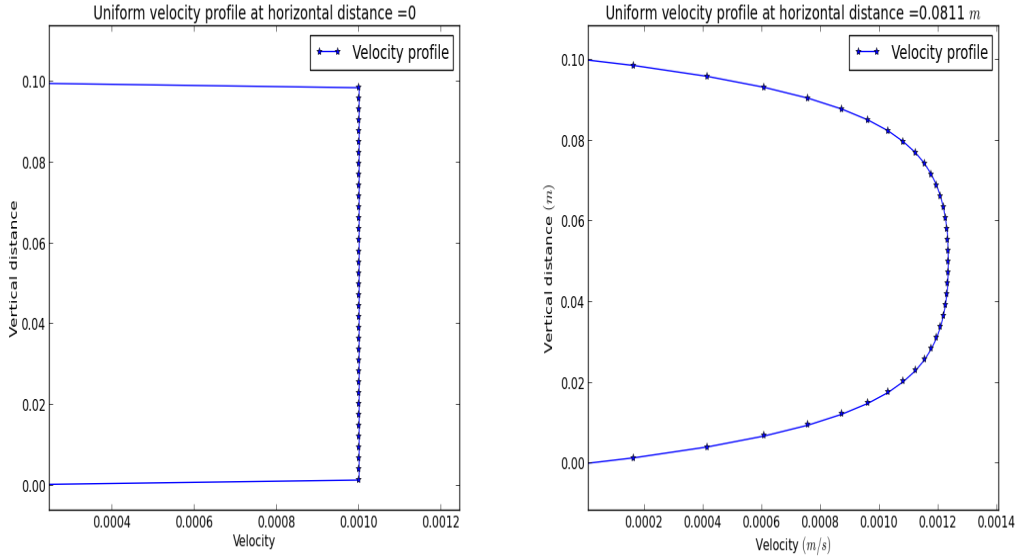

Figure 3.4: Flow development profiles

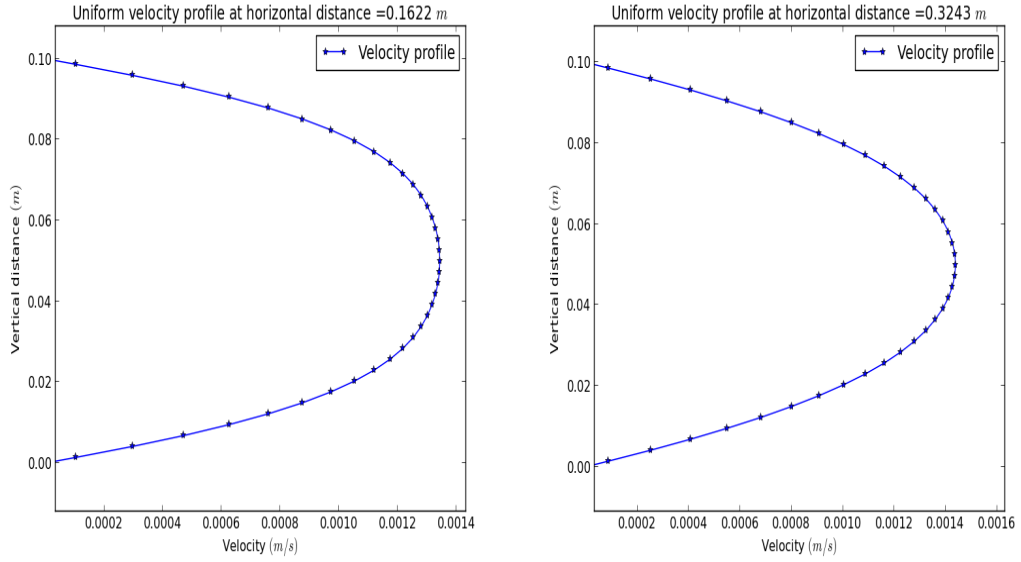

Figure 3.5: Flow development profiles

The graph at left hand side of Figure 3.4 is the uniform entrance velocity profile and the graph at right hand side of Figure 3.4 is the velocity profile at a short distance from the entrance. The graph at the right hand side of Figure 3.5 shows the fully developed velocity profile. It can be observed that, the velocity profiles clearly illustrate flow development.

3.2 Macroscopic Modelling

The microscopic description considers the transport phenomena at every mathematical point within any phase (considered as a continuum). In principle this method is feasible, since the resulting microscopic model can be used to describe phenomena in the pore length scale. However, due to our inability to measure quantities at the pore level, coupled with large length scale problems usually encountered in practical cases, and due to our inability to describe the complicated geometry of the porous domain, the microscopic description is not employed in practical problems involving phenomena in porous structures. Figure 3.6 illustrates the complicated geometry of a porous domain.

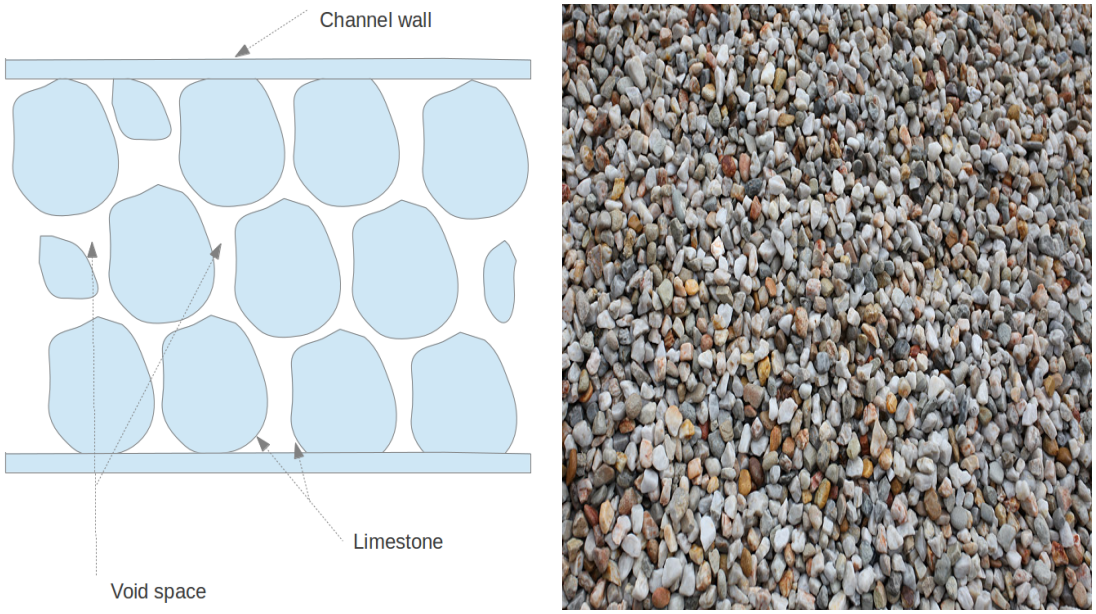

Figure 3.6: Schematic and real porous media.

An alternative modelling approach that circumvents the problems listed in the previous paragraph, is a higher continuum approach (macroscopic) in which the real porous domain is replaced by a fictitious continuum [69, 70, 7, 31]. The method considers matter present in the domain as continuum which completely fills the domain. Thus, if the matter is composed of multi-phases, each phase is treated as continuum. Which further implies that, a multi-phase domain is simply a set of overlapping continua that are interacting [69, 70]. The difficulties encountered with the microscopic method are overcome by averaging

over a small volume domain located in the porous medium called an elementary volume. The average of a variable is taken over an elementary volume and assigned to the centroid of that volume. This averaged value is called a macroscopic value [69, 70].

The higher continuum approach and the representative elementary volume (REV) concepts are not new, see the next section for a detailed discussion of REV. Many researchers have elaborated these concepts in detail [69, 24, 41, 68, 27, 57, 46], however in this work, we employ those concepts as part of literature review and methodology to derive a mathematical model for the AMD process.

The assumptions used in this section include: constant viscosity, constant thermal conductivity and constant specific heat capacity for the effluent water. The limestone is assumed to be isotropic and homogeneous. No-slip condition applies to fluid-solid interfaces.

3.2.1 Representative elementary volume

A sample elementary volume of the porous domain which always consist of a void space and a solid phase, that represents a mathematical/physical point, and returns a constant averaged value is called a REV [69, 7, 60]. Figure 3.7 is a simple representative elementary volume.

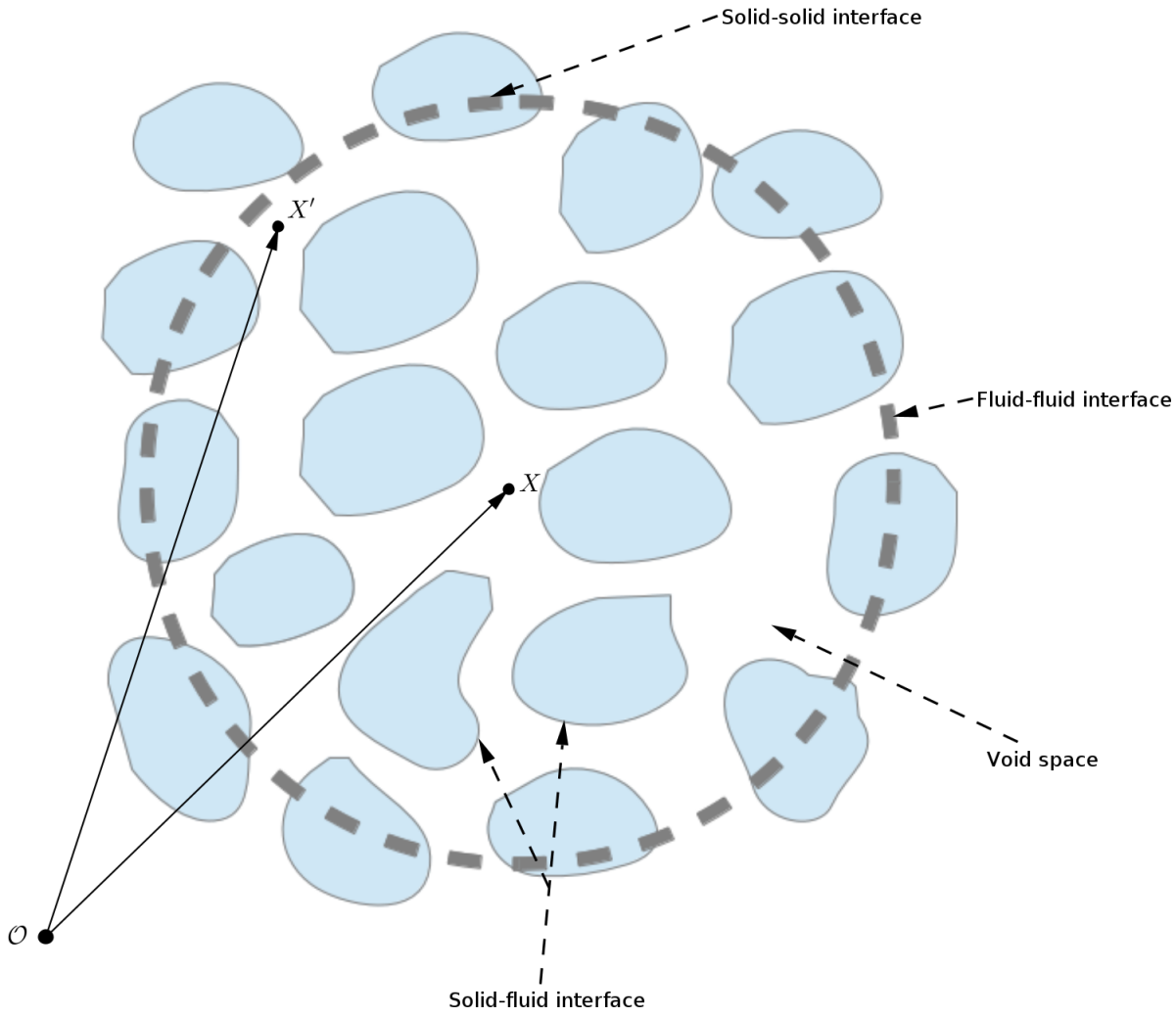

Figure 3.7: A Representative Elementary Volume.

Void space is the area that the fluid either occupies or flow through in the porous medium. Between the solid phase and the void space is an interface called solid-fluid interface (denoted by A_{sf} in Figure 3.7). Other interfaces include fluid-fluid and solid-solid interfaces located at the REV boundaries [69].

Two important theorems are used to obtain macroscopic models from microscopic model. These theorems are Slattery's theorem and volume averaging theorem.

3.2.2 Volume averaging and Slattery's theorem

Let X' denote a point in the volume V_f of fluid located inside the REV of size V, and let X denote the position of the REV's centroid in a fixed coordinate system.

An intrinsic volume average of a property is the amount of that property present in a unit phase volume of an REV. The intrinsic phase average is used when the parameters or variables of interest are physically measured per phase. For the property G, an intrinsic volume average over the fluid phase of an REV is defined by [19]:

$$\langle G\rangle^f(X,t) = \frac{1}{V_f(X,t)}\int_{V_f(X,t)} G(X',t)dV_f(X'). \tag{3.2.1}$$

and the intrinsic average of the solid phase is given by:

$$\langle G\rangle^s(X,t) = \frac{1}{V_s(X,t)}\int_{V_s(X,t)} G(X',t)dV_s(X'). \tag{3.2.2}$$

where V_s is the volume of the solid phase in the REV.

Parameters can also be given or measured per unit volume of the REV instead of phase volume, these parameters or variables are called superficial parameters or variables. Superficial variables are obtained directly by averaging over an REV, the procedure is called superficial averaging. The formula for superficial averaging is defined by [19]:

$$\langle G\rangle(X,t) = \frac{1}{V(X,t)}\int_{V(X,t)} G(X',t)dV(X') = \varepsilon_f\langle G\rangle^f \tag{3.2.3}$$

where:

$$\varepsilon_f = \frac{V_f}{V}, \tag{3.2.4}$$

is the volumetric porosity of the fluid phase. The sum of the void fraction and the solid phase fraction of the REV is unity, thus we have:

$$\varepsilon_s + \varepsilon_f = 1, \tag{3.2.5}$$

where ε_s is the solid phase fraction of the REV. Since the macroscopic value or variable (the averaged value assigned to the centroid) of the REV is a mean of microscopic values or variables at any point inside the REV, then any microscopic value or variable inside that same REV can be expressed in terms of the the mean and a deviation, thus we have:

$$G(X',t;X) = \langle G\rangle(X,t) + \Phi'(X',t;X) \tag{3.2.6}$$

or:

$$G(X',t;X) = \langle G \rangle^f (X,t) + G'(X',t;X), \tag{3.2.7}$$

where $G'(X',t;X)$ is deviation of the property G, at position X' in time t, from the averaged value assigned to the centroid of the REV. Equation 3.2.6 expresses the microscopic property in terms of the superficial average, and Equation 3.2.7 expresses the microscopic property in terms of the intrinsic average. Henceforth, we omit the functional arguments $(X',t;X)$, thus $G'(X',t;X)$ will be written simply as G'.

Each term in the microscopic equations must be averaged to obtain macroscopic terms. However, it can be observed that almost all the terms in the equation are derivatives. Thus when the averaging theorems are applied to the derivatives, the resulting terms will need further treatment. Slattery proposed a theorem that relates the average of derivatives to derivatives of average, this theorem is given by [69, 19]:

$$\langle \nabla G \rangle = \nabla \langle G \rangle + \frac{1}{V} \int_{A_{sf}} G \mathbf{n} dA, \tag{3.2.8}$$

where $\mathbf{n}$ is a unit outward normal pointing from the fluid phase towards the solid phase.

The average of the time derivative is related to the time derivative of an averaged quantity, by [69] :

$$\langle \partial_t' G \rangle = \partial_t \langle G \rangle - \frac{1}{V} \int_{A_{sf}} G \mathbf{v_{esf}} \cdot \mathbf{n} dA, \tag{3.2.9}$$

where $\mathbf{v_{esf}}$ is the velocity of the solid-fluid interface (A_{sf}), and $\partial_t' = \frac{\partial}{\partial t'}$ is a microscopic time derivative.

Other rules used in the volume averaging procedure include [69]:

$$\langle \nabla' G \rangle = \varepsilon_f \nabla \langle G \rangle^f + \frac{1}{V} \int_{A_{sf}} G' \mathbf{n} dA. \tag{3.2.10}$$

Mean of sum rule:

$$\langle G_1 + G_2 \rangle = \langle G_1 \rangle + \langle G_2 \rangle, \tag{3.2.11}$$

where G_1 and G_2 are extensive properties.

Mean of product rule:

$$\langle G_1 G_2 \rangle = \langle G_1 \rangle \langle G_2 \rangle + \langle G_1' G_2' \rangle. \tag{3.2.12}$$

Mean of scalar constant product:

$$\langle \alpha_{constant} G \rangle = \alpha_{constant} \langle G \rangle, \tag{3.2.13}$$

where $\alpha_{constant}$ is any constant.

The mean of the deviations in Equation 3.2.7 and Equation 3.2.6 is zero, thus we have:

$$\langle G' \rangle = 0 \quad \text{and} \quad \langle G' \rangle^f = 0. \tag{3.2.14}$$

3.2.3 Macroscopic continuity equation

Applying the volume averaging theorem given by Equation 3.2.8 to the microscopic continuity Equation 3.1.13, we obtain:

$$\langle \frac{\partial \rho_e}{\partial t'} + \nabla' \cdot (\rho_e \mathbf{v_e}) \rangle = \langle S_{\rho_e} \rangle. \tag{3.2.15}$$

Applying rule 3.2.11 to Equation 3.2.15, we obtain:

$$\langle \frac{\partial \rho_e}{\partial t'} \rangle + \langle \nabla' \cdot (\rho_e \mathbf{v_e}) \rangle = \langle S_{\rho_e} \rangle. \tag{3.2.16}$$

Replacing the gradient operator in Slattery's theorem given by 3.2.8 with a divergence operator, and applying the results to the second term in Equation 3.2.16, we obtain:

$$\langle \nabla' \cdot (\rho_e \mathbf{v_e}) \rangle = \nabla \cdot \langle (\rho_e \mathbf{v_e}) \rangle + \frac{1}{V} \int_{A_{sf}} \rho_e \mathbf{v_e} \cdot \mathbf{n} dA \tag{3.2.17}$$

Applying no-slip condition (i. e. $\mathbf{v_e} \cdot \mathbf{n} = 0$), the integral term vanishes. The density ρ_e and the velocity are expressed in terms of their intrinsic mean and deviations by using Equation 3.2.6, thus $\rho_e = \langle \rho_e \rangle^f + \rho_e'$ and $\mathbf{v_e} = \langle \mathbf{v_e} \rangle^f + \mathbf{v_e'}$, where $\mathbf{v_e'}$ is the velocity deviation from the mean velocity, and ρ_e' is the density deviation from the mean density. Substituting into Equation 3.2.17 :

$$\langle \nabla' \cdot (\rho_e \mathbf{v_e}) \rangle = \nabla \cdot \Big(\langle \big(\langle \rho_e \rangle^f + \rho_e' \big) \big(\langle \mathbf{v_e} \rangle^f + \mathbf{v_e'} \big) \rangle \Big) \tag{3.2.18}$$

Expanding Equation 3.2.18, we obtain:

$$\begin{aligned}\langle \nabla' \cdot (\rho_e \mathbf{v_e}) \rangle &= \nabla \cdot \Big(\langle \big(\langle \rho_e \rangle^f + \rho_e' \big) \big(\langle \mathbf{v_e} \rangle^f + \mathbf{v_e'} \big) \rangle \Big) \\ &= \nabla \cdot \Big(\langle \big(\langle \rho_e \rangle^f \langle \mathbf{v_e} \rangle^f + \rho_e' \langle \mathbf{v_e} \rangle^f + \langle \rho_e \rangle^f \mathbf{v_e'} + \rho_e' \mathbf{v_e'} \big) \rangle \Big) \\ &= \nabla \cdot \Big(\langle \langle \rho_e \rangle^f \langle \mathbf{v_e} \rangle^f \rangle + \langle \rho_e' \langle \mathbf{v_e} \rangle^f \rangle + \langle \langle \rho_e \rangle^f \mathbf{v_e'} \rangle + \langle \rho_e' \mathbf{v_e'} \rangle \Big). \end{aligned} \tag{3.2.19}$$

Replacing the superficial average in Equation 3.2.19 by the intrinsic average and applying rule 3.2.13 to the results, we obtain:

$$\begin{aligned}\langle \nabla' \cdot (\rho_e \mathbf{v_e}) \rangle = \nabla \cdot \Big(& \varepsilon_f \langle \rho_e \rangle^f \langle \mathbf{v_e} \rangle^f \langle 1 \rangle^f + \varepsilon_f \langle \rho_e' \rangle^f \langle \mathbf{v_e} \rangle^f \\ & + \varepsilon_f \langle \rho_e \rangle^f \langle \mathbf{v_e'} \rangle^f + \varepsilon_f \langle \rho_e' \mathbf{v_e'} \rangle^f \Big). \end{aligned} \tag{3.2.20}$$

Since the average of a constant is the constant, and the average of a deviation is zero (according to rule 3.2.14), then Equation 3.2.20 can be written as follows:

$$\begin{aligned}\langle \nabla' \cdot (\rho_e \mathbf{v_e}) \rangle &= \nabla \cdot \Big(\varepsilon_f \langle \rho_e \rangle^f \langle \mathbf{v_e} \rangle^f + \varepsilon_f \langle \rho_e' \mathbf{v_e'} \rangle^f \Big), \\ &= \nabla \cdot \Big(\varepsilon_f \langle \rho_e \rangle^f \langle \mathbf{v_e} \rangle^f \Big) + \nabla \cdot \Big(\varepsilon_f \langle \rho_e' \mathbf{v_e'} \rangle^f \Big). \end{aligned} \tag{3.2.21}$$

The average of the time derivative in Equation 3.2.16 can also be expanded by applying Equation 3.2.9. thus we obtain:

$$\langle \frac{\partial \rho_e}{\partial t'} \rangle = \frac{\partial \langle \rho_e \rangle}{\partial t} - \frac{1}{V} \int_{A_{sf}} \rho_e \mathbf{v_{esf}} \cdot \mathbf{n} dA. \tag{3.2.22}$$

Replacing the first term of Equation 3.2.16 by the right hand side of Equation 3.2.22, and also replacing the second term left hand side of 3.2.16 by the right hand side of Equation 3.2.21, the macroscopic continuity equation for the effluent water is given by:

$$\begin{aligned}\frac{\partial \varepsilon_f \langle \rho_e \rangle^f}{\partial t} + \nabla \cdot \Big(\varepsilon_f \langle \rho_e \rangle^f \langle \mathbf{v_e} \rangle^f \Big) + \nabla \cdot \Big(\varepsilon_f \langle \rho_e' \mathbf{v_e'} \rangle^f \Big) = \varepsilon_f \langle S_{\rho_e} \rangle^f \\ + \frac{1}{V} \int_{A_{sf}} \rho_e \mathbf{v_{esf}} \cdot \mathbf{n} dA. \end{aligned} \tag{3.2.23}$$

Equation 3.2.23 is the macroscopic mass balance for a homogeneous (a single) fluid flowing through a porous medium. It describes a flow through a homogeneous medium whose

porosity changes in time and space [7]. The first term at the left hand side of Equation 3.2.23 accounts for the rate at which the mass density is changing with time in the domain. The second term (left hand side of Equation 3.2.23) is the convection term, which describes the rate at which mass is transported across domain boundaries by convection. The third term (left hand side of Equation 3.2.23) is the dispersion term, it quantifies mass transport relative to convection. The first term right hand side is the averaged source term, and the last term is a source term that quantifies inter-phase transfer of mass.

3.2.4 Contaminant transport and carrier fluid continuity equations

The mine effluent water can be separated into pure water and contaminants by physical or chemical methods. The density and other parameters of the effluent water is the sum of the parameters for the pure water and the contaminants. Thus the mine effluent water density $\langle \rho_e \rangle^f$, can be written as;

$$\langle \rho_e \rangle^f = \langle \rho_w \rangle^f + \langle \rho_c \rangle^f, \tag{3.2.24}$$

where $\langle \rho_w \rangle^f$ is the intrinsic density of water and $\langle \rho_c \rangle^f$ is the intrinsic density of the contaminants.

Substituting the right hand side of Equation 3.2.24 into the macroscopic continuity Equation 3.2.23, we obtain:

$$\begin{aligned} &\frac{\partial \varepsilon_f \left(\langle \rho_w \rangle^f + \langle \rho_c \rangle^f \right)}{\partial t} + \nabla \cdot \left(\varepsilon_f \left(\langle \rho_w \rangle^f + \langle \rho_c \rangle^f \right) \langle \mathbf{v_e} \rangle^f \right) + \nabla \cdot \left(\varepsilon_f \langle \rho_e' \mathbf{v_e'} \rangle^f \right) \\ &= \varepsilon_f \langle S_{\rho_w} \rangle^f + \varepsilon_f \langle S_{\rho_c} \rangle^f + S_{RC}, \end{aligned} \tag{3.2.25}$$

where $S_{RC} = \frac{1}{V} \int_{A_{sf}} \rho_e \mathbf{v_{esf}} \cdot \mathbf{n} dA$, and $\langle S_{\rho_e} \rangle^f = \langle S_{\rho_w} \rangle^f + \langle S_{\rho_c} \rangle^f$.

Equation 3.2.25 can be split into the pure water transport equation;

$$\frac{\partial \varepsilon_f \langle \rho_w \rangle^f}{\partial t} + \nabla \cdot \left(\varepsilon_f \langle \rho_w \rangle^f \langle \mathbf{v_e} \rangle^f \right) = \varepsilon_f \langle S_{\rho_w} \rangle^f, \tag{3.2.26}$$

and the contaminant transport equation:

$$\frac{\partial \varepsilon_f \langle \rho_c \rangle^f}{\partial t} + \nabla \cdot \left(\varepsilon_f \langle \rho_c \rangle^f \langle \mathbf{v_e} \rangle^f \right) + \nabla \cdot \left(\varepsilon_f \langle \rho_e' \mathbf{v_e'} \rangle^f \right) = \varepsilon_f \langle S_{\rho_c} \rangle^f + S_{RC}. \tag{3.2.27}$$

Equation 3.2.27 requires closure since the dispersion term contains variables that cannot be written into separate mean values. The dispersive flux $\langle \rho_e' \mathbf{v_e'} \rangle^f$, is related to the gradient of the mass density [7] by:

$$\langle \rho_e' \mathbf{v_e'} \rangle^f = -\bar{\mathbf{D}} \cdot \nabla \langle \rho_c \rangle, \tag{3.2.28}$$

where $\bar{\mathbf{D}}$ is a second-rank tensor called coefficient of mechanical dispersion. Replacing the dispersive flux in Equation 3.2.27 with the right hand side of Equation 3.2.28, we obtain:

$$\frac{\partial \varepsilon_f \langle \rho_c \rangle^f}{\partial t} + \nabla \cdot \left(\varepsilon_f \langle \rho_c \rangle^f \langle \mathbf{v_e} \rangle^f \right) - \nabla \cdot \left(\varepsilon_f \bar{\mathbf{D}} \cdot \nabla \langle \rho_c \rangle \right) = \varepsilon_f \langle S_{\rho_c} \rangle^f + S_{RC}. \tag{3.2.29}$$

The pure water is the component of the effluent water that is in excess, therefore dominates in the flow process. The dominant fluid or component is called carrier fluid [30]. The flow parameters from the contaminants are considered negligible as compared with the flow parameters for the carrier fluid. Thus the flow parameters in the continuity, momentum and energy equations for the mine effluent water are approximated by parameters for pure water. In the continuity Equation 3.2.25 for the pure water, the source term accounts for the water that is produced during chemical reaction, but comparing the source to the flowing fluid, the source is negligible. Since the density and porosity are assumed constant, the macroscopic continuity equation for the carrier fluid (water) is given by:

$$\nabla \cdot \mathbf{v_e} \rangle^f = 0. \tag{3.2.30}$$

Moreover, the water contaminant is a mixture of chemical species. The goal in this Chapter is to obtain a transport equation for each chemical species. The density of the contaminants is the sum of the densities of all the chemical species present in the effluent water, thus we have:

$$\langle \rho_c \rangle^f = \sum_{k=1}^{N_{spe}} \langle \rho_k \rangle^f, \tag{3.2.31}$$

where $\langle \rho_k \rangle^f$ is the density of the k^{th} chemical species, and N_{spe} is the total number of chemical species present in the water. The fraction of each chemical species is called mass fraction [30], [28]. The mass fraction (ω_k) of species k, is defined as:

$$\omega_k = \frac{\langle \rho_k \rangle^f}{\langle \rho_c \rangle^f}. \tag{3.2.32}$$

The macroscopic transport equation for each species is obtained by multiplying the mass fraction ω_k, by each term in the contaminant Equation 3.2.29. Thus we obtain:

$$\frac{\partial \varepsilon_f \omega_k \langle \rho_c \rangle^f}{\partial t} + \nabla \cdot \left(\varepsilon_f \omega_k \langle \rho_c \rangle^f \langle \mathbf{v_e} \rangle^f \right) - \nabla \cdot \left(\varepsilon_f \bar{\mathbf{D}} \cdot \nabla \omega_k \langle \rho_c \rangle \right) = S_k, \tag{3.2.33}$$

where $S_k = \omega_k \Big(\varepsilon_f \langle S_{\rho_c} \rangle^f + S_{RC} \Big)$, is the portion of the source mass for the k^{th} chemical species. The product $\omega_k \langle \rho_c \rangle^f = C_k$ in Equation 3.2.33 is the mass concentration of species k, thus we can rewrite Equation 3.2.33 as:

$$\frac{\partial \varepsilon_f C_k}{\partial t} + \nabla \cdot \left(\varepsilon_f \langle \mathbf{v_e} \rangle^f C_k \right) - \nabla \cdot \left(\varepsilon_f \bar{\mathbf{D}} \cdot \nabla C_k \right) = S_k. \tag{3.2.34}$$

3.2.5 Hydrogen ion transport equation

When $k = 1$, Equation 3.2.34 is the transport equation for H^+ ions, thus we have:

$$\frac{\partial \varepsilon_f C_1}{\partial t} + \nabla \cdot \left(\varepsilon_f \langle \mathbf{v_e} \rangle^f C_1 \right) - \nabla \cdot \left(\varepsilon_f \bar{\mathbf{D}} \cdot \nabla C_1 \right) = S_1. \tag{3.2.35}$$

For closure of Equation 3.2.35, we substitute S_1 using Equation 2.8.2, thus we obtain:

$$\begin{aligned} &\frac{\partial \varepsilon_f C_1}{\partial t} + \nabla \cdot \left(\varepsilon_f \langle \mathbf{v_e} \rangle^f C_1 \right) - \nabla \cdot \left(\varepsilon_f \bar{\mathbf{D}} \cdot \nabla C_1 \right) \\ &= -K_f \big((1 - \theta_c) \mathcal{B}(\theta_f) \big) \theta_L C_1 + 0.00040984 K_b C_6 C_8. \end{aligned} \tag{3.2.36}$$

3.2.6 Ferric ion transport equation

When $k = 2$, Equation 3.2.34 is the transport equation for Fe^{3+} ions, thus we have:

$$\frac{\partial \varepsilon_f C_2}{\partial t} + \nabla \cdot \left(\varepsilon_f \langle \mathbf{v_e} \rangle^f C_2\right) - \nabla \cdot \left(\varepsilon_f \bar{\mathbf{D}} \cdot \nabla C_2\right) = S_2. \tag{3.2.37}$$

For closure of Equation 3.2.37, we substitute S_2 using Equation 2.4.1, thus we obtain:

$$\frac{\partial \varepsilon_f C_1}{\partial t} + \nabla \cdot \left(\varepsilon_f \langle \mathbf{v_e} \rangle^f C_1\right) - \nabla \cdot \left(\varepsilon_f \bar{\mathbf{D}} \cdot \nabla C_1\right) = K_o C_3 C_7. \tag{3.2.38}$$

3.2.7 Ferrous ion transport equation

When $k = 3$, Equation 3.2.34 is the transport equation for Fe^{2+} ions, thus we have:

$$\frac{\partial \varepsilon_f C_3}{\partial t} + \nabla \cdot \left(\varepsilon_f \langle \mathbf{v_e} \rangle^f C_3\right) - \nabla \cdot \left(\varepsilon_f \bar{\mathbf{D}} \cdot \nabla C_3\right) = S_3. \tag{3.2.39}$$

For closure of Equation 3.2.39, we substitute S_3 using Equation 2.3.10 to obtain:

$$\frac{\partial \varepsilon_f C_3}{\partial t} + \nabla \cdot \left(\varepsilon_f \langle \mathbf{v_e} \rangle^f C_3\right) - \nabla \cdot \left(\varepsilon_f \bar{\mathbf{D}} \cdot \nabla C_3\right) = -K_o C_3 C_7. \tag{3.2.40}$$

3.2.8 'Yellowboy' transport equation

When $k = 2$, Equation 3.2.34 is the transport equation for $Fe(OH)_3$, thus we have:

$$\frac{\partial \varepsilon_f C_4}{\partial t} + \nabla \cdot \left(\varepsilon_f \langle \mathbf{v_e} \rangle^f C_4\right) - \nabla \cdot \left(\varepsilon_f \bar{\mathbf{D}} \cdot \nabla C_4\right) = S_4. \tag{3.2.41}$$

For closure of Equation 3.2.41, we substitute S_4 using Equation 2.6.9 to obtain:

$$\frac{\partial \varepsilon_f C_4}{\partial t} + \nabla \cdot \left(\varepsilon_f \langle \mathbf{v_e} \rangle^f C_4\right) - \nabla \cdot \left(\varepsilon_f \bar{\mathbf{D}} \cdot \nabla C_4\right) = -\theta_c \theta_L K_{dep,f} \mathcal{B}(\theta_f) C_4. \tag{3.2.42}$$

3.2.9 Sulphate ion transport equation

When $k = 5$, Equation 3.2.34 is the transport equation for SO_4^{2-} ion, thus we have:

$$\frac{\partial \varepsilon_f C_5}{\partial t} + \nabla \cdot \left(\varepsilon_f \langle \mathbf{v_e} \rangle^f C_5\right) - \nabla \cdot \left(\varepsilon_f \bar{\mathbf{D}} \cdot \nabla C_5\right) = S_5. \tag{3.2.43}$$

This ion has no source or sink, thus we substitute $S_5 = 0$ into Equation 3.2.43 to obtain:

$$\frac{\partial \varepsilon_f C_5}{\partial t} + \nabla \cdot \left(\varepsilon_f \langle \mathbf{v_e} \rangle^f C_5\right) - \nabla \cdot \left(\varepsilon_f \bar{\mathbf{D}} \cdot \nabla C_5\right) = 0. \tag{3.2.44}$$

3.2.10 Calcium ion transport equation

When $k = 6$, Equation 3.2.34 is the transport equation for Ca^{2+} ion, thus we have:

$$\frac{\partial \varepsilon_f C_6}{\partial t} + \nabla \cdot \left(\varepsilon_f \langle \mathbf{v_e} \rangle^f C_6\right) - \nabla \cdot \left(\varepsilon_f \bar{\mathbf{D}} \cdot \nabla C_6\right) = S_6. \tag{3.2.45}$$

For closure of Equation 3.2.45, we substitute S_6 using Equation 2.9.2 to obtain:

$$\begin{aligned} &\frac{\partial \varepsilon_f C_6}{\partial t} + \nabla \cdot \left(\varepsilon_f \langle \mathbf{v_e} \rangle^f C_6\right) - \nabla \cdot \left(\varepsilon_f \bar{\mathbf{D}} \cdot \nabla C_6\right) \\ &= 40 K_f \big((1 - \theta_c)\mathcal{B}(\theta_f)\big)\theta_L C_1 - 0.0164 K_b C_6 C_8. \end{aligned} \tag{3.2.46}$$

3.2.11 Oxygen transport equation

When $k = 7$, Equation 3.2.34 is the transport equation for O_2, thus we have:

$$\frac{\partial \varepsilon_f C_7}{\partial t} + \nabla \cdot \left(\varepsilon_f \langle \mathbf{v_e} \rangle^f C_7\right) - \nabla \cdot \left(\varepsilon_f \bar{\mathbf{D}} \cdot \nabla C_7\right) = S_7. \tag{3.2.47}$$

For closure of Equation 3.2.47, we substitute S_7 using Equation 2.5.1 to obtain:

$$\frac{\partial \varepsilon_f C_6}{\partial t} + \nabla \cdot \left(\varepsilon_f \langle \mathbf{v_e} \rangle^f C_6\right) - \nabla \cdot \left(\varepsilon_f \bar{\mathbf{D}} \cdot \nabla C_6\right) = -0.25 K_o C_3 C_7. \tag{3.2.48}$$

3.2.12 HCO_3^- transport equation

When $k = 8$, Equation 3.2.34 is the transport equation for HCO_3^- ion, thus we have:

$$\frac{\partial \varepsilon_f C_8}{\partial t} + \nabla \cdot \left(\varepsilon_f \langle \mathbf{v_e} \rangle^f C_8\right) - \nabla \cdot \left(\varepsilon_f \bar{\mathbf{D}} \cdot \nabla C_8\right) = S_8. \tag{3.2.49}$$

For closure of Equation 3.2.49, we substitute S_8 using Equation 2.10.2 to obtain:

$$\begin{aligned} &\frac{\partial \varepsilon_f C_8}{\partial t} + \nabla \cdot \left(\varepsilon_f \langle \mathbf{v_e} \rangle^f C_8\right) - \nabla \cdot \left(\varepsilon_f \bar{\mathbf{D}} \cdot \nabla C_8\right) \\ &= 61 K_f \big((1-\theta_c)\mathcal{B}(\theta_f)\big)\theta_L C_1 - 0.025 K_b C_6 C_8. \end{aligned} \tag{3.2.50}$$

3.2.13 Macroscopic momentum equation

Applying the volume averaging theorem given by Equation 3.2.8 to the microscopic momentum Equation 3.1.25, we obtain:

$$\langle \frac{\partial \rho_e \mathbf{v_e}}{\partial t'} + \nabla' \cdot (\rho_e \mathbf{v_e} \mathbf{v_e}) \rangle = \langle -\nabla' p_e + \nabla' \cdot (\mu_e \nabla' \mathbf{v_e}) + \rho_e \mathbf{g} \rangle. \tag{3.2.51}$$

Applying rule 3.2.11 to Equation 3.2.51, we obtain:

$$\langle \frac{\partial \rho_e \mathbf{v_e}}{\partial t'} \rangle + \langle \nabla' \cdot (\rho_e \mathbf{v_e} \mathbf{v_e}) \rangle = -\langle \nabla' p_e \rangle + \langle \nabla' \cdot (\mu_e \nabla' \mathbf{v_e}) \rangle + \langle \rho_e \mathbf{g} \rangle. \tag{3.2.52}$$

The averaged time derivative in Equation 3.2.52 is expanded by applying Equation 3.2.9, thus we obtain:

$$\langle \frac{\partial \rho_e \mathbf{v_e}}{\partial t'} \rangle = \frac{\partial \langle \rho_e \mathbf{v_e} \rangle}{\partial t} - \frac{1}{V} \int_{A_{sf}} \rho_e \mathbf{v_e} \mathbf{v_{esf}} \cdot \mathbf{n} dA. \tag{3.2.53}$$

We want to obtain the derivatives of averaged quantities and not the average of derivatives thus, we can write the microscopic velocity and density as sums of intrinsic averages and deviations. Thus substituting $\mathbf{v_e} = \langle \mathbf{v_e} \rangle^f + \mathbf{v'_e}$, and $\rho_e = \langle \rho_e \rangle^f + \rho'_e$ into first term at the right hand side of Equation 3.2.53, we obtain:

$$\langle \frac{\partial \rho_e \mathbf{v_e}}{\partial t'} \rangle = \frac{\partial \langle \Big(\langle \rho_e \rangle^f + \rho'_e \Big) \Big(\langle \mathbf{v_e} \rangle^f + \mathbf{v'_e} \Big) \rangle}{\partial t} - \frac{1}{V} \int_{A_{sf}} \rho_e \mathbf{v_e} \mathbf{v_{esf}} \cdot \mathbf{n} dA. \tag{3.2.54}$$

Expanding Equation 3.2.54, we obtain:

$$\begin{aligned} \langle \frac{\partial \rho_e \mathbf{v_e}}{\partial t'} \rangle = \frac{\partial}{\partial t} \Big(\langle \langle \rho_e \rangle^f \langle \mathbf{v_e} \rangle^f \rangle + \langle \rho'_e \langle \mathbf{v_e} \rangle^f \rangle + \langle \langle \rho_e \rangle^f \mathbf{v'_e} \rangle + \langle \rho'_e \mathbf{v'_e} \rangle \Big) \\ - \frac{1}{V} \int_{A_{sf}} \rho_e \mathbf{v_e} \mathbf{v_{esf}} \cdot \mathbf{n} dA. \end{aligned} \tag{3.2.55}$$

Changing superficial averaging to intrinsic averaging, and applying rules 3.2.13 and 3.2.14, Equation 3.2.55 is simplified to the following:

$$\begin{aligned} \langle \frac{\partial \rho_e \mathbf{v_e}}{\partial t'} \rangle = \frac{\partial}{\partial t} \Big(\varepsilon_f \langle \rho_e \rangle^f \langle \mathbf{v_e} \rangle^f \Big) + \frac{\partial}{\partial t} \Big(\varepsilon_f \langle \rho'_e \mathbf{v'_e} \rangle \Big) \\ - \frac{1}{V} \int_{A_{sf}} \rho_e \mathbf{v_e} \mathbf{v_{esf}} \cdot \mathbf{n} dA. \end{aligned} \tag{3.2.56}$$

Replacing the gradient operator in Slattery's theorem 3.2.8 with a divergence operator, applying the results to the second term in Equation 3.2.52, and using the no-slip condition, we obtain:

$$\langle \nabla' \cdot (\rho_e \mathbf{v_e} \mathbf{v_e}) \rangle = \nabla \cdot \langle (\rho_e \mathbf{v_e} \mathbf{v_e}) \rangle. \tag{3.2.57}$$

Expressing the velocities and density in terms of intrinsic averages, Equation 3.2.57 becomes:

$$\begin{aligned} \langle \nabla' \cdot (\rho_e \mathbf{v_e} \mathbf{v_e}) \rangle &= \nabla \cdot \langle (\rho_e \mathbf{v_e} \mathbf{v_e}) \rangle, \\ &= \nabla \cdot \langle \Big(\big(\langle \rho_e \rangle^f + \rho'_e \big) \big(\langle \mathbf{v_e} \rangle^f + \mathbf{v'_e} \big) \big(\langle \mathbf{v_e} \rangle^f + \mathbf{v'_e} \big) \Big) \rangle. \end{aligned} \tag{3.2.58}$$

Expanding the right hand side of Equation 3.2.58, we have:

$$\begin{aligned}\langle\nabla'\cdot(\rho_e\mathbf{v_e}\mathbf{v_e})\rangle &= \nabla\cdot\langle\Big(\big(\langle\rho_e\rangle^f+\rho'_e\big)\big(\langle\mathbf{v_e}\rangle^f+\mathbf{v'_e}\big)\big(\langle\mathbf{v_e}\rangle^f+\mathbf{v'_e}\big)\Big)\rangle,\\ &= \nabla\cdot\langle\Big(\big(\langle\rho_e\rangle^f+\rho'_e\big)\big(\langle\mathbf{v_e}\rangle^f\langle\mathbf{v_e}\rangle^f+\mathbf{v'_e}\langle\mathbf{v_e}\rangle^f+\langle\mathbf{v_e}\rangle^f\mathbf{v'_e}+\mathbf{v'_e}\mathbf{v'_e}\big)\Big)\rangle,\\ &= \nabla\cdot\langle\Big(\big(\langle\rho_e\rangle^f\langle\mathbf{v_e}\rangle^f\langle\mathbf{v_e}\rangle^f+\langle\rho_e\rangle^f\mathbf{v'_e}\langle\mathbf{v_e}\rangle^f+\langle\rho_e\rangle^f\langle\mathbf{v_e}\rangle^f\mathbf{v'_e}\\ &+\langle\rho_e\rangle^f\mathbf{v'_e}\mathbf{v'_e}+\rho'_e\langle\mathbf{v_e}\rangle^f\langle\mathbf{v_e}\rangle^f+\rho'_e\mathbf{v'_e}\langle\mathbf{v_e}\rangle^f\\ &+\rho'_e\langle\mathbf{v_e}\rangle^f\mathbf{v'_e}+\rho'_e\mathbf{v'_e}\mathbf{v'_e}\Big)\rangle. \end{aligned}\tag{3.2.59}$$

Changing superficial average to intrinsic average, and applying rules 3.2.11, 3.2.13 and 3.2.14 to Equation 3.2.59, we obtain:

$$\begin{aligned}\langle\nabla'\cdot(\rho_e\mathbf{v_e}\mathbf{v_e})\rangle &= \nabla\cdot\varepsilon_f\Big(\langle\rho_e\rangle^f\langle\mathbf{v_e}\rangle^f\langle\mathbf{v_e}\rangle^f+\langle\rho_e\rangle^f\langle\mathbf{v'_e}\mathbf{v'_e}\rangle^f+\langle\rho'_e\mathbf{v'_e}\rangle^f\langle\mathbf{v_e}\rangle^f\\ &+\langle\rho'_e\mathbf{v'_e}\rangle^f\langle\mathbf{v_e}\rangle^f+\langle\rho'_e\mathbf{v'_e}\mathbf{v'_e}\rangle^f\Big)\\ &= \nabla\cdot\varepsilon_f\Big(\langle\rho_e\rangle^f\langle\mathbf{v_e}\rangle^f\langle\mathbf{v_e}\rangle^f\Big)+\nabla\cdot\varepsilon_f\Big(\langle\rho_e\rangle^f\langle\mathbf{v'_e}\mathbf{v'_e}\rangle^f\Big)\\ &+\nabla\cdot\varepsilon_f\Big(\langle\rho'_e\mathbf{v'_e}\rangle^f\langle\mathbf{v_e}\rangle^f\Big)+\nabla\cdot\varepsilon_f\Big(\langle\rho'_e\mathbf{v'_e}\rangle^f\langle\mathbf{v_e}\rangle^f\Big)\\ &+\nabla\cdot\varepsilon_f\Big(\langle\rho'_e\mathbf{v'_e}\mathbf{v'_e}\rangle^f\Big)\end{aligned}\tag{3.2.60}$$

Applying rule 3.2.10 to the averaged pressure term in Equation 3.2.52

$$\langle\nabla' p_e\rangle = \varepsilon_f\nabla\langle p_e\rangle^f+\frac{1}{V}\int_{A_{sf}}p'_e\mathbf{n}dA,\tag{3.2.61}$$

where p'_e is the pressure deviation from the mean.

Replacing the gradient operator in Slattery's theorem 3.2.8 with a divergence operator, and applying the results to the second term at the right hand side of Equation 3.2.52, we obtain:

$$\langle\nabla'\cdot(\mu_e\nabla'\mathbf{v_e})\rangle = \nabla\cdot\langle(\mu_e\nabla'\mathbf{v_e})\rangle+\frac{1}{V}\int_{A_{sf}}(\mu_e\nabla'\mathbf{v_e})\cdot\mathbf{n}dA\tag{3.2.62}$$

Changing superficial average to intrinsic average, applying rule 3.2.8 to the first term at the right hand side of Equation 3.2.62, and taking μ_e as a constant, we obtain:

$$\nabla \cdot \langle (\mu_e \nabla' \mathbf{v_e}) \rangle = \nabla \cdot \left(\varepsilon_f \langle \mu_e \rangle^f \nabla \langle \mathbf{v_e} \rangle^f + \frac{1}{V} \int_{A_{sf}} \mathbf{v_e} \mathbf{n} dA \right)$$
$$= \nabla \cdot \left(\varepsilon_f \langle \mu_e \rangle^f \nabla \langle \mathbf{v_e} \rangle^f \right) + \frac{1}{V} \nabla \cdot \int_{A_{sf}} \mathbf{v_e} \mathbf{n} dA. \tag{3.2.63}$$

Thus replacing the first term at the right hand side of Equation 3.2.62 with the right hand side of Equation 3.2.63, we obtain:

$$\langle \nabla' \cdot (\mu_e \nabla' \mathbf{v_e}) \rangle = \nabla \cdot \left(\varepsilon_f \langle \mu_e \rangle^f \nabla \langle \mathbf{v_e} \rangle^f \right) + \frac{1}{V} \nabla \cdot \int_{A_{sf}} \mathbf{v_e} \mathbf{n} dA$$
$$+ \frac{1}{V} \int_{A_{sf}} (\mu_e \nabla' \mathbf{v_e}) \cdot \mathbf{n} dA. \tag{3.2.64}$$

Assembling all the expanded averaged terms of Equation 3.2.52, which are given by Equations 3.2.56, 3.2.60, 3.2.61 and 3.2.64, the macroscopic momentum transport equation is given by:

$$\frac{\partial}{\partial t} \left(\varepsilon_f \langle \rho_e \rangle^f \langle \mathbf{v_e} \rangle^f \right) + \frac{\partial}{\partial t} \left(\varepsilon_f \langle \rho'_e \mathbf{v}'_\mathbf{e} \rangle^f \right) + \nabla \cdot \varepsilon_f \left(\langle \rho_e \rangle^f \langle \mathbf{v_e} \rangle^f \langle \mathbf{v_e} \rangle^f \right) + \nabla \cdot \varepsilon_f \left(\langle \rho_e \rangle^f \langle \mathbf{v}'_\mathbf{e} \mathbf{v}'_\mathbf{e} \rangle^f \right)$$
$$+ \nabla \cdot \varepsilon_f \left(\langle \rho'_e \mathbf{v}'_\mathbf{e} \rangle^f \langle \mathbf{v_e} \rangle^f \right) + \nabla \cdot \varepsilon_f \left(\langle \rho'_e \mathbf{v}'_\mathbf{e} \rangle^f \langle \mathbf{v_e} \rangle^f \right) + \nabla \cdot \varepsilon_f \left(\langle \rho'_e \mathbf{v}'_\mathbf{e} \mathbf{v}'_\mathbf{e} \rangle^f \right)$$
$$= -\varepsilon_f \nabla \langle p_e \rangle^f + \nabla \cdot \left(\varepsilon_f \langle \mu_e \rangle^f \nabla \langle \mathbf{v_e} \rangle^f \right) + \varepsilon_f \langle \rho_e \rangle^f \mathbf{g} + \frac{1}{V} \nabla \cdot \int_{A_{sf}} \mathbf{v_e} \mathbf{n} dA$$
$$+ \frac{1}{V} \int_{A_{sf}} (\mu_e \nabla' \mathbf{v_e}) \cdot \mathbf{n} dA - \frac{1}{V} \int_{A_{sf}} p'_e \mathbf{n} dA + \frac{1}{V} \int_{A_{sf}} \rho_e \mathbf{v_e} \mathbf{v_{esf}} \cdot \mathbf{n} dA. \tag{3.2.65}$$

The last integral term in Equation 3.2.65 quantifies the interfacial momentum flux in the case of a multi-phase flow. Since a single phase flow is assumed in our study, we consider the effect of that integral term negligible. Thus Equation 3.2.65 reduces to:

$$\frac{\partial}{\partial t} \left(\varepsilon_f \langle \rho_e \rangle^f \langle \mathbf{v_e} \rangle^f \right) + \frac{\partial}{\partial t} \left(\varepsilon_f \langle \rho'_e \mathbf{v}'_\mathbf{e} \rangle^f \right) + \nabla \cdot \varepsilon_f \left(\langle \rho_e \rangle^f \langle \mathbf{v_e} \rangle^f \langle \mathbf{v_e} \rangle^f \right) + \nabla \cdot \varepsilon_f \left(\langle \rho_e \rangle^f \langle \mathbf{v}'_\mathbf{e} \mathbf{v}'_\mathbf{e} \rangle^f \right)$$
$$+ \nabla \cdot \varepsilon_f \left(\langle \rho'_e \mathbf{v}'_\mathbf{e} \rangle^f \langle \mathbf{v_e} \rangle^f \right) + \nabla \cdot \varepsilon_f \left(\langle \rho'_e \mathbf{v}'_\mathbf{e} \rangle^f \langle \mathbf{v_e} \rangle^f \right) + \nabla \cdot \varepsilon_f \left(\langle \rho'_e \mathbf{v}'_\mathbf{e} \mathbf{v}'_\mathbf{e} \rangle^f \right)$$
$$= -\varepsilon_f \nabla \langle p_e \rangle^f + \nabla \cdot \left(\varepsilon_f \langle \mu_e \rangle^f \nabla \langle \mathbf{v_e} \rangle^f \right) + \varepsilon_f \langle \rho_e \rangle^f \mathbf{g} + \frac{1}{V} \nabla \cdot \int_{A_{sf}} \mathbf{v_e} \mathbf{n} dA$$
$$+ \frac{1}{V} \int_{A_{sf}} (\mu_e \nabla' \mathbf{v_e}) \cdot \mathbf{n} dA - \frac{1}{V} \int_{A_{sf}} p'_e \mathbf{n} dA. \tag{3.2.66}$$

The first term at the left hand side of Equation 3.2.66 describes the unsteady macroscopic momentum transport in the considered domain and the second term at the left hand accounts for unsteady momentum dispersion due to the presence of the solid in the flow domain. The third term accounts for macroscopic momentum convection across the domain boundaries, and the rest of the terms at the left hand side of Equation 3.2.66 are dispersion terms which occurred as a result of the presence of solid surfaces in the flow domain. The first three terms at the right hand side of Equation 3.2.66, respectively, are the macroscopic, pressure term, diffusive momentum transport term and body force per unit volume. In the case of a homogeneous fluid, the macroscopic momentum equation further reduces to:

$$\begin{aligned}
&\frac{\partial}{\partial t}\Big(\varepsilon_f\langle\rho_e\rangle^f\langle\mathbf{v_e}\rangle^f\Big) + \nabla\cdot\varepsilon_f\Big(\langle\rho_e\rangle^f\langle\mathbf{v_e}\rangle^f\langle\mathbf{v_e}\rangle^f\Big)\\
&= -\varepsilon_f\nabla\langle p_e\rangle^f + \nabla\cdot\Big(\varepsilon_f\langle\mu_e\rangle^f\nabla\langle\mathbf{v_e}\rangle^f\Big) + \varepsilon_f\langle\rho_e\rangle^f\mathbf{g} + \frac{1}{V}\nabla\cdot\int_{A_{sf}}\mathbf{v_e}\mathbf{n}dA\\
&-\nabla\cdot\varepsilon_f\Big(\langle\rho_e\rangle^f\langle\mathbf{v_e'}\mathbf{v_e'}\rangle^f\Big) + \frac{1}{V}\int_{A_{sf}}(\mu_e\nabla'\mathbf{v_e})\cdot\mathbf{n}dA - \frac{1}{V}\int_{A_{sf}}p_e'\mathbf{n}dA. \qquad (3.2.67)
\end{aligned}$$

The fifth term at the right hand side of Equation 3.2.67 is a dispersive momentum flux, we consider this term negligible for simplicity. However, since there are still integral terms in the macroscopic momentum Equation 3.2.67, the equation is not closed for numerical or analytical considerations. Let;

$$\mathbf{S_{pD}} = \frac{1}{V}\nabla\cdot\int_{A_{sf}}\mathbf{v_e}\mathbf{n}dA + \frac{1}{V}\int_{A_{sf}}(\mu_e\nabla'\mathbf{v_e})\cdot\mathbf{n}dA - \frac{1}{V}\int_{A_{sf}}p_e'\mathbf{n}dA,$$

where $\mathbf{S_{pD}}$ quantifies the pressure drop due to the presence of the solid surfaces in the flow domain. Thus replacing the integral in Equation 3.2.67 with $\mathbf{S_{pD}}$, we obtain:

$$\begin{aligned}
&\frac{\partial}{\partial t}\Big(\varepsilon_f\langle\rho_e\rangle^f\langle\mathbf{v_e}\rangle^f\Big) + \nabla\cdot\varepsilon_f\Big(\langle\rho_e\rangle^f\langle\mathbf{v_e}\rangle^f\langle\mathbf{v_e}\rangle^f\Big)\\
&= -\varepsilon_f\nabla\langle p_e\rangle^f + \nabla\cdot\Big(\varepsilon_f\langle\mu_e\rangle^f\nabla\langle\mathbf{v_e}\rangle^f\Big) + \varepsilon_f\langle\rho_e\rangle^f\mathbf{g} + \mathbf{S_{pD}}. \qquad (3.2.68)
\end{aligned}$$

Furthermore, closure of the Equation 3.2.68 requires pore-scale modelling since the microscopic velocity and its gradient appear in the integral terms, however, we use Darcy law for the closure in our discussion. Thus by the Darcy law, the pressure drop is given by:

$$\mathbf{S_pD} = -\frac{\langle\mu_e\rangle^f}{\langle K_p\rangle}\langle\mathbf{v_e}\rangle^f \qquad (3.2.69)$$

where $\langle K_p \rangle$ is the permeability of the porous medium.

Therefore, the closed macroscopic momentum equation for the mine effluent water is given by:

$$\begin{aligned}&\frac{\partial}{\partial t}\Big(\varepsilon_f \langle \rho_e \rangle^f \langle \mathbf{v_e} \rangle^f\Big) + \nabla \cdot \varepsilon_f \Big(\langle \rho_e \rangle^f \langle \mathbf{v_e} \rangle^f \langle \mathbf{v_e} \rangle^f\Big) \\ &= -\varepsilon_f \nabla \langle p_e \rangle^f + \nabla \cdot \Big(\varepsilon_f \langle \mu_e \rangle^f \nabla \langle \mathbf{v_e} \rangle^f\Big) + \varepsilon_f \langle \rho_e \rangle^f \mathbf{g} - K_h \langle \mathbf{v_e} \rangle^f,\end{aligned} \tag{3.2.70}$$

where $K_h = \frac{\langle \mu_e \rangle^f}{\langle K_p \rangle}$ is the hydraulic conductivity.

3.2.14 Macroscopic energy transport equation

Applying the volume averaging theorem given by Equation 3.2.8 to the microscopic energy transport Equation 3.1.41, we obtain:

$$\langle \frac{\partial \rho_e (C_p)_e T_e}{\partial t'} + \nabla' \cdot (\rho_e (C_p)_e T_e \mathbf{v_e}) \rangle = \langle \nabla' \cdot \kappa_e \nabla' T_e \rangle. \tag{3.2.71}$$

Applying rule 3.2.11 to Equation 3.2.71, we obtain:

$$\langle \frac{\partial \rho_e (C_p)_e T_e}{\partial t'} \rangle + \langle \nabla' \cdot (\rho_e (C_p)_e T_e \mathbf{v_e}) \rangle = \langle \nabla' \cdot \kappa_e \nabla' T_e \rangle + \langle S_{TT} \rangle. \tag{3.2.72}$$

The averaged time derivative in Equation 3.2.72 is expanded by applying Equation 3.2.9, thus we obtain:

$$\langle \frac{\partial \rho_e (C_p)_e T_e}{\partial t'} \rangle = \frac{\partial}{\partial t} \langle \rho_e (C_p)_e T_e \rangle - \frac{1}{V} \int_{A_{sf}} \rho_e (C_p)_e T_e \mathbf{v_{esf}} \cdot \mathbf{n} dA. \tag{3.2.73}$$

We want to obtain the derivatives of averaged quantities but the average of derivatives, thus we write the microscopic temperature and density as sums of intrinsic averages and deviations. Thus substituting; $T_e = \langle T_e \rangle^f + T_e'$, and $\rho_e = \langle \rho_e \rangle^f + \rho_e'$ into the first term on the right hand side of Equation 3.2.73, we obtain:

$$\langle\frac{\partial\rho_e(C_p)_eT_e}{\partial t'}\rangle = \frac{\partial}{\partial t}\langle\Big((C_p)_e\big(\langle\rho_e\rangle^f+\rho_e'\big)\big(\langle T_e\rangle^f+T_e'\big)\Big)\rangle - \frac{1}{V}\int_{A_{sf}}\rho_e(C_p)_eT_e\mathbf{v_{esf}}\cdot\mathbf{n}dA. \tag{3.2.74}$$

Expanding the first term at the right hand side Equation 3.2.74, we obtain:

$$\langle\frac{\partial\rho_e(C_p)_eT_e}{\partial t'}\rangle = \frac{\partial}{\partial t}\langle\Big((C_p)_e\langle\rho_e\rangle^f\langle T_e\rangle^f+(C_p)_e\rho_e'\langle T_e\rangle^f + (C_p)_e\langle\rho_e\rangle^fT_e'+(C_p)_eT_e'\rho_e'\Big)\rangle - \frac{1}{V}\int_{A_{sf}}\rho_e(C_p)_eT_e\mathbf{v_{esf}}\cdot\mathbf{n}dA. \tag{3.2.75}$$

Changing superficial average to intrinsic average, and applying rules 3.2.11, 3.2.13 and 3.2.14 to Equation 3.2.75, we obtain:

$$\begin{aligned}\langle\frac{\partial\rho_e(C_p)_eT_e}{\partial t'}\rangle &= \frac{\partial}{\partial t}\varepsilon_f\Big(\langle(C_p)_e\rangle^f\langle\rho_e\rangle^f\langle T_e\rangle^f+\langle(C_p)_e\rangle^f\langle\,T_e'\rho_e'\rangle^f\Big)\\ &\quad-\frac{1}{V}\int_{A_{sf}}\rho_e(C_p)_eT_e\mathbf{v_{esf}}\cdot\mathbf{n}dA,\\ &= \frac{\partial}{\partial t}\varepsilon_f\Big(\langle(C_p)_e\rangle^f\langle\rho_e\rangle^f\langle T_e\rangle^f\Big)+\frac{\partial}{\partial t}\varepsilon_f\Big(\langle(C_p)_e\rangle^f\langle\,T_e'\rho_e'\rangle^f\Big)\\ &\quad-\frac{1}{V}\int_{A_{sf}}\rho_e(C_p)_eT_e\mathbf{v_{esf}}\cdot\mathbf{n}dA.\end{aligned} \tag{3.2.76}$$

Similarly for the average energy convection term in Equation 3.2.72, we replace the gradient operator in Slattery's theorem (3.2.8) with a divergence operator, and apply a no-slip condition to the results, thus we obtain:

$$\langle\nabla'\cdot(\rho_e(C_p)_eT_e\mathbf{v_e})\rangle = \nabla\cdot\langle(\rho_e(C_p)_eT_e\mathbf{v_e})\rangle. \tag{3.2.77}$$

Expressing microscopic variables at the right hand side of Equation 3.2.77 in terms of

deviations and mean, we have:

$$\begin{aligned}\langle\nabla'\cdot(\rho_e(C_p)_eT_e\mathbf{v_e})\rangle &= \nabla\cdot\langle\Big(\big(\langle\rho_e\rangle^f+\rho_e'\big)\langle(C_p)_e\rangle^f\big(\langle T_e\rangle^f+T_e'\big)\big(\langle\mathbf{v_e}\rangle^f+\mathbf{v_e'}\big)\Big)\rangle,\\ &= \nabla\cdot\langle\Big(\big(\langle\rho_e\rangle^f+\rho_e'\big)\langle(C_p)_e\rangle^f\big(\langle T_e\rangle^f\langle\mathbf{v_e}\rangle^f+T_e'\langle\mathbf{v_e}\rangle^f+\langle T_e\rangle^f\mathbf{v_e'}+T_e'\mathbf{v_e'}\big)\Big)\rangle,\\ &= \nabla\cdot\langle\Big(\langle\rho_e\rangle^f\langle(C_p)_e\rangle^f\langle T_e\rangle^f\langle\mathbf{v_e}\rangle^f+\langle\rho_e\rangle^f\langle(C_p)_e\rangle^fT_e'\langle\mathbf{v_e}\rangle^f\\ &+\langle\rho_e\rangle^f\langle(C_p)_e\rangle^f\langle T_e\rangle^f\mathbf{v_e'}+\langle\rho_e\rangle^f\langle(C_p)_e\rangle^fT_e'\mathbf{v_e'}\big)+\rho_e'\langle(C_p)_e\rangle^f\langle T_e\rangle^f\langle\mathbf{v_e}\rangle^f\\ &+\rho_e'\langle(C_p)_e\rangle^fT_e'\langle\mathbf{v_e}\rangle^f+\rho_e'\langle(C_p)_e\rangle^f\langle T_e\rangle^f\mathbf{v_e'}\\ &+\rho_e'\langle(C_p)_e\rangle^fT_e'\mathbf{v_e'}\Big)\rangle. \end{aligned}\tag{3.2.78}$$

Changing superficial average to intrinsic average, and applying rules 3.2.11, 3.2.13 and 3.2.14 to Equation 3.2.78, we obtain:

$$\begin{aligned}\langle\nabla'\cdot(\rho_e(C_p)_eT_e\mathbf{v_e})\rangle &= \nabla\cdot\varepsilon_f\Big(\langle\rho_e\rangle^f\langle(C_p)_e\rangle^f\langle T_e\rangle^f\langle\mathbf{v_e}\rangle^f\Big)+\nabla\cdot\varepsilon_f\Big(\langle\rho_e\rangle^f\langle(C_p)_e\rangle^f\langle T_e'\mathbf{v_e'}\rangle^f\Big)\\ &+\nabla\cdot\varepsilon_f\Big(\langle\rho_e'T_e'\rangle^f\langle(C_p)_e\rangle^f\langle\mathbf{v_e}\rangle^f\Big)+\nabla\cdot\varepsilon_f\Big(\langle(C_p)_e\rangle^f\langle T_e\rangle^f\langle\rho_e'\mathbf{v_e'}\rangle^f\Big)\\ &+\nabla\cdot\varepsilon_f\Big(\langle(C_p)_e\rangle^f\langle\rho_e'T_e'\mathbf{v_e'}\rangle^f\Big).\end{aligned}\tag{3.2.79}$$

Replacing the gradient operator in Slattery's theorem 3.2.8 with a divergence operator, and applying the results to the second term at the right hand side of Equation 3.2.72, we obtain:

$$\langle\nabla'\cdot\kappa_e\nabla'T_e\rangle=\nabla\cdot\langle(\kappa_e\nabla'T_e)\rangle+\frac{1}{V}\int_{A_{sf}}(\kappa_e\nabla'T_e)\cdot\mathbf{n}dA\tag{3.2.80}$$

Changing superficial average to intrinsic average, applying rule 3.2.8 to the first term at the right hand side of Equation 3.2.80, and taking κ_e as constant, we obtain:

$$\begin{aligned}\nabla\cdot\langle(\kappa_e\nabla'T_e)\rangle &= \nabla\cdot\Big(\varepsilon_f\langle\kappa_e\rangle^f\nabla\langle T_e\rangle^f+\frac{1}{V}\int_{A_{sf}}T_e\mathbf{n}dA\Big)\\ &= \nabla\cdot\Big(\varepsilon_f\langle\kappa_e\rangle^f\nabla\langle T_e\rangle^f\Big)+\frac{1}{V}\nabla\cdot\int_{A_{sf}}T_e\mathbf{n}dA.\end{aligned}\tag{3.2.81}$$

Thus replacing the first term at the right hand side of Equation 3.2.80 with the right hand side of Equation 3.2.81, we obtain:

$$\langle \nabla' \cdot \kappa_e \nabla' T_e \rangle = \nabla \cdot \left(\varepsilon_f \langle \kappa_e \rangle^f \nabla \langle T_e \rangle^f \right) + \frac{1}{V} \nabla \cdot \int_{A_{sf}} T_e \mathbf{n} dA + \frac{1}{V} \int_{A_{sf}} (\kappa_e \nabla' T_e) \cdot \mathbf{n} dA. \tag{3.2.82}$$

Assembling all the expanded averaged terms of Equation 3.2.72, which are given by Equations 3.1.33, 3.1.35, and 3.1.38, the macroscopic energy equation is given by:

$$\begin{aligned} &\frac{\partial}{\partial t} \varepsilon_f \left(\langle (C_p)_e \rangle^f \langle \rho_e \rangle^f \langle T_e \rangle^f \right) + \frac{\partial}{\partial t} \varepsilon_f \left(\langle (C_p)_e \rangle^f \langle \, T'_e \rho'_e \rangle^f \right) \\ &+ \nabla \cdot \varepsilon_f \left(\langle \rho_e \rangle^f \langle (C_p)_e \rangle^f \langle T_e \rangle^f \langle \mathbf{v_e} \rangle^f \right) + \nabla \cdot \varepsilon_f \left(\langle \rho_e \rangle^f \langle (C_p)_e \rangle^f \langle T'_e \mathbf{v'_e} \rangle^f \right) \\ &+ \nabla \cdot \varepsilon_f \left(\langle \rho'_e T'_e \rangle^f \langle (C_p)_e \rangle^f \langle \mathbf{v_e} \rangle^f \right) + \nabla \cdot \varepsilon_f \left(\langle (C_p)_e \rangle^f \langle T_e \rangle^f \langle \rho'_e \mathbf{v'_e} \rangle^f \right) \\ &+ \nabla \cdot \varepsilon_f \left(\langle (C_p)_e \rangle^f \langle \rho'_e T'_e \mathbf{v'_e} \rangle^f \right) = \nabla \cdot \left(\varepsilon_f \langle \kappa_e \rangle^f \nabla \langle T_e \rangle^f \right) + \frac{1}{V} \nabla \cdot \int_{A_{sf}} T_e \mathbf{n} dA \\ &+ \frac{1}{V} \int_{A_{sf}} (\kappa_e \nabla' T_e) \cdot \mathbf{n} dA + \frac{1}{V} \int_{A_{sf}} \rho_e (C_p)_e T_e \mathbf{v_{esf}} \cdot \mathbf{n} dA + \langle S_{TT} \rangle. \end{aligned} \tag{3.2.83}$$

The first term on the left hand side of Equation 3.2.83 describes the unsteady macroscopic energy transport in the considered domain and the second term at the left hand accounts for unsteady energy dispersion due to the presence of the solid in the flow domain. The third term accounts for macroscopic energy convection across the domain boundaries, and the rest of the terms on the left hand side of Equation 3.2.83 are dispersion terms which occurred as a result of the presence of solid surfaces in the flow domain. In the case of a homogeneous fluid, the macroscopic energy equation reduces to the following:

$$\begin{aligned} &\frac{\partial}{\partial t} \varepsilon_f \left(\langle (C_p)_e \rangle^f \langle \rho_e \rangle^f \langle T_e \rangle^f \right) + \nabla \cdot \varepsilon_f \left(\langle \rho_e \rangle^f \langle (C_p)_e \rangle^f \langle T_e \rangle^f \langle \mathbf{v_e} \rangle^f \right) \\ &= \nabla \cdot \left(\varepsilon_f \langle \kappa_e \rangle^f \nabla \langle T_e \rangle^f \right) - \nabla \cdot \varepsilon_f \left(\langle \rho_e \rangle^f \langle (C_p)_e \rangle^f \langle T'_e \mathbf{v'_e} \rangle^f \right) + \frac{1}{V} \nabla \cdot \int_{A_{sf}} T_e \mathbf{n} dA \\ &+ \frac{1}{V} \int_{A_{sf}} (\kappa_e \nabla' T_e) \cdot \mathbf{n} dA + \frac{1}{V} \int_{A_{sf}} \rho_e (C_p)_e T_e \mathbf{v_{esf}} \cdot \mathbf{n} dA + \langle S_{TT} \rangle. \end{aligned} \tag{3.2.84}$$

The effect of the dispersion term on the right hand side of Equation 3.2.84 is assumed negligible for the sake of simplicity. However, due to the presence of the integral terms in Equation 3.2.84, the equation is not closed for numerical or analytical treatment, therefore, closure is required. The integrals in the equation are due to the presence of the solid phase in the flow domain. Let

$$S_{FT} = \frac{1}{V}\nabla \cdot \int_{A_{sf}} T_e \mathbf{n} dA + \frac{1}{V}\int_{A_{sf}} (\kappa_e \nabla' T_e) \cdot \mathbf{n} dA + \frac{1}{V}\int_{A_{sf}} \rho_e (C_p)_e T_e \mathbf{v_{esf}} \cdot \mathbf{n} dA.$$

Then the macroscopic energy Equation (3.2.84) can be written as:

$$\begin{aligned} &\frac{\partial}{\partial t}\varepsilon_f \Big(\langle (\langle (C_p)_e \rangle^f \langle \rho_e \rangle^f \langle T_e \rangle^f \Big) + \nabla \cdot \varepsilon_f \Big(\langle \rho_e \rangle^f \langle (\langle (C_p)_e \rangle^f \langle T_e \rangle^f \langle \mathbf{v_e} \rangle^f \Big) \\ &= \nabla \cdot \Big(\varepsilon_f \langle \kappa_e \rangle^f \nabla \langle T_e \rangle^f \Big) + S_{FT} + \langle S_{TT} \rangle. \end{aligned} \tag{3.2.85}$$

The macroscopic energy transport equation for the solid phase is obtained by averaging Equation 3.1.42 over the REV, thus by applying the volume averaging theorem given by Equation 3.2.8 to Equation 3.1.42, we have:

$$\langle \frac{\partial \rho_s (C_p)_s T_s}{\partial t'} \rangle = \langle \nabla' \cdot \kappa_s \nabla' T_s \rangle. \tag{3.2.86}$$

By the same procedure used to obtain Equation 3.2.76, the expanded averaged unsteady term in Equation 3.2.86 is obtained as:

$$\begin{aligned} \langle \frac{\partial \rho_s (C_p)_s T_s}{\partial t'} \rangle = &\frac{\partial}{\partial t}(1-\varepsilon_f)\Big(\langle (C_p)_s \rangle^s \langle \rho_s \rangle^s \langle T_s \rangle^s \Big) + \frac{\partial}{\partial t}(1-\varepsilon_f)\Big(\langle (C_p)_s \rangle^s \langle \, T_s' \rho_s' \rangle^s \Big) \\ &- \frac{1}{V}\int_{A_{sf}} \rho_s (C_p)_s T_s \mathbf{v_{esf}} \cdot \mathbf{n} dA. \end{aligned} \tag{3.2.87}$$

where $\langle T_s \rangle^s$ is the solid phase average of temperature, T_s' is the temperature deviation from the mean and $\varepsilon_s = 1 - \varepsilon_f$, is the solid fraction.

By the same procedure used to obtain Equation 3.2.82, the expanded averaged conduction term in Equation 3.2.86 is obtained as:

$$\begin{aligned} \langle \nabla' \cdot \kappa_s \nabla' T_s \rangle = &\nabla \cdot \Big((1-\varepsilon_f) \langle \kappa_s \rangle^s \nabla \langle T_s \rangle^s \Big) + \frac{1}{V}\nabla \cdot \int_{A_{sf}} T_s \mathbf{n} dA \\ &+ \frac{1}{V}\int_{A_{sf}} (\kappa_s \nabla' T_s) \cdot \mathbf{n} dA. \end{aligned} \tag{3.2.88}$$

Combining Equations 3.2.87 and 3.2.88, the macroscopic energy transport through the solid phase is given by:

$$\begin{aligned}
&\frac{\partial}{\partial t}(1-\varepsilon_f)\Big(\langle(C_p)_s\rangle^s\langle\rho_s\rangle^s\langle T_s\rangle^s\Big)+\frac{\partial}{\partial t}(1-\varepsilon_f)\Big(\langle(C_p)_s\rangle^s\langle\ T_s'\rho_s'\rangle^s\Big)\\
&=\nabla\cdot\Big((1-\varepsilon_f)\langle\kappa_s\rangle^s\nabla\langle T_s\rangle^s\Big)+\frac{1}{V}\nabla\cdot\int_{A_{sf}}T_s\mathbf{n}dA\\
&+\frac{1}{V}\int_{A_{sf}}(\kappa_s\nabla' T_s)\cdot\mathbf{n}dA+\frac{1}{V}\int_{A_{sf}}\rho_s(C_p)_sT_s\mathbf{v_{esf}}\cdot\mathbf{n}dA. \qquad (3.2.89)
\end{aligned}$$

The integrals and the dispersive unsteady term (second term on the left hand side of Equation 3.2.89) occur due to the presence of the fluid phase. Let

$$S_{ST}=\frac{1}{V}\nabla\cdot\int_{A_{sf}}T_s\mathbf{n}dA+\frac{1}{V}\int_{A_{sf}}(\kappa_s\nabla' T_s)\cdot\mathbf{n}dA+\frac{1}{V}\int_{A_{sf}}\rho_s(C_p)_sT_s\mathbf{v_{esf}}\cdot\mathbf{n}dA.$$

For a homogeneous solid, the dispersive unsteady term vanishes, thus we obtain:

$$\frac{\partial}{\partial t}(1-\varepsilon_f)\Big(\langle(C_p)_s\rangle^s\langle\rho_s\rangle^s\langle T_s\rangle^s\Big)=\nabla\cdot\Big((1-\varepsilon_f)\langle\kappa_s\rangle^s\nabla\langle T_s\rangle^s\Big)+S_{ST}. \qquad (3.2.90)$$

The complete macroscopic energy transport equation is the combined energy transport Equation 3.2.85 for the fluid phase, and Equation 3.2.90 for the solid phase. Thus we have:

$$\begin{aligned}
&\frac{\partial}{\partial t}(1-\varepsilon_f)\Big(\langle(C_p)_s\rangle^s\langle\rho_s\rangle^s\langle T_s\rangle^s\Big)+\frac{\partial}{\partial t}\varepsilon_f\Big(\langle(C_p)_e\rangle^f\langle\rho_e\rangle^f\langle T_e\rangle^f\Big)\\
&+\nabla\cdot\varepsilon_f\Big(\langle\rho_e\rangle^f\langle(C_p)_e\rangle^f\langle T_e\rangle^f\langle\mathbf{v_e}\rangle^f\Big)=\nabla\cdot\Big((1-\varepsilon_f)\langle\kappa_s\rangle^s\nabla\langle T_s\rangle^s\Big)\\
&+\nabla\cdot\Big(\varepsilon_f\langle\kappa_e\rangle^f\nabla\langle T_e\rangle^f\Big)+S_{ET}+\langle S_{TT}\rangle, \qquad (3.2.91)
\end{aligned}$$

where $S_{ET}=S_{FT}+S_{ST}$.

In a case where the fluid and the solid exist in thermodynamic equilibrium, their temperatures are the same, i. e. $\langle T_e\rangle^f=\langle T_s\rangle^f=T$, where T is a common temperature variable. In this case, the energy transport Equation 3.2.91 can be simplified to the following:

$$\frac{\partial}{\partial t}\rho_M T+\nabla\cdot\Big(\varepsilon_f\langle\rho_e\rangle^f\langle(C_p)_e\rangle^f\langle\mathbf{v_e}\rangle^f T\Big)=\nabla\cdot\kappa_M\nabla T+S_{ET}+\varepsilon_f\langle S_{TT}\rangle^f, \qquad (3.2.92)$$

where

$$\rho_M=\Big((1-\varepsilon_f)\langle(C_p)_s\rangle^s\langle\rho_s\rangle^s+\varepsilon_f\langle(C_p)_e\rangle^f\langle\rho_e\rangle^f\Big),$$

and

$$\kappa_M = \Big((1-\varepsilon_f)\langle\kappa_s\rangle^s + \varepsilon_f\langle\kappa_e\rangle^f\Big).$$

The oxidation of iron and the dissolution of calcite are exothermic processes. Thus, the heat released from these reactions is used for the closure of the energy Equation 3.2.85.

When the oxidation of iron occurs, the amount of heat released is 17800 J/mol [21]. Converting moles to mass, the energy released from the oxidation is 317.85 J/g. Energy is released is equal to the product change in concentration and the enthalpy of the oxidation. The rate of energy release is given by:

$$\langle S_{TT}\rangle^f = (\Delta C_3) \times 317.86, \tag{3.2.93}$$

where ΔC_3 is the change in concentration of ferric ion per unit time.

Similarly, when calcite dissolution occurs, the amount of heat released is 1206.92 J/mol [21]. Converting to mole to mass, we obtain 12.07 J/g. Thus, the energy released from calcite dissolution per unit time is given by:

$$S_T = (\Delta C_6) \times 12.07, \tag{3.2.94}$$

where ΔC_6 is the change in concentration of calcium ions per unit time. Substituting Equations 3.2.94 and 3.2.94 into Equation 3.2.92, the closed macroscopic energy equation is given by:

$$\begin{aligned}&\frac{\partial}{\partial t}\rho_M T + \nabla\cdot\Big(\varepsilon_f\langle\rho_e\rangle^f\langle(C_p)_e\rangle^f\langle\mathbf{v_e}\rangle^f T\Big)\\ &= \nabla\cdot\kappa_M\nabla T + 12.07(\Delta C_6) + 317.86\varepsilon_f(\Delta C_3).\end{aligned} \tag{3.2.95}$$

3.3 Complete mathematical model for AMD

Let $\mathbf{v} = \langle\mathbf{v_e}\rangle^f$, $\mu = \langle\mu_e\rangle^f$, $(C_p)_f = \langle(C_p)_e\rangle^f$, $p = \langle p_e\rangle^f$ and $\rho = \langle\rho_w\rangle^f$. The water produced during reactions inside the domain is considered negligible. The complete model for the flow and reactive transport processes inside the limestone is given by:

$$\nabla\cdot\mathbf{v} = 0. \tag{3.3.1}$$

$$\frac{\partial}{\partial t}\Big(\varepsilon_f \rho \mathbf{v}\Big) + \nabla \cdot \varepsilon_f \Big(\rho \mathbf{v}\mathbf{v}\Big) = -\varepsilon_f \nabla p + \nabla \cdot \Big(\varepsilon_f \mu \nabla \mathbf{v}\Big) + \varepsilon_f \rho \mathbf{g} - K_h \mathbf{v}. \tag{3.3.2}$$

$$\frac{\partial \varepsilon_f C_1}{\partial t} + \nabla \cdot \Big(\varepsilon_f \mathbf{v} C_1\Big) - \nabla \cdot \Big(\varepsilon_f \bar{\mathbf{D}} \cdot \nabla C_1\Big) = -K_f\big((1-\theta_c)\mathcal{B}(\theta_f)\big)\theta_L C_1 + 0.00040984 K_b C_6 C_8. \tag{3.3.3}$$

$$\frac{\partial \varepsilon_f C_2}{\partial t} + \nabla \cdot \Big(\varepsilon_f \mathbf{v_e} C_2\Big) - \nabla \cdot \Big(\varepsilon_f \bar{\mathbf{D}} \cdot \nabla C_2\Big) = K_o C_3 C_7. \tag{3.3.4}$$

$$\frac{\partial \varepsilon_f C_3}{\partial t} + \nabla \cdot \Big(\varepsilon_f \mathbf{v} C_3\Big) - \nabla \cdot \Big(\varepsilon_f \bar{\mathbf{D}} \cdot \nabla C_3\Big) = -K_o C_3 C_7. \tag{3.3.5}$$

$$\frac{\partial \varepsilon_f C_4}{\partial t} + \nabla \cdot \Big(\varepsilon_f \mathbf{v} C_4\Big) - \nabla \cdot \Big(\varepsilon_f \bar{\mathbf{D}} \cdot \nabla C_4\Big) = -\theta_c \theta_L K_{dep,f} \mathcal{B}(\theta_f) C_4. \tag{3.3.6}$$

$$\frac{\partial \varepsilon_f C_5}{\partial t} + \nabla \cdot \Big(\varepsilon_f \mathbf{v} C_5\Big) - \nabla \cdot \Big(\varepsilon_f \bar{\mathbf{D}} \cdot \nabla C_5\Big) = 0. \tag{3.3.7}$$

$$\frac{\partial \varepsilon_f C_6}{\partial t} + \nabla \cdot \Big(\varepsilon_f \mathbf{v} C_6\Big) - \nabla \cdot \Big(\varepsilon_f \bar{\mathbf{D}} \cdot \nabla C_6\Big) = 40 K_f\big((1-\theta_c)\mathcal{B}(\theta_f)\big)\theta_L C_1 - 0.0164 K_b C_6 C_8. \tag{3.3.8}$$

$$\frac{\partial \varepsilon_f C_7}{\partial t} + \nabla \cdot \Big(\varepsilon_f \mathbf{v} C_7\Big) - \nabla \cdot \Big(\varepsilon_f \bar{\mathbf{D}} \cdot \nabla C_7\Big) = -0.25 K_o C_3 C_7. \tag{3.3.9}$$

$$\frac{\partial \varepsilon_f C_8}{\partial t} + \nabla \cdot \Big(\varepsilon_f \mathbf{v} C_8\Big) - \nabla \cdot \Big(\varepsilon_f \bar{\mathbf{D}} \cdot \nabla C_8\Big)$$
$$= 61 K_f \big((1-\theta_c)\mathcal{B}(\theta_f)\big)\theta_L C_1 - 0.025 K_b C_6 C_8. \tag{3.3.10}$$

$$\frac{\partial}{\partial t}\rho_M T + \nabla \cdot \Big(\varepsilon_f \rho (C_p)_f \mathbf{v} T\Big)$$
$$= \nabla \cdot \kappa_M \nabla T + 12.07(\Delta C_6) + 317.86 \varepsilon_f (\Delta C_3). \tag{3.3.11}$$

We remark that the coupling of temperature and the chemical species is through the second and third term of Equation 3.3.11 and the parameter K_0. In general, the parameter K_0 is temperature-dependent but here we assume it to be constant for simplicity.

In addition to the Equations 3.3.1 – 3.3.11, one needs initial and boundary conditions. These are problem specific and they will be presented in Chapter 5 for specific cases.

3.4 Summary

In this Chapter, the continuum approaches for modelling fluid flows on and through materials are used to derive a system of partial differential equations. A complete model is obtained by closure of the partial differential equations with kinetic data that resulted from discussions on chemical kinetics of calcite dissolution, oxidation of ferrous ions and filtration.

Chapter 4

Numerical modelling

In this Chapter, we assume a uniform flow with a constant pressure gradient. The resulting model is a system of linear partial differential equations that are coupled in the source term. The finite volume method is used to obtain a discretized model to the continuous model.

The model obtained in Chapter 3 will be simulated in a two-dimensional rectangular coordinate system, in an $xy-$plane. The y-axis is the vertical axis and the x-axis is the horizontal axis of the domain. The domain denoted by Ω_d, is the area enclosed by a rectangle of finite size. Specifically, we consider a case in which the effluent water flows through a distance L_x units in the x direction and L_y units in the y direction. Figure 4.1 shows the domain used in our numerical study.

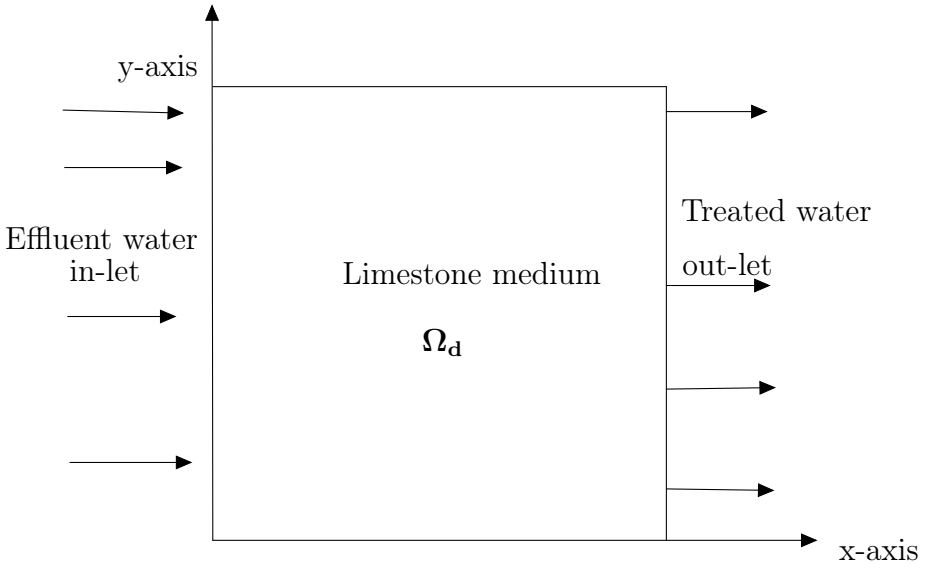

Figure 4.1: A 2-dimensional rectangular domain Ω_d.

The gradient operator in two-dimensional rectangular coordinates is given by:

$$\nabla = \frac{\partial}{\partial x}\mathbf{i} + \frac{\partial}{\partial y}\mathbf{j}, \tag{4.0.1}$$

and the velocity vector is expressed in component form by:

$$\mathbf{v} = u\mathbf{i} + v\mathbf{j}. \tag{4.0.2}$$

In general the governing equation for any transport phenomena can be written as:

$$\frac{\partial \rho_\phi \phi}{\partial t} + \nabla \cdot (\rho_\phi \mathbf{v}\phi) = \nabla \cdot (\Gamma_\phi \nabla \phi) + S_\phi, \qquad \in \Omega_d \tag{4.0.3}$$

where ϕ the dependent variable is a scalar quantity such as temperature or concentration and ρ_ϕ is the density of ϕ. The first term at the right hand side of Equation 4.0.3 describes the rate of change of the quantity ϕ due to a gradient in ϕ. The last term (left hand side of Equation 4.0.3) describes the rate of production or consumption of ϕ. The discretization, linear system and solution methods used for Equation 4.0.3 apply to each of the chemical and energy transport equations derived in Chapter 3. We first discuss the discretization procedure for a steady transport case, and conclude with a discretization procedure for the time-dependent Equation 4.0.3.

4.1 Discretization of a steady transport equation

For a steady transport case, the first term in Equation 4.0.3 vanishes, thus we have:

$$\nabla \cdot (\rho_\phi \mathbf{v}\phi) = \nabla \cdot (\Gamma_\phi \nabla \phi) + S_\phi. \qquad \in \Omega_d \tag{4.1.1}$$

By Equations 4.0.1 and 4.0.2, the two-dimensional form of Equation 4.1.1 is given by:

$$\Big(\frac{\partial}{\partial x}\mathbf{i} + \frac{\partial}{\partial y}\mathbf{j}\Big) \cdot \Big(\rho_\phi \phi (u\mathbf{i} + v\mathbf{j})\Big) = \Big(\frac{\partial}{\partial x}\mathbf{i} + \frac{\partial}{\partial y}\mathbf{j}\Big) \cdot \Big(\Gamma_\phi \Big(\frac{\partial}{\partial x}\mathbf{i} + \frac{\partial}{\partial y}\mathbf{j}\Big)\phi\Big) + S_\phi. \tag{4.1.2}$$

Expanding and simplifying Equation 4.1.2, we obtain:

$$\frac{\partial \rho_\phi u\phi}{\partial x} + \frac{\partial \rho_\phi v\phi}{\partial y} = \frac{\partial}{\partial x}\Gamma_\phi \frac{\partial \phi}{\partial x} + \frac{\partial}{\partial y}\Gamma_\phi \frac{\partial \phi}{\partial y} + S_\phi. \qquad \in \Omega_d \tag{4.1.3}$$

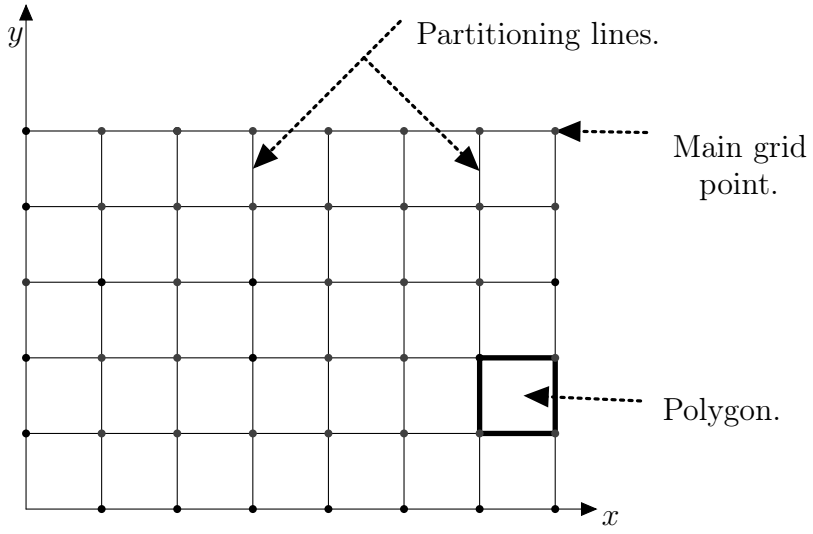

Figure 4.2: A partitioned rectangular domain Ω_d.

The set of points are located at the intersecting points of the partitioning lines, these points are called main grid points. The polygons (rectangles in the Figure 4.2) are the areas enclosed by a set of grid points connected by partitioning lines. The partitioned domain is called a grid or mesh.

Let N_x and N_y be the number of partitions in the x and y directions respectively. The ratio of length and number of partitions is called grid size or step size. The step size in the x direction is given by:

$$\Delta x = L_x / N_x, \tag{4.1.4}$$

and the step size in the y direction is given by:

$$\Delta y = L_y/N_y. \tag{4.1.5}$$

The numerical solution to the transport equations is stored on the grid points.

However, further details of the discrete domain are required to solve the linear system of equations which is obtained by discretizing the transport equation. These details include a description of the exact location of a grid point and its neighbours. Figure 4.3 shows a detailed description of the discretized domain. The broken lines in Figure 4.3 are the centrelines of the solid (unbroken) lines in Figure 4.2 and the black dots (•) are the main grid points (grid points in Figure 4.2).

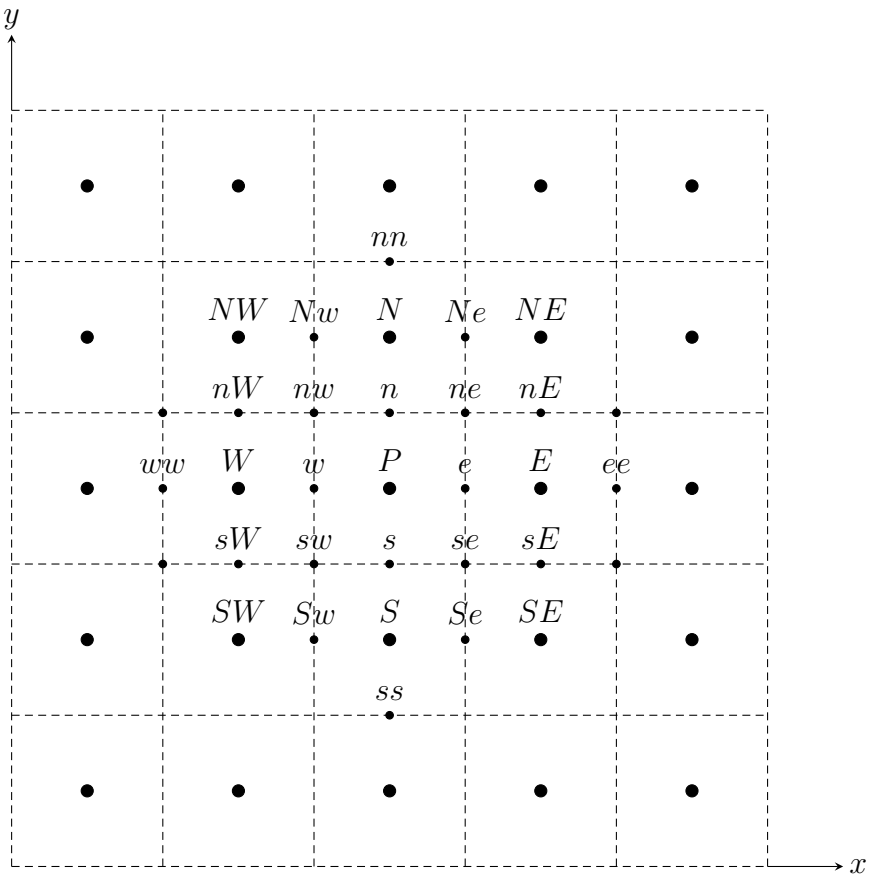

Figure 4.3: Practice B grid used in discretization [65, 28].

In Figure 4.3, the single upper-case letters indicate main grid points. At any grid point P, inside the partitioned domain, there are four (4) neighbouring points. These grid points

are denoted by $W, E, N,$ and S for western, eastern, northern and southern neighbouring grid points respectively.

The lower case $(n, nn, e, s, ss, ee, ww, w)$ and mixed case $(nE, sE, Ne, Se, \cdots, sW)$ letters located in-between the main grid points denote minor grid points formed by the broken lines. These minor grid points aid in describing locations in the domain.

From Figure 4.3, the rectangles surrounding the main grid points (e.g. P,), formed by connecting the neighbouring minor grid points with the broken lines is called a control volume. The size of the control volume (denoted by V_{CV}) is the measurable area of the rectangle enclosing the main grid point and bounded by the minor grid points. The length of each side of the control volume is called interface area. The interface area at the western side of the control volume is denoted by A_w, the eastern interface area is denoted by (A_e), the northern interface area is denoted by (A_n) and the southern interface area of the control volume is denoted by A_s. For a two dimensional rectangular domain, the interface areas are given by the Table 4.1.

Interface area	A_e	A_w	A_n	A_s	V_{CV}
Size	Δy	Δy	Δx	Δx	$\Delta x \Delta y$

Table 4.1: Control volume size and its interface area sizes for a dimensional problem.

The control volume is the most important component of the domain that is used in discretization of the governing equation. The detail description of the control volume parts can be found in Figure 4.4.

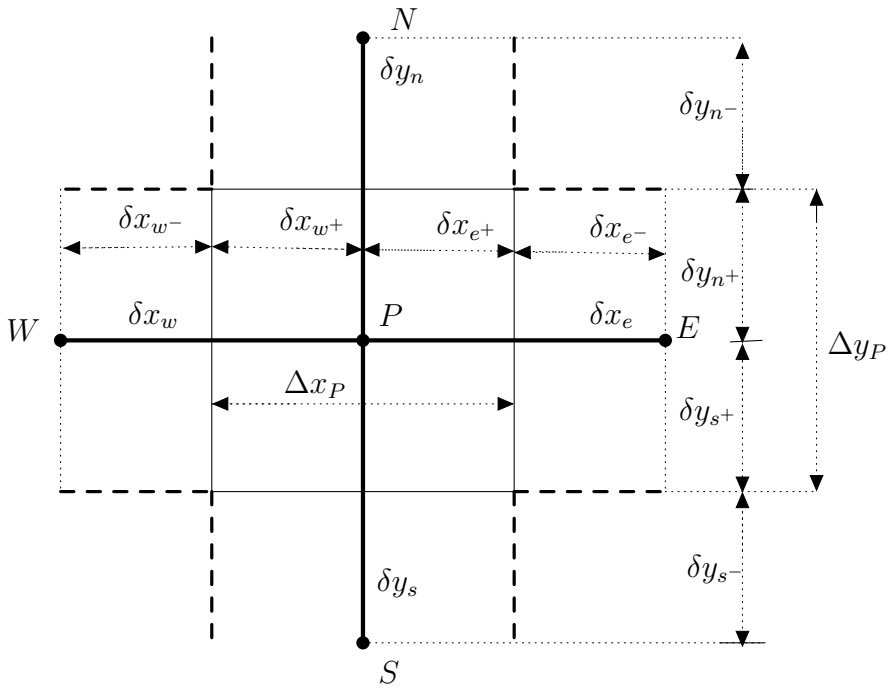

Figure 4.4: A control volume (CV) around a grid point P, with its linear dimensions.

In Figure 4.4, the distance between the western main grid point (W) and the central main grid point P, is denoted by δx_w, the distance between the eastern grid point E, and the central main grid point P, is denoted by δx_e, the distance between the southern main grid point S, and the central main grid point P, is denoted by δy_s, and the northern distance is denoted by δy_n.

Apart from the control volume interface areas, other useful lengths can also be identified with the control volume. The distance between the central grid point P, and the northern interface of the control volume is denoted by δy_{n^+}, the distance between the central grid point (P) and the southern interface of the control volume is denoted by δy_{s^+}, the eastern distance is denoted by δx_{e^+}, and the western distance is denoted by δx_{w^+}. These distances are generally referred to as linear dimensions. The distance from the control volume interface to neighbouring main grid points are also indicated in Figure 4.4.

The grid shown in Figure 4.3 is called Practice B by [65, 28] and will be used in our subsequent discussion. It is constructed such that the main grid points are located in the

center of the control volume. However, grid points are not always located at the center of the control volume, linear dimensions of the control volume are used in locating grid points or interpolating the unknown variable ϕ, at the grid points.

The distances (apart from the control volume interface areas) defined by Figure 4.4 are used to adequately locate the main grid points. Dimensionless ratios used for interpolation can also be defined using such distances or lengths. These dimensionless ratios are given by:

$$f_e = \frac{\delta x_{e^+}}{\delta x_e}, \; f_w = \frac{\delta x_{w^+}}{\delta x_w}, \; f_n = \frac{\delta y_{n^+}}{\delta y_n}, \text{ and } f_s = \frac{\delta y_{s^+}}{\delta y_s}. \tag{4.1.6}$$

For a uniform partition (implying a uniform grid), $\delta x_w = \delta x_e = \Delta x_P$, $\delta y_n = \delta y_s = \Delta y_P$, and all the dimensionless ratios are equal to half, i.e. $f_e = f_w = f_n = f_s = \frac{1}{2}$.

The discretization of the steady transport Equation 4.1.2 is obtained by integrating it over the control volume defined by Figure 4.4. That is:

$$\int_{CV} \frac{\partial \rho_\phi u\phi}{\partial x} dV_c + \int_{CV} \frac{\partial \rho_\phi v\phi}{\partial y} dV_c = \int_{CV} \frac{\partial}{\partial x} \Gamma_\phi \frac{\partial \phi}{\partial x} dV_c + \int_{CV} \frac{\partial}{\partial y} \Gamma_\phi \frac{\partial \phi}{\partial y} dV_c + \int_{CV} S_\phi dV_c, \tag{4.1.7}$$

where dV_c is an infinitesimal element of the control volume, defined by;

$$dV_c = Perpendicular\ Area\ \times\ length. \tag{4.1.8}$$

For the two-dimensional control volume given above in Figure 4.4, the size of the infinitesimal element is the area of an infinitesimal rectangular element. That is:

$$dV_c = dxdy, \tag{4.1.9}$$

where dx and dy are infinitesimal lengths in the x and y directions respectively. Thus by substitution, Equation 4.1.7 becomes:

$$\begin{aligned} \int_{CV} \frac{\partial \rho_\phi u\phi}{\partial x} dxdy + \int_{CV} \frac{\partial \rho_\phi v\phi}{\partial y} dxdy = &\int_{CV} \frac{\partial}{\partial x} \Gamma_\phi \frac{\partial \phi}{\partial x} dxdy \\ &+ \int_{CV} \frac{\partial}{\partial y} \Gamma_\phi \frac{\partial \phi}{\partial y} dxdy + \int_{CV} S_\phi dxdy. \end{aligned} \tag{4.1.10}$$

4.1.1 Discretization of the convection terms

The integrand of the first integral term at the left hand side of Equation 4.1.10 contains a derivative in the x direction, thus the discretization of that term is in the x, direction. Since the *area* is always perpendicular to the reference direction, then the infinitesimal volume element in the term under consideration, can be written as:

$$dxdy = A_c \times dx \tag{4.1.11}$$

where $A_c = dy$ is the perpendicular area.

Substituting Equation 4.1.11 into the first term at the left hand side of Equation 4.1.10, the volume integral becomes a line integral. Thus we obtain:

$$\begin{aligned}\int_{CV} \frac{\partial \rho_\phi u\phi}{\partial x} dxdy &= \int_w^e \frac{\partial \rho_\phi u\phi}{\partial x} A_c dx \\ &= \left(\rho_\phi u A_c \phi\right)_e - \left(\rho_\phi u A_c \phi\right)_w \\ &= \left(\rho_\phi u A_c\right)_e \phi_e - \left(\rho_\phi u A_c\right)_w \phi_w \end{aligned} \tag{4.1.12}$$

where w, e are defined in Figure 4.3. $\left(\rho_\phi u A_c\right)_e$ is the convective flux across the eastern interface of the control volume and $\left(\rho_\phi u A_c\right)_w$, is the convective flux across the western interface. Let

$$F_e = \left(\rho_\phi u A_c\right)_e,$$

and

$$F_w = \left(\rho_\phi u A_c\right)_w,$$

then Equation 4.1.12 becomes:

$$\int_{CV} \frac{\partial \rho_\phi u\phi}{\partial x} dxdy = F_e\phi_e - F_w\phi_w. \tag{4.1.13}$$

Similarly, the second volume integral term at the left hand side of Equation 4.1.10 is transformed into a line integral, and then followed by the discretization below:

$$\begin{aligned}\int_{CV} \frac{\partial \rho_\phi v\phi}{\partial y} dxdy &= \int_s^n \frac{\partial \rho_\phi v\phi}{\partial x} A_c dy \\ &= \Big(\rho_\phi v A_c \phi\Big)_n - \Big(\rho_\phi v A_c \phi\Big)_s \\ &= \Big(\rho_\phi v A_c\Big)_n \phi_n - \Big(\rho_\phi v A_c\Big)_s \phi_s, \end{aligned} \tag{4.1.14}$$

where s, n are defined in Figure 4.3 and $\Big(\rho_\phi v A_c\Big)_n, \Big(\rho_\phi v A_c\Big)_s$ are the convective fluxes across the northern and southern interfaces respectively. Let

$$F_n = \Big(\rho_\phi v A_c\Big)_n,$$

and

$$F_s = \Big(\rho_\phi v A_c\Big)_s,$$

then Equation 4.1.14 can be written as:

$$\int_{CV} \frac{\partial \rho_\phi v\phi}{\partial y} dxdy = F_n\phi_n - F_s\phi_s. \tag{4.1.15}$$

Combining the discretized convection terms given by Equations 4.1.13 and 4.1.15, we obtain:

$$\int_{CV} \frac{\partial \rho_\phi u\phi}{\partial x} dxdy + \int_{CV} \frac{\partial \rho_\phi v\phi}{\partial y} dxdy = F_e\phi_e - F_w\phi_w + F_n\phi_n - F_s\phi_s. \tag{4.1.16}$$

4.1.2 Discretization of the diffusion terms

The diffusion terms at the right hand side Equation 4.1.10 are discretized, by using the control volume given by Figure 4.4 to obtain:

$$\begin{aligned}\int_{CV} \frac{\partial}{\partial x}\Gamma_\phi \frac{\partial \phi}{\partial x} dxdy &= \Big(A_c\Gamma_\phi \frac{\partial \phi}{\partial x}\Big)_e - \Big(A_c\Gamma_\phi \frac{\partial \phi}{\partial x}\Big)_w, \\ &= (A_c\Gamma_\phi)_e\Big(\frac{\partial \phi}{\partial x}\Big)_e - (A_c\Gamma_\phi)_w\Big(\frac{\partial \phi}{\partial x}\Big)_w. \end{aligned} \tag{4.1.17}$$

and

$$\int_{CV} \frac{\partial}{\partial y}\Gamma_\phi \frac{\partial \phi}{\partial y} dxdy = \left(A_c \Gamma_\phi \frac{\partial \phi}{\partial y}\right)_n - \left(A_c \Gamma_\phi \frac{\partial \phi}{\partial y}\right)_s,$$
$$= (A_c \Gamma_\phi)_n \left(\frac{\partial \phi}{\partial y}\right)_n - (A_c \Gamma_\phi)_s \left(\frac{\partial \phi}{\partial y}\right)_s. \tag{4.1.18}$$

However, Equation 4.1.17 still contains derivative that must be discretized. At the eastern interface of the control volume, a derivative is approximated by:

$$\left(\frac{\partial \phi}{\partial x}\right)_e = \frac{\phi_E - \phi_P}{\delta x_e}. \tag{4.1.19}$$

The approximations for the other derivatives are as follows:

$$\left(\frac{\partial \phi}{\partial y}\right)_n = \frac{\phi_N - \phi_P}{\delta y_n}, \tag{4.1.20}$$
$$\left(\frac{\partial \phi}{\partial x}\right)_w = \frac{\phi_P - \phi_W}{\delta x_w}, \tag{4.1.21}$$
$$\left(\frac{\partial \phi}{\partial y}\right)_s = \frac{\phi_P - \phi_S}{\delta y_s}, \tag{4.1.22}$$

for the northern, western and southern interfaces respectively. Substituting the approximated derivatives into Equations 4.1.17 and 4.1.18, we obtain:

$$\int_{CV} \frac{\partial}{\partial x}\Gamma_\phi \frac{\partial \phi}{\partial x} dxdy = \frac{(A_c \Gamma_\phi)_e}{\delta x_e}(\phi_E - \phi_P) - \frac{(A_c \Gamma_\phi)_w}{\delta x_w}(\phi_P - \phi_W), \tag{4.1.23}$$

and

$$\int_{CV} \frac{\partial}{\partial y}\Gamma_\phi \frac{\partial \phi}{\partial y} dxdy = \frac{(A_c \Gamma_\phi)_n}{\delta y_n}(\phi_N - \phi_P) - \frac{(A_c \Gamma_\phi)_s}{\delta y_s}(\phi_P - \phi_S). \tag{4.1.24}$$

The coefficients; $\frac{(A_c\Gamma_\phi)_e}{\delta x_e}$, $\frac{(A_c\Gamma_\phi)_w}{\delta x_w}$, $\frac{(A_c\Gamma_\phi)_n}{\delta y_n}$, and $\frac{(A_c\Gamma_\phi)_s}{\delta y_s}$ are the diffusive fluxes across the control volume, at the eastern, western, northern and southern interfaces, respectively. Let

$$D_e = \frac{(A_c \Gamma_\phi)_e}{\delta x_e}, \quad D_w \frac{(A_c \Gamma_\phi)_w}{\delta x_w}, \quad D_n = \frac{(A_c \Gamma_\phi)_n}{\delta y_n}, \text{ and } D_s = \frac{(A_c \Gamma_\phi)_s}{\delta y_s}, \tag{4.1.25}$$

then Equations 4.1.23 and 4.1.24 can be written as:

$$\int_{CV} \frac{\partial}{\partial x}\Gamma_\phi \frac{\partial \phi}{\partial x} dxdy = D_e(\phi_E - \phi_P) - D_w(\phi_P - \phi_W), \tag{4.1.26}$$

and

$$\int_{CV} \frac{\partial}{\partial y}\Gamma_\phi \frac{\partial \phi}{\partial y} dxdy = D_n(\phi_N - \phi_P) - D_s(\phi_P - \phi_S). \tag{4.1.27}$$

Combining Equations 4.1.26 and 4.1.27, the discretization for the diffusive transport terms is given by:

$$\begin{aligned}\int_{CV} \frac{\partial}{\partial x}\Gamma_\phi \frac{\partial \phi}{\partial x} dxdy + \int_{CV} \frac{\partial}{\partial y}\Gamma_\phi \frac{\partial \phi}{\partial y} dxdy = \\ D_e(\phi_E - \phi_P) - D_w(\phi_P - \phi_W) \\ + D_n(\phi_N - \phi_P) - D_s(\phi_P - \phi_S).\end{aligned} \tag{4.1.28}$$

4.1.3 Discretization of the source term

The discretization for the source term (last term at the right hand side of Equation 4.1.10 is given by:

$$\int_{CV} S_\phi dxdy = \bar{S}_\phi \Delta x_P \Delta y_P, \tag{4.1.29}$$

where $\bar{S}_\phi$ indicates an average of S_ϕ.

However, the source term is usually a function of the unknown variable. This function can be a polynomial of any degree in the unknown variable. Following the discretization procedure for conservation laws, developed by [65] and [28], the linearised average source term is given by:

$$\bar{S}_\phi = S_C + S_P \phi_P. \tag{4.1.30}$$

For higher degree (degree > 1) polynomial source terms, iterative methods are appropriate for solving the resulting linear system [65]. Substituting Equation 4.1.30 into Equation 4.1.29, the discretized source term for the transport equation is given by:

$$\int_{CV} S_\phi dxdy = S_C \Delta x_P \Delta y_P + S_P \Delta x_P \Delta y_P \ \phi_P. \tag{4.1.31}$$

4.1.4 Discretized steady transport equation

Combining the discretized convection terms given by Equation 4.1.16, the diffusion terms given by Equation 4.1.28 and the linearised source term given by Equation 4.1.31, we obtain the discretization for the steady transport Equation 4.1.1 as:

$$\begin{aligned} F_e\phi_e - F_w\phi_w + F_n\phi_n - F_s\phi_s = {} & D_e(\phi_E - \phi_P) - D_w(\phi_P - \phi_W) \\ & + D_n(\phi_N - \phi_P) - D_s(\phi_P - \phi_S) \\ & + S_C\Delta x_P\Delta y_P + S_P\Delta x_P\Delta y_P\ \phi_P. \end{aligned} \tag{4.1.32}$$

Furthermore, from Figure 4.3 it can be observed that the notations; e, w, n, s that correspond to control volume interfaces, do not coincide with the main grid points where the unknown variable ϕ is defined. Therefore, the values; $\phi_e, \phi_w, \phi_n, \phi_s$ in Equation 4.1.32 do not coincide with main grid points, thus must be interpolated from neighbouring values on main grid points. There are many approximating schemes for such cases, however, we only discuss the upwind, central differencing and the hybrid schemes.

4.1.5 Central differencing scheme

When the approximation of the unknown variable is a weighted mean of neighbouring values, then the scheme is a piece-wise linear scheme. A second order piece-wise linear scheme, approximates the values of ϕ at the control volume interface as follows:

$$\phi_e = \frac{\delta x_{e^+}\ \phi_P + \delta x_{e^-}\ \phi_E}{\delta x_e} = f_e\phi_P + (1 - f_e)\phi_E, \tag{4.1.33}$$

$$\phi_w = \frac{\delta x_{w^+}\ \phi_P + \delta x_{w^-}\ \phi_W}{\delta x_w} = f_w\phi_P + (1 - f_w)\phi_W, \tag{4.1.34}$$

$$\phi_n = \frac{\delta y_{n^+}\ \phi_P + \delta y_{n^-}\ \phi_N}{\delta y_n} = f_n\phi_P + (1 - f_n)\phi_N, \tag{4.1.35}$$

$$\phi_s = \frac{\delta y_{s^+}\ \phi_P + \delta y_{s^-}\ \phi_S}{\delta y_s} = f_s\phi_P + (1 - f_s)\phi_S. \tag{4.1.36}$$

In the case of a uniform grid, the weighted mean is equal to arithmetic mean and the piece-wise linear scheme is called central differencing scheme. The important feature

of the central differencing scheme is that, it assumes the control volume interfaces are located midway between main grid points. Thus the approximations for ϕ at the control volume interfaces, by the central differencing scheme are given by:

$$\phi_e = \frac{\phi_P + \phi_E}{2}, \tag{4.1.37}$$

$$\phi_w = \frac{\phi_P + \phi_W}{2}, \tag{4.1.38}$$

$$\phi_n = \frac{\phi_P + \phi_N}{2}, \tag{4.1.39}$$

$$\phi_s = \frac{\phi_P + \phi_S}{2}. \tag{4.1.40}$$

Substituting the central differencing approximations of ϕ, in the left hand side of Equation 4.1.32, we have:

$$\begin{aligned} F_e\phi_e - F_w\phi_w + F_n\phi_n - F_s\phi_s = F_e\Big(\frac{\phi_P + \phi_E}{2}\Big) - F_w\Big(\frac{\phi_P + \phi_W}{2}\Big) \\ + F_n\Big(\frac{\phi_P + \phi_S}{2}\Big) - F_s\Big(\frac{\phi_P + \phi_S}{2}\Big). \end{aligned} \tag{4.1.41}$$

Substituting Equation 4.1.41 into Equation 4.1.32 and rearranging the resulting terms, we obtain:

$$\begin{aligned} \Big(D_e - \frac{F_e}{2} + D_w + \frac{F_w}{2} + D_n - \frac{F_n}{2} + D_s + \frac{F_s}{2} \\ +(F_e - F_w) + (F_n - F_s) - S_P\Delta x_P\Delta y_P\Big)\phi_P = \\ \Big(D_e - \frac{F_e}{2}\Big)\phi_E + \Big(D_w + \frac{F_w}{2}\Big)\phi_W \\ + \Big(D_n - \frac{F_n}{2}\Big)\phi_N \\ + \Big(D_s + \frac{F_s}{2}\Big)\phi_S, \\ + S_C\Delta x_P\Delta y_P. \end{aligned} \tag{4.1.42}$$

In a compact form, Equation 4.1.42 is written as follows:

$$a_P\phi_P = a_E\phi_E + a_W\phi_W + a_N\phi_N + a_S\phi_S + b, \tag{4.1.43}$$

where the coefficients a_E, a_W, a_S, a_N and b are defined in Table 4.2 and the central coefficient is given by:

$$a_P = a_E + a_W + a_S + a_N + (F_e - F_w) + (F_n - F_s) - S_P\Delta x_P\Delta y_P.$$

a_W	a_E	a_N	a_S	b
$D_w + \frac{F_w}{2}$	$D_E - \frac{F_e}{2}$	$D_n - \frac{F_n}{2}$	$D_s + \frac{F_s}{2}$	$S_C \Delta x_P \Delta y_P$

Table 4.2: Central difference coefficients for Equation 4.1.43 [65, 28].

Equation 4.1.43 is the final discretization for any two dimensional steady scalar transport equation. However, the coefficient in the equations are evaluated using expressions that differ for different discretization schemes.

4.1.6 Upwind differencing scheme

The upwind scheme takes the flow direction into consideration. The upstream values of ϕ, that are on neighbouring main grid points are used to approximate the interface values. In the case of a two-dimensional control volume, the possible directions include:

- $u_w > 0$ and $u_e > 0$, which implies that $F_w > 0$ and $F_e > 0$. Figure 4.5 illustrates this possibility. For this possibility, the interface values are approximated by setting $\phi_w = \phi_W$, and $\phi_e = \phi_P$.
- $v_s > 0$ and $v_n > 0$, which implies that $F_s > 0$ and $F_n > 0$. For this possibility, the interface values are approximated as follows $\phi_s = \phi_S$, and $\phi_n = \phi_P$.
- $u_w < 0$ and $u_e < 0$, which implies that $F_w < 0$ and $F_e < 0$. Figure 4.6 illustrates this possibility. For such a case, the interface values are approximated by setting $\phi_w = \phi_P$, and $\phi_e = \phi_E$.
- $v_s < 0$ and $v_n < 0$, which implies that $F_s < 0$ and $F_n < 0$. For this case, the interface values are approximated as follows $\phi_s = \phi_P$, and $\phi_n = \phi_N$.

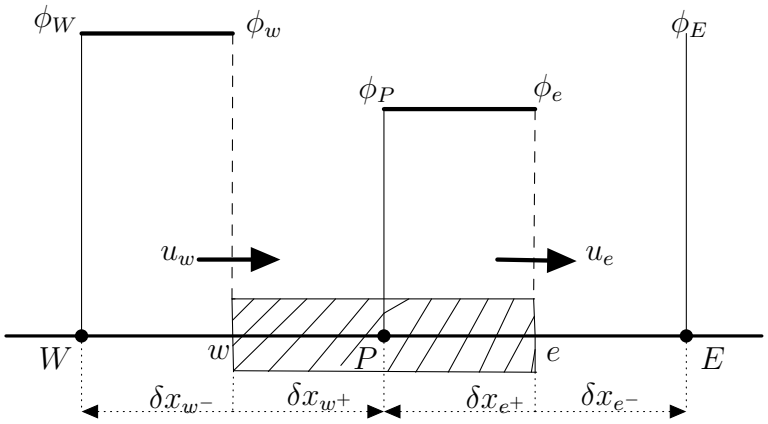

Figure 4.5: Flow in and out of a control volume from left to right.

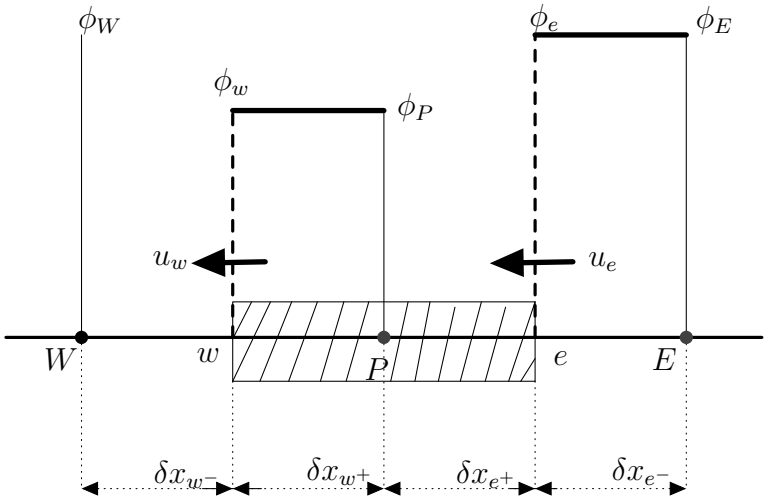

Figure 4.6: Flow in and out of a control volume from right to left.

By the first two possibilities, the left hand side of the discretized transport Equation 4.1.32 becomes:

$$F_e\phi_e - F_w\phi_w + F_n\phi_n - F_s\phi_s = F_e\phi_P - F_w\phi_W + F_n\phi_P - F_s\phi_S, \tag{4.1.44}$$

which implies that:

$$\begin{aligned} F_e\phi_P - F_w\phi_W + F_n\phi_P - F_s\phi_S = {} & D_e(\phi_E - \phi_P) - D_w(\phi_P - \phi_W) \\ & + D_n(\phi_N - \phi_P) - D_s(\phi_P - \phi_S) \\ & + S_C\Delta x_P\Delta y_P + S_P\Delta x_P\Delta y_P\phi_P. \end{aligned} \tag{4.1.45}$$

Grouping like-terms, we obtain a linear system (Equation 4.1.43) as in the case of the central differencing scheme, but the coefficients a_E, a_W, a_S, a_N and b are defined in Table 4.3 and the central coefficient is given by:

$$a_P = a_E + a_W + a_S + a_N + (F_e - F_w) + (F_n - F_s) - S_P\Delta x_P\Delta y_P.$$

Coefficient	a_W	a_E	a_N	a_S	b
$F_e > 0, F_w > 0$, and $F_s > 0, F_n > 0$	$D_w + F_w$	D_e	D_n	$D_s + F_s$	$S_C\Delta x_P\Delta y_P$

Table 4.3: Upwind coefficients for Equation 4.1.43, when the flow is from left to right.

Taking the last two possibilities into consideration, the left hand side of the discretized transport Equation 4.1.32 becomes:

$$F_e\phi_e - F_w\phi_w + F_n\phi_n - F_s\phi_s = F_e\phi_E - F_w\phi_P + F_n\phi_N - F_s\phi_P, \tag{4.1.46}$$

which implies that:

$$\begin{aligned} F_e\phi_E - F_w\phi_P + F_n\phi_N - F_s\phi_P = {} & D_e(\phi_E - \phi_P) - D_w(\phi_P - \phi_W) \\ & + D_n(\phi_N - \phi_P) - D_s(\phi_P - \phi_S) \\ & + S_C\Delta x_P\Delta y_P + S_P\Delta x_P\Delta y_P\phi_P. \end{aligned} \tag{4.1.47}$$

Coefficient	a_W	a_E	a_N	a_S	b
$F_e < 0, F_w < 0$, and $F_s < 0, F_n < 0$.	D_w	$D_e - F_e$	$D_n - F_n$	D_s	$S_C \Delta x_P \Delta y_P$

Table 4.4: Upwind coefficients for Equation 4.1.43, when the flow is from right to left.

Grouping like-terms, we obtain the linear system defined by Equation 4.1.43, with the coefficients a_E, a_W, a_S, a_N and b defined by Table 4.4.

The upwind coefficients for a general case, which satisfies all the four conditions, is given by Table 4.5 [65, 28].

a_W	a_E	a_N	a_S	b
$D_w + \max(F_w, 0)$	$D_e + \max(-F_e, 0)$	$D_n + \max(-F_n, 0)$	$D_s + \max(F_s, 0)$	$S_C \Delta x_P \Delta y_P$

Table 4.5: Generalized upwind coefficients for Equation 4.1.43. [65, 28]

4.1.7 Hybrid scheme

The hybrid scheme is a combination of the upwind and central differencing schemes. Peclet number which is a ratio of convective and diffusive fluxes is used to combine both schemes. At each interface of the control volume, the Peclet number can be evaluated using the convective flux and diffusive conductance at that interface, e.g. at the northern interface, the Peclet number is calculated as follows:

$$Pe_n = \frac{F_n}{D_n}.$$

If $-2 < Pe_n < 2$, the approximation for ϕ_n is the central differencing approximation. Otherwise, the approximation for ϕ_n is given by the upwind differencing scheme. According to [28, 65], the coefficients for the linear system 4.1.43, obtained by using the hybrid scheme, are given by:

$$a_W = \max\left[F_w, \left(D_w + \frac{F_w}{2}\right), 0\right] \tag{4.1.48}$$

$$a_E = \max\left[-F_e, \left(D_e - \frac{F_e}{2}\right), 0\right] \tag{4.1.49}$$

$$a_N = \max\left[-F_n, \left(D_n - \frac{F_n}{2}\right), 0\right] \tag{4.1.50}$$

$$a_S = \max\left[F_s, \left(D_s + \frac{F_s}{2}\right), 0\right] \tag{4.1.51}$$

$$b = S_C \Delta x_P \Delta y_P. \tag{4.1.52}$$

The central coefficient a_P is same as with the other schemes.

4.2 Properties of a discretization scheme

There are many numerical schemes, however, schemes that produce physically relevant solutions have some common properties. These properties include conservativeness, boundedness and transportiveness.

4.2.1 Conservativeness

Discretization schemes must ensure that the flux across control volume interfaces is the same, if there is no source or sink. The conservativeness of a scheme is enforced by the consistency rule, which states that [65]:

" *When a face is common to two adjacent control volumes, the flux across it must be represented by the same expression in the discretization equations for the two control volumes.*"

All the three schemes used in this work, are consistent at control volume interfaces, since the unknown variable ϕ and its gradients at the control volume interfaces are uniquely defined by the schemes.

4.2.2 Boundedness

Considering the steady state Equation 4.1.1, its final discretization, Equation 4.1.43, is a linear equation, which may be solved by direct or iterative methods. The iterative methods start with a guessed solution, then successively update until convergence. We refer to [65, 28] for a detailed discussion.

However, convergence is not always guaranteed, thus a sufficient condition for convergence, called Scarborough criterion, which is expressed in terms of the coefficients in the linear system is given by [65, 28]:

$$\frac{\sum |a_{nb}|}{|a_P|} \begin{cases} \leq 1: & \textit{at all main grid points} \\ < 1: & \textit{atleast one main grid point} \end{cases}$$

Where $\sum |a_{nb}|$ is the sum of all neighbouring coefficients. It should be noted here that, the expression for a_P contains the gradient of ϕ (S_P) from the linearised source term. If this criterion is satisfied, then the scheme produces coefficients that result in a diagonally dominant matrix.

The boundedness property is satisfied when the following rules are observed by the numerical schemes:

1. The central coefficient a_P, forms the diagonal elements in the coefficient matrix for the linear system given by Equation 4.1.43. Achieving diagonal dominance implies that the central coefficient a_P, is larger than the other coefficients. It can be observed in the expression for the central coefficient ($a_P = \sum a_{nb} - S_P \Delta x_P \Delta y_P$) that the guarantee for diagonal dominance is when $S_P < 0$, thus the first rule is [65]:

   "The linearised source term, $\bar{S}_\phi = S_C + S_P \phi$, must have a negative slope, therefore $S_P \leq 0$."

2. Without sources and sinks, the central coefficient is the sum of all the neighbouring coefficients. that is [65]:
   "In the absence of a source, $a_P = \sum a_{nb}$."

3. It can be deduced from rule 2, that if one or all the neighbouring coefficient are negative, diagonal dominance may not be achieved. Thus another rule that guarantees diagonal dominance is [65]:
   "All the neighbouring coefficients, $a_{nb,}$ as well as the central coefficient a_P must be positive."

4.2.3 Transportiveness

Flow directions can influence transportation of a quantity at any grid point. Peclet number, which is a dimensionless ratio of convective transport to diffusive transport, is used to quantitatively describe transportiveness.

When the Peclet number (Pe) is zero, there is no convective transport, only diffusion. The effect of diffusion in an isotropic medium is to spread the quantity evenly in all directions (see Figure 4.7).

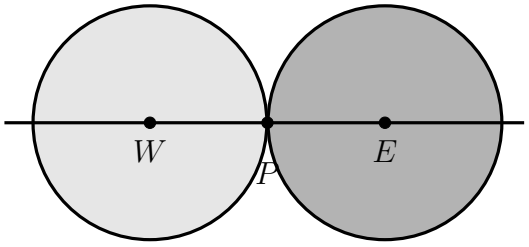

Figure 4.7: Pure diffusion $P_e \to 0$, for an isotropic medium. This figure is reproduced from [28].

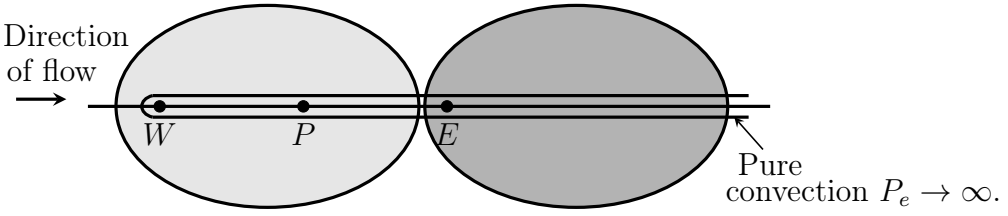

Figure 4.8: Convection and diffusion. This figure is reproduced from [28].

In Figure 4.7, two point sources at W and E spread out evenly (due to diffusion) at the same rate, thus their effects or influence at point P is the same.

In the presence of both convection and diffusion, the Peclet number is non-zero. Convection introduces directional dependence into the transport process. In Figure 4.8, the direction of influence is from left to right. It can be observed from the Figure 4.8 that, point P is only affected by transported quantity from point W. One can observe that concentric circles in the pure diffusion process, have turned into ellipses. As the Peclet number goes to infinity, (implying that convection is dominant), the effect of diffusion can not be noticed, and the elliptic lines are completely stretched-out.

Apart from the central differencing scheme, the other schemes considered in the discussion satisfy the transportiveness property [65, 28]. We conclude here that, the schemes considered in this work are qualitatively capable of providing physically relevant solutions to our model.

4.3 Discretization of a time-dependent transport equation

In this section, we discuss the discretization procedure for a generalised scalar time-dependent transport equation. That is:

$$\frac{\partial \rho_\phi \phi}{\partial t} + \frac{\partial (\rho_\phi u \phi)}{\partial x} + \frac{\partial (\rho_\phi v \phi)}{\partial y} = \frac{\partial}{\partial x}\left(\Gamma_\phi \frac{\partial \phi}{\partial x}\right) + \frac{\partial}{\partial y}\left(\Gamma_\phi \frac{\partial \phi}{\partial y}\right) + S_\phi, \qquad x, y \in \Omega_d, \quad t \in [0, \top], \tag{4.3.1}$$

Where $\top$ is the final time. The time period is also partitioned to obtain a time grid. Let $N_\top$ be the total number of points on the time grid, then the time step size Δt, is given by:

$$\Delta t = \frac{\top}{N_\top}. \tag{4.3.2}$$

Integrating the time-dependent Equation 4.3.1 over the control volume given above by

Figure 4.4, and over a time grid, we obtain:

$$\int_t^{t+\Delta t}\int_{CV}\frac{\partial \rho_\phi \phi}{\partial t}dV\,dt+\int_t^{t+\Delta t}\int_{CV}\frac{\partial(\rho_\phi u\phi)}{\partial x}dV\,dt+\int_t^{t+\Delta t}\int_{CV}\frac{\partial(\rho_\phi v\phi)}{\partial y}dV\,dt=$$
$$\int_t^{t+\Delta t}\int_{CV}\frac{\partial}{\partial x}\Big(\Gamma_\phi\frac{\partial\phi}{\partial x}\Big)dV\,dt+\int_t^{t+\Delta t}\int_{CV}\frac{\partial}{\partial y}\Big(\Gamma_\phi\frac{\partial\phi}{\partial y}\Big)dV\,dt+\int_t^{t+\Delta t}\int_{CV}S_\phi dV\,dt. \tag{4.3.3}$$

To avoid complicated long expressions in the discretization process, we first integrate over the control volume, and then follow with time integration. Thus integrating over the control volume, we obtain:

$$\int_{CV}\frac{\partial \rho_\phi \phi}{\partial t}dV+\int_{CV}\frac{\partial(\rho_\phi u\phi)}{\partial x}dV+\int_{CV}\frac{\partial(\rho_\phi v\phi)}{\partial y}dV=$$
$$\int_{CV}\frac{\partial}{\partial x}\Big(\Gamma_\phi\frac{\partial\phi}{\partial x}\Big)dV+\int_{CV}\frac{\partial}{\partial y}\Big(\Gamma_\phi\frac{\partial\phi}{\partial y}\Big)dV+\int_{CV}S_\phi dV. \tag{4.3.4}$$

By following the procedure used in the steady case discussed in the previous section, Equation 4.3.4 can be written into the semi-discretized equation:

$$\int_{CV}\frac{\partial \rho_\phi \phi}{\partial t}dV+a_P\phi_P=a_E\phi_E+a_W\phi_W+a_N\phi_N+a_S\phi_S+b, \tag{4.3.5}$$

where the coefficients a_W, a_E, a_N, a_S, b and a_P are given by any of the discretization schemes discussed above. By comparing the steady equation and the time-dependent equation, it can be observed that unsteady integral term at the left hand side of Equation 4.3.5 is part of the source term in Equation 4.1.3. Thus we first treat the unsteady integral term like a source term, and then discretize later in time. The final discretization over the control volume is given by:

$$\frac{\partial \rho_\phi \phi}{\partial t}\Delta x_P\Delta y_P+a_P\phi_P=a_E\phi_E+a_W\phi_W+a_N\phi_N+a_S\phi_S+b. \tag{4.3.6}$$

Since Equation 4.3.6 still contains a derivative (a time derivative), we integrate over the

time period. Thus we have:

$$\int_t^{t+\Delta t} \frac{\partial \rho_\phi \phi}{\partial t} \Delta x_P \Delta y_P dt + \int_t^{t+\Delta t} a_P \phi_P dt = \int_t^{t+\Delta t} a_E \phi_E dt + \int_t^{t+\Delta t} a_W \phi_W dt + \int_t^{t+\Delta t} a_N \phi_N dt + \int_t^{t+\Delta t} a_S \phi_S dt + \int_t^{t+\Delta t} b dt. \tag{4.3.7}$$

The time derivative in Equation 4.3.7 is approximated by [28, 65]

$$\frac{\partial \phi}{\partial t} = \frac{\phi_P - \phi_P^o}{\Delta t}. \tag{4.3.8}$$

If the density is constant, the discretization for the time integral is given by:

$$\int_t^{t+\Delta t} \frac{\partial \rho_\phi \phi}{\partial t} \Delta x_P \Delta y_P dt = \frac{\rho_\phi \Delta x_P \Delta y_P}{\Delta t} (\phi_P - \phi_P^o), \tag{4.3.9}$$

where ϕ_P^o is the previous value of ϕ at grid point P.

Replacing the first integral in Equation 4.3.7 by using Equation 4.3.9 we obtain:

$$\rho_\phi \Delta x_P \Delta y_P (\phi_P - \phi_P^o) + \int_t^{t+\Delta t} a_P \phi_P dt = \int_t^{t+\Delta t} a_E \phi_E dt + \int_t^{t+\Delta t} a_W \phi_W dt + \int_t^{t+\Delta t} a_N \phi_N dt + \int_t^{t+\Delta t} a_S \phi_S dt + \int_t^{t+\Delta t} b dt. \tag{4.3.10}$$

Discretization of the integral terms in Equation 4.3.10 can be achieved, by a weighted mean of the integrands at a given grid point. An example is [65, 28]:

$$\int_t^{t+\Delta t} \phi_P dt = \Big(\xi \phi_P + (1-\xi)\phi_P^o\Big) \Delta t, \tag{4.3.11}$$

where $0 \leq \xi \leq 1$, is a control parameter for controlling the influence of ϕ in different times on the current value. Thus by Equation 4.3.11, the time integrals in Equation 4.3.10 are discretized to obtain:

$$\rho_\phi \Delta x_P \Delta y_P(\phi_P - \phi_P^o) + a_P\Big(\xi\phi_P + (1-\xi)\phi_P^o\Big)\Delta t = a_E\Big(\xi\phi_E + (1-\xi)\phi_E^o\Big)\Delta t + a_W\Big(\xi\phi_W + (1-\xi)\phi_W^o\Big)\Delta t + a_N\Big(\xi\phi_N + (1-\xi)\phi_N^o\Big)\Delta t + a_S\Big(\xi\phi_S + (1-\xi)\phi_S^o\Big)\Delta t + b\Delta t. \tag{4.3.12}$$

Dividing both sides of Equation 4.3.12 by Δt and rearranging the resulting terms, we have:

$$\Big(a_P^o + a_P\xi\Big)\phi_P = \Big(a_P^o - a_P(1-\xi)\Big)\phi_P^o + a_E\Big(\xi\phi_E + (1-\xi)\phi_E^o\Big) + a_W\Big(\xi\phi_W + (1-\xi)\phi_W^o\Big) + a_N\Big(\xi\phi_N + (1-\xi)\phi_N^o\Big) + a_S\Big(\xi\phi_S + (1-\xi)\phi_S^o\Big) + b, \tag{4.3.13}$$

where $a_P^o = \frac{\rho_\phi \Delta x_P \Delta y_P}{\Delta t}$.

4.3.1 Fully implicit scheme

When the control parameter is exactly one, the scheme is fully implicit. Thus Equation 4.3.13 reduces to the following:

$$\Big(a_P^o + a_P\Big)\phi_P = a_P^o\phi_P^o + a_E\phi_E + a_W\phi_W + a_N\phi_N + a_S\phi_S + b. \tag{4.3.14}$$

By observing Equation 4.3.14, it can be qualitatively concluded that the scheme satisfies all the rules discussed above, especially the rule concerning positivity of coefficients. Since the coefficients are always positive, the implicit scheme is unconditionally stable, and it is first order accurate.

4.3.2 Explicit scheme

When the control parameter is zero, the scheme is explicit. Thus Equation 4.3.13 reduces to the following:

$$a_P^o \phi_P = (a_P^o - a_P)\phi_P^o + a_E \phi_E^o + a_W \phi_W^o + a_N \phi_N^o + a_S \phi_S^o + b. \tag{4.3.15}$$

For the explicit discretization (Equation 4.3.15), the coefficient $a_P^o - a_P$, is capable of violating the positivity rule. The violation occurs when $a_P^o - a_P < 0$, thus a_P^o must always be less than a_P to ensure numerical stability. The explicit scheme is first order accurate, with regards to a Taylor series truncation error.

4.4 Summary

In this Chapter, a uniform flow is assumed for simplicity and a constant pressure gradient is also assumed. The finite volume discretization method is used to discretize the resulting partial differential equations on a rectangular domain. Central differencing, Upwind and hybrid schemes are used for approximating the coefficients in the linear systems. The finite difference method is used to obtain implicit and explicit time marching schemes.

Chapter 5

Results and Discussion

5.1 Accuracy and stability test for numerical schemes

In this section, we assess the accuracy of numerical schemes that were discussed in Chapter 4. A one-dimensional convection-diffusion equation that has an analytical solution is used for the assessment.

(1). **Spatial discretization schemes**

Spatial discretization schemes are applied to a steady case of the one-dimensional convection-diffusion equation whose analytical solution and parameter values are given by Example (5.1) of [28]. Table 5.1 contains the data for testing the accuracy of spatial schemes.

Parameter	Numerical Value	Units of measurement
L_x	1.0	m
ρ_ϕ	1.0	kg/m^3
Γ_ϕ	0.1	$kg/m.s$
u	$0.1, 2.5$	m/s
Boundary $\phi_L = \phi(0)$ Boundary $\phi_R = \phi(L_x)$	1.0 0.0	depends on ϕ depends on ϕ

Table 5.1: Accuracy test data for spatial numerical schemes [28].

The analytical solution for the one-dimensional convection-diffusion equation is given by [28]:

$$\phi(x) = \phi_L + \frac{(\phi_R - \phi_L) \times \left(\exp(\frac{\rho_\phi u x}{\Gamma_\phi}) - 1 \right)}{\exp(\frac{\rho_\phi u L_x}{\Gamma_\phi}) - 1}. \tag{5.1.1}$$

(2). **Time discretization schemes**

For the time discretization schemes, data for accuracy test is taken from Example (8.1) of [28]. Table 5.2 contains the input data for assessing the accuracy of the time discretization scheme.

Parameter	**Numerical Value**	**Units of measurement**
Lx	2×10^{-2}	m
ρ_ϕ	10^7	$J/m^3.K$
Γ_ϕ	10	$W/m.K$
u	0	m/s
Boundary condition; $\frac{\partial \phi}{\partial x}(0,t)$	0	$^oC/m$
Boundary condition; $\phi(Lx,t)$	0	^oC
Initial condition $\phi_0 = \phi(x,0)$	2×10^2	^oC

Table 5.2: Accuracy test data for time discretization schemes [28].

The analytical solution for the one-dimensional time-dependent transport equation, used for the accuracy test is given by [28]:

$$\phi(x,t) = \frac{4\phi_0}{\pi} \sum_{n=1}^{\infty} \frac{(-1)^{n+1}}{2n-1} \exp(-\alpha_n \lambda_n^2 t) \cos(\lambda_n x), \tag{5.1.2}$$

where

$$\lambda_n = \frac{(2n-1)\pi}{2Lx},$$

and

$$\alpha_n = \frac{\Gamma_\phi}{\rho_\phi}.$$

Some of the results obtained in our study do not match exactly with results obtained in [28]. The discrepancy is attributed to rounding and truncation errors.

5.1.1 Accuracy and stability test for central differencing scheme

The numerical solution for a course grid of five (5) points, obtained by using central differencing coefficients is given by the graph at the left hand side of Figure 5.1. The relative error across the domain is given by the graph at the right hand of Figure 5.1.

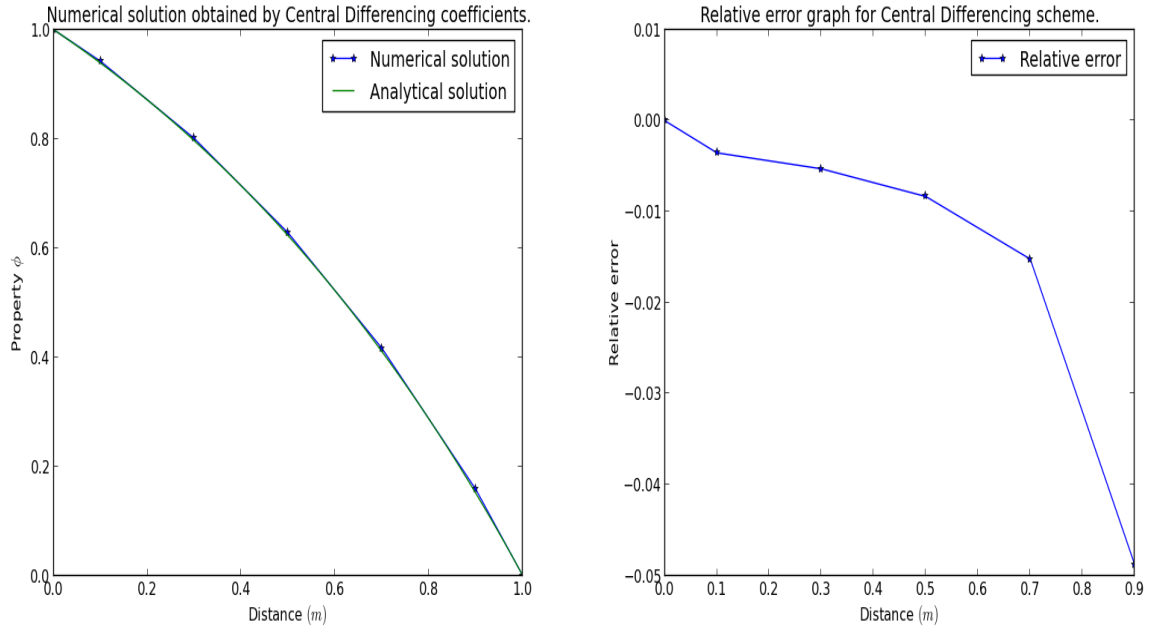

Figure 5.1: Comparing analytical solution 5.1.1 with central differencing solution for a course grid.

It can be observed from Figure 5.1 that even for a course grid of five (5) points, the central differencing scheme gives a good approximation of the analytical solution 5.1.1. Effects of grid size (number of grid points) on the numerical solution is investigated. The graph at the left hand side of Figure 5.2 shows a comparison of the analytical solution with the central differencing solution obtained by using 15 grid points. The graph at the right hand side of Figure 5.2 shows a comparison of the analytical solution 5.1.1 with the central differencing solution, obtained by using 25 grid points.

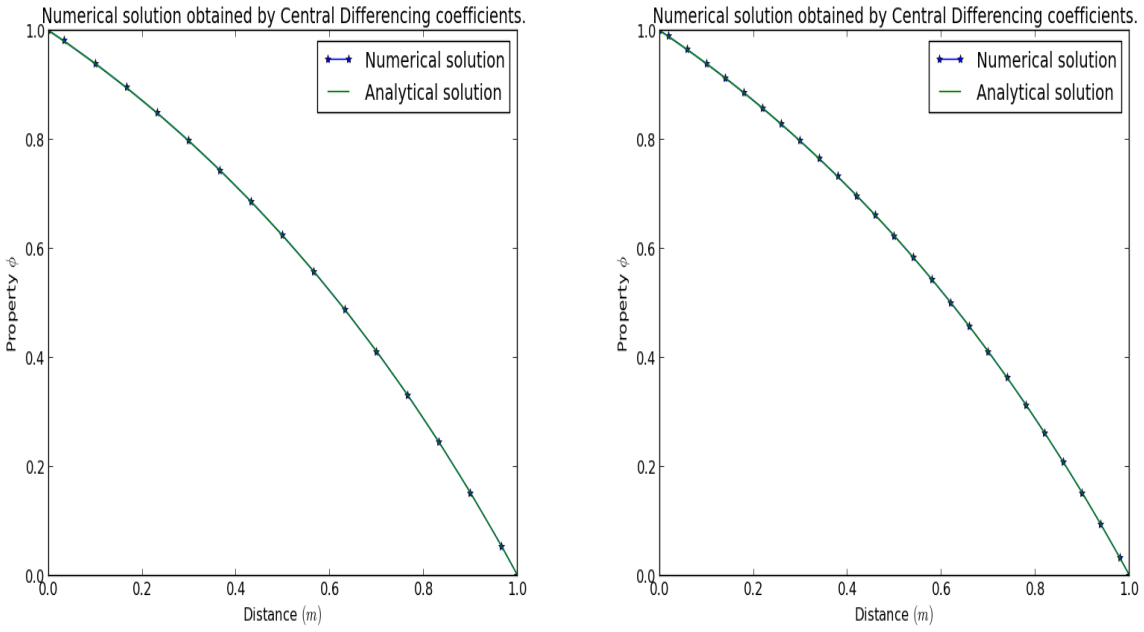

Figure 5.2: Comparing the analytical solution 5.1.1 with central differencing solutions for finer grids.

From Figure 5.2, it can be qualitatively concluded the central differencing solution converges to the exact solution as the grid becomes finer (implying smaller step sizes or more grid points). Thus the central differencing scheme can be used to obtain good numerical approximations.

However, the velocity used to obtain Figures 5.1 and 5.2 is 0.1 m/s. When the velocity was set to 2.5 m/s, the central differencing solution oscillated about the analytical solution as shown in Figure 5.3.

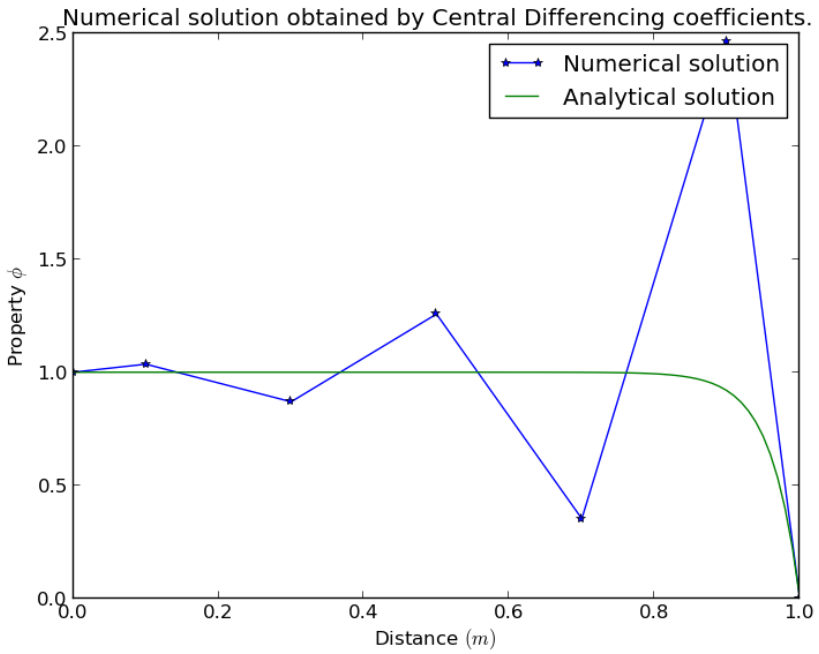

Figure 5.3: Comparing central differencing solution and analytical solution for a high Peclet number.

The calculated Peclet number for the case where the velocity is 0.1 m/s, is 0.2, while the calculated Peclet number for the case where the velocity is 2.5 m/s, is 5. Since 5 is a higher value (> 2,), the transportiveness property must be satisfied to obtain numerical stability as discussed in Chapter 4. The instability of the central differencing solution suggest that, the scheme is not reliable and must be used with other schemes.

5.1.2 Accuracy and stability test for the upwind scheme

The numerical solution for a course grid of five (5) points, obtained by using the upwind coefficients is given by the graph at the left hand side of Figure 5.4. The relative error across the domain is given by the graph at the right hand side of Figure 5.4.

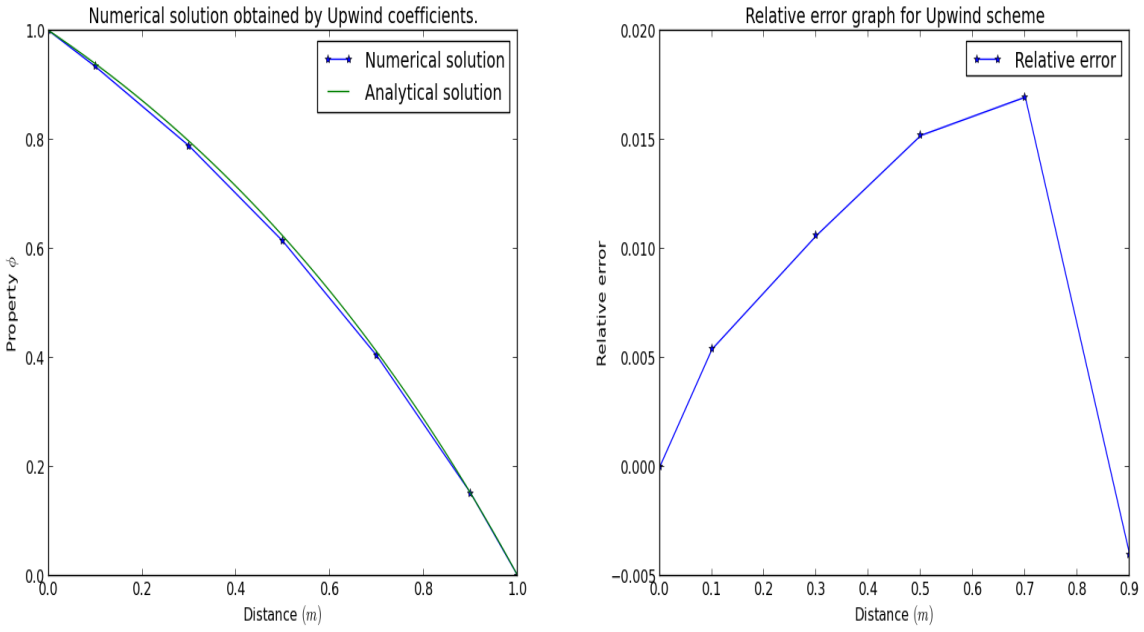

Figure 5.4: Comparing analytical solution 5.1.1 with upwind solution for a course grid.

It can be observed from Figure 5.4 that even for a course grid of five (5) points, the upwind scheme gives a good approximation of the analytical solution 5.1.1.

Effects of grid size (number of grid points) on convergence is also investigated, the graph at the left hand side of Figure 5.5 shows a comparison of the analytical solution with the upwind solution obtained by using 15 grid points. The graph at the right hand side of Figure 5.5 shows a comparison of the analytical solution 5.1.1 and the upwind solution, obtained by using 25 grid points.

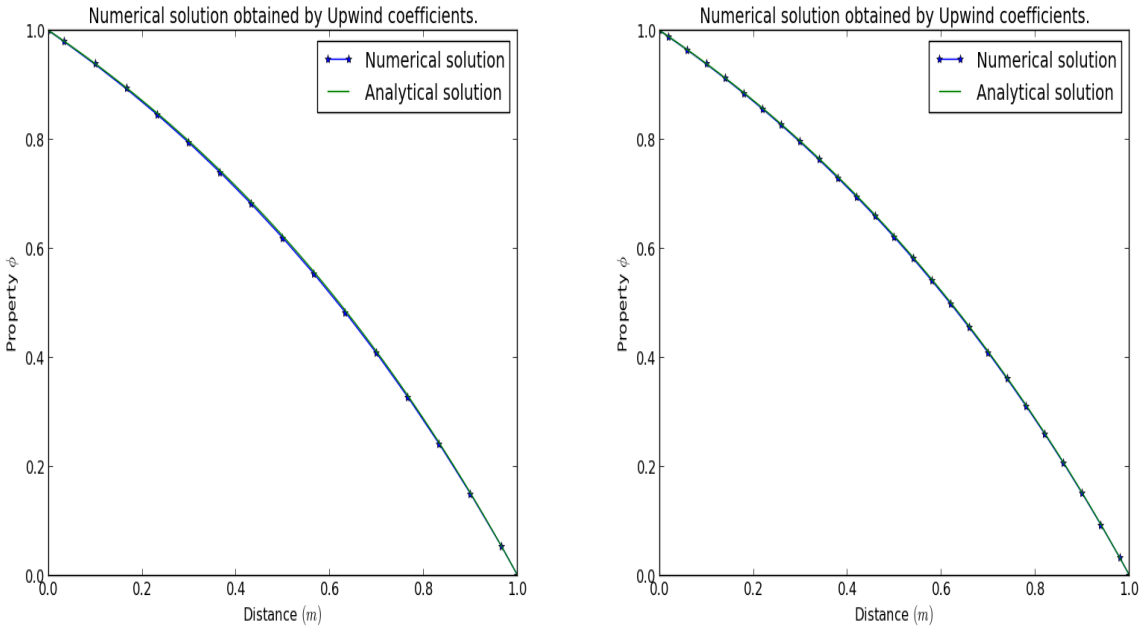

Figure 5.5: Comparing the analytical solution 5.1.1 with upwind solutions for finer grids.

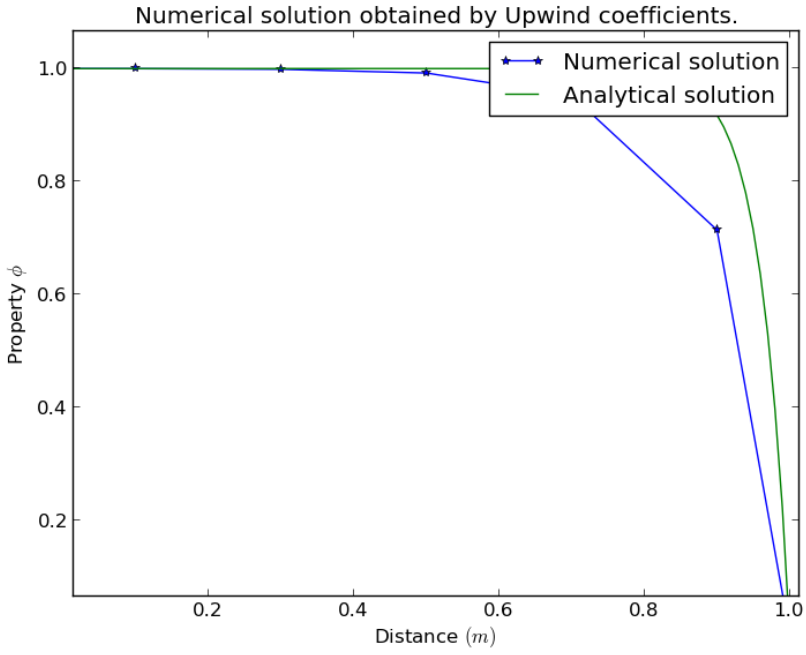

Figure 5.6: Comparing upwind solution and analytical solution for a high Peclet number.

From the results given by Figure 5.5, it can be qualitatively concluded that the upwind solution converges to the exact solution as the grid becomes finer (implying smaller step sizes or more grid points). Thus for more accuracy a finer grids should be used.

However, effects of a high Peclet number on the upwind solution is also investigated. Figure 5.6 shows a comparison of the analytical solution and the upwind solution for a Peclet number of 5.

The results in Figure 5.6 do not contain oscillations because the upwind scheme satisfies the transportiveness property. The observed results imply that the upwind scheme is reliable high Peclet number problems.

5.1.3 Accuracy and stability test for hybrid scheme

The numerical solution for a course grid of five (5) points obtained by using the hybrid coefficients is given by the graph at the left hand side of Figure 5.7. The relative error across the domain is given by the graph at the right hand side of Figure 5.7.

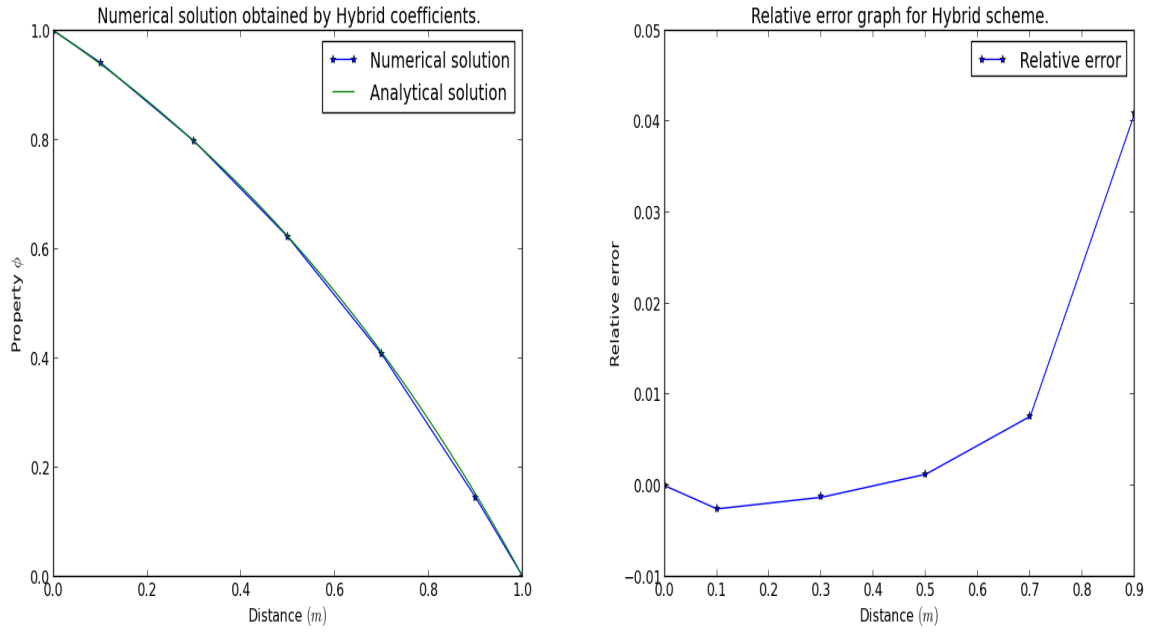

Figure 5.7: Comparing analytical solution 5.1.1 with hybrid solution for a course grid.

It can be observed from Figure 5.7 that even for a course grid of five (5) points, the hybrid scheme gives a good approximation of the analytical solution 5.1.1.

Effects of grid size (number of grid points) on convergence is also investigated, the graph at the left hand side of Figure 5.8 shows a comparison of the analytical solution with the hybrid solution obtained by using 15 grid points. Figure 5.8 shows a comparison of the analytical solution 5.1.1 and the hybrid solution obtained by using 25 grid points.

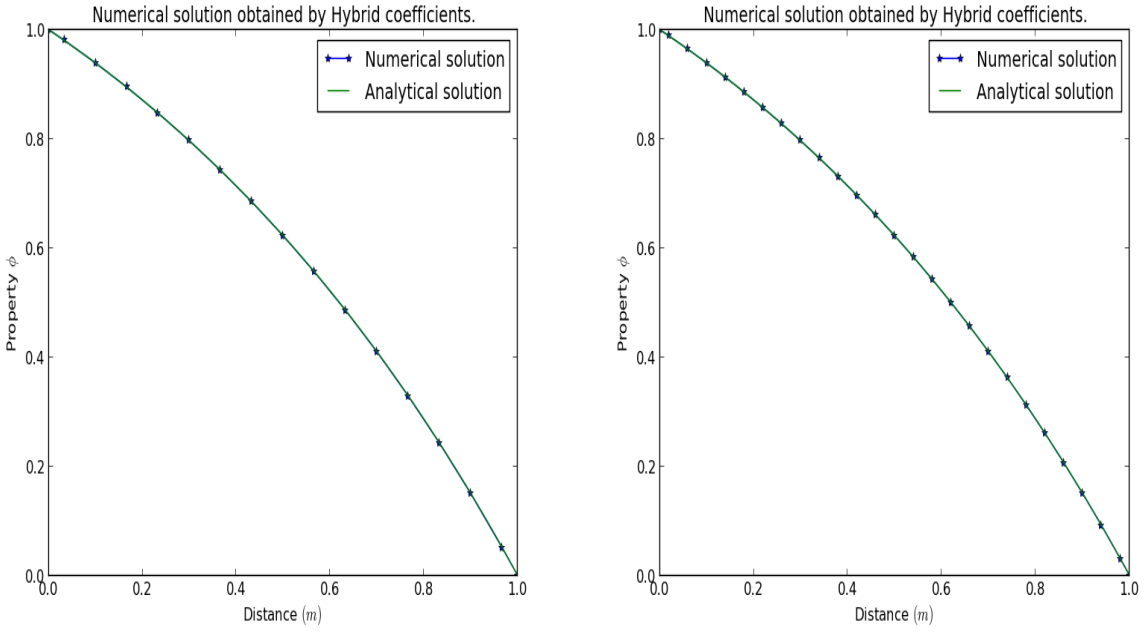

Figure 5.8: Comparing the analytical solution 5.1.1 with hybrid solutions for finer grids.

From the graphs given by Figure 5.8, it can be qualitatively concluded the hybrid solution converges to the exact solution as the grid becomes finer (implying smaller step sizes or more grid points). Thus if more accuracy is desired in numerical simulations, finer grids should be used.

Furthermore, effects of a high Peclet number is also investigated on the hybrid scheme. Figure 5.9 shows a comparison of the analytical solution and the hybrid solution for a Peclet number of 5.

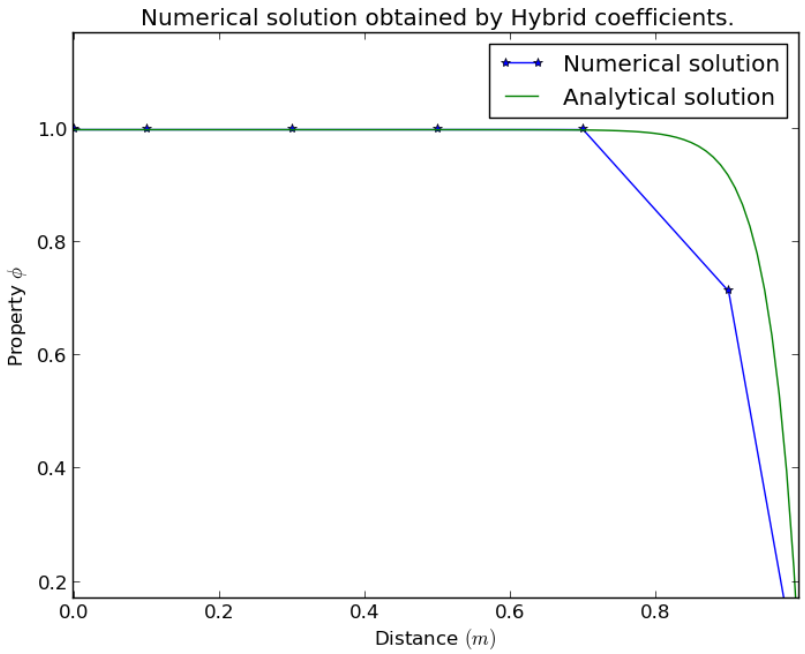

Figure 5.9: Comparing hybrid solution and analytical solution for a high Peclet number.

The results in Figure 5.9 do not contain oscillations because the hybrid scheme satisfies the transportiveness property. The hybrid scheme is more efficient in high Peclet number cases as compared with the central differencing scheme. The results suggest that the hybrid scheme is reliable for high Peclet number problems.

To compare the performance of the spatial discretization schemes, we compare the effects of grid size on convergence for the three schemes. Figure 5.10 shows the results for the comparison.

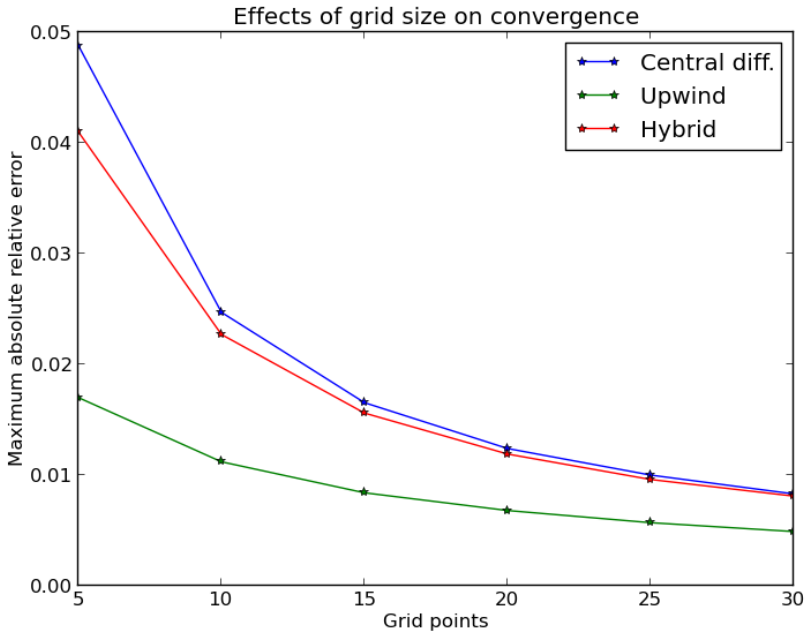

Figure 5.10: Convergence rate of the upwind, central differencing and hybrid solutions.

The results in Figure 5.10 show that the upwind scheme has minimal errors for the test case. It can also be observed that, all the schemes converge as the number of grid points increases. However, the central differencing solution converges faster, followed by the hybrid.

5.1.4 Accuracy and stability test for the explicit scheme

The explicit solution for the time-dependent problem is given by the graph at the left hand side of Figure 5.11. The relative error across the domain is given by the graph at the right hand of Figure 5.11.

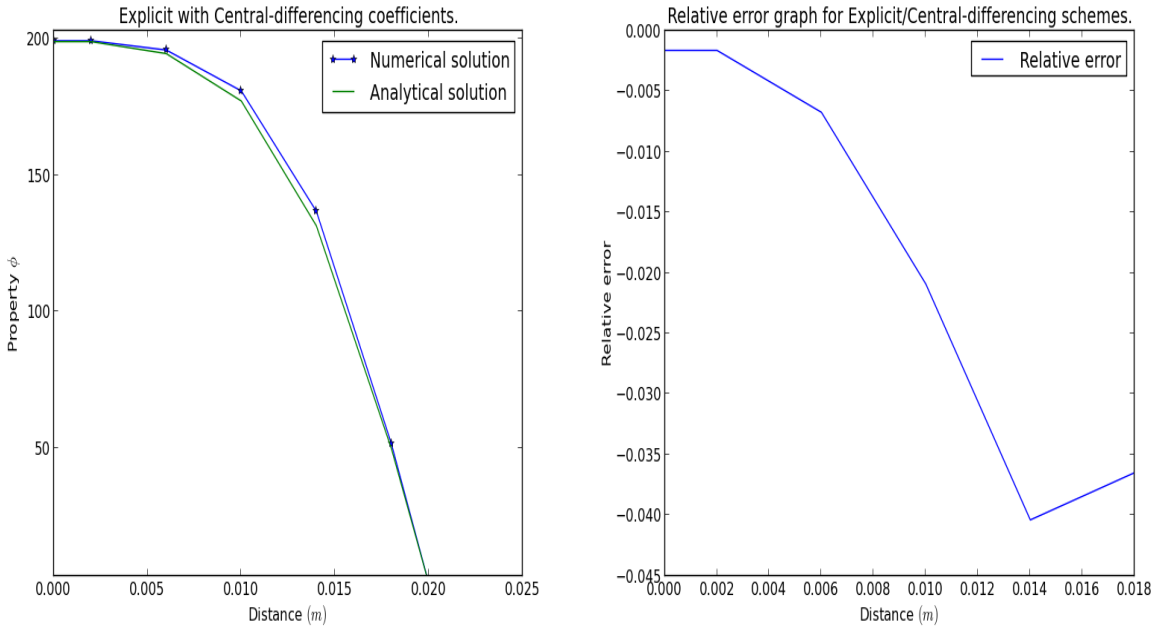

Figure 5.11: Comparing analytical solution 5.1.2 with the explicit solution for a course grid of five points and time step size of 2 s.

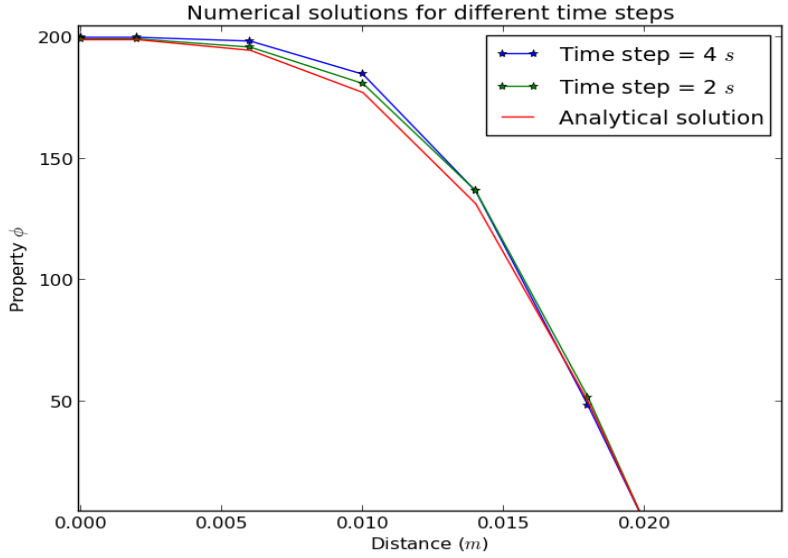

Figure 5.12: Comparing the analytical solution 5.1.2 with the explicit solution for a course grids and for different time steps .

It can be observed from Figure 5.11 that the explicit scheme gives a good approximation of the analytical solution 5.1.2 for a course grid of five (5) points.

Effects of time step size on convergence of the solution is investigated, Figure 5.12 shows a comparison of the analytical solution with the explicit solution for two time step sizes.

The graph with the smaller time step size in Figure 5.12 gives a better approximation of the analytical solution. Thus using smaller time step sizes will improve the accuracy of the explicit scheme. However, for time-dependent convection-diffusion problems, the accuracy of the numerical solution also depends on grid size. Smoothness of the numerical solution is determined by the grid size as shown by the graph on the left hand side of Figure 5.13 and fitness of the numerical solution with the analytical solution is determined by time step size as shown by the graph at the right hand side of Figure 5.13.

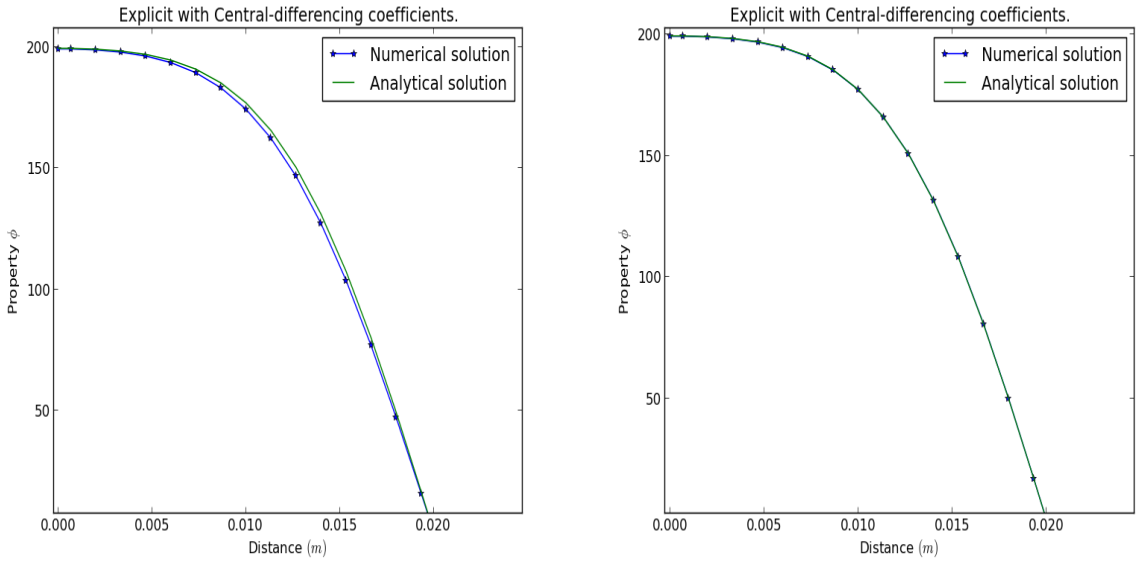

Figure 5.13: Comparing the analytical solution 5.1.2 with the explicit solution for a fine grid (15 points) and for different time step sizes (0.2 s for the left graph and 0.002 s for the right graph).

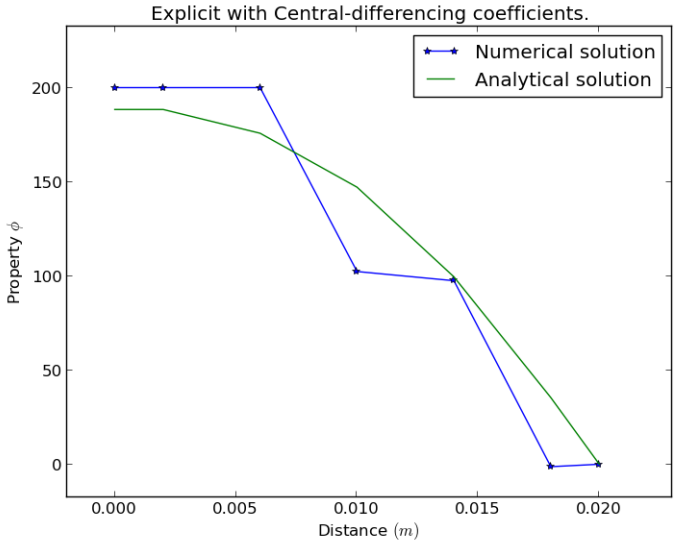

Figure 5.14: Comparing the explicit solution with analytical solution for a time step size of 10 s.

From the results given by Figures 5.13, it can be qualitatively concluded that the accuracy of the explicit solution improves when the time step size is small and a fine grid is used.

The stability of the explicit scheme is investigated by setting the time step to 10 s. The results are given in Figure 5.14.

The results in Figure 5.14 confirm that the explicit scheme is conditionally stable, thus not reliable.

5.1.5 Accuracy and stability test for the fully implicit scheme

The implicit solution for the time-dependent problem is given by the graph at the right hand side of Figure 5.15. The corresponding relative error across the domain is given by the right hand side graph of Figure 5.15.

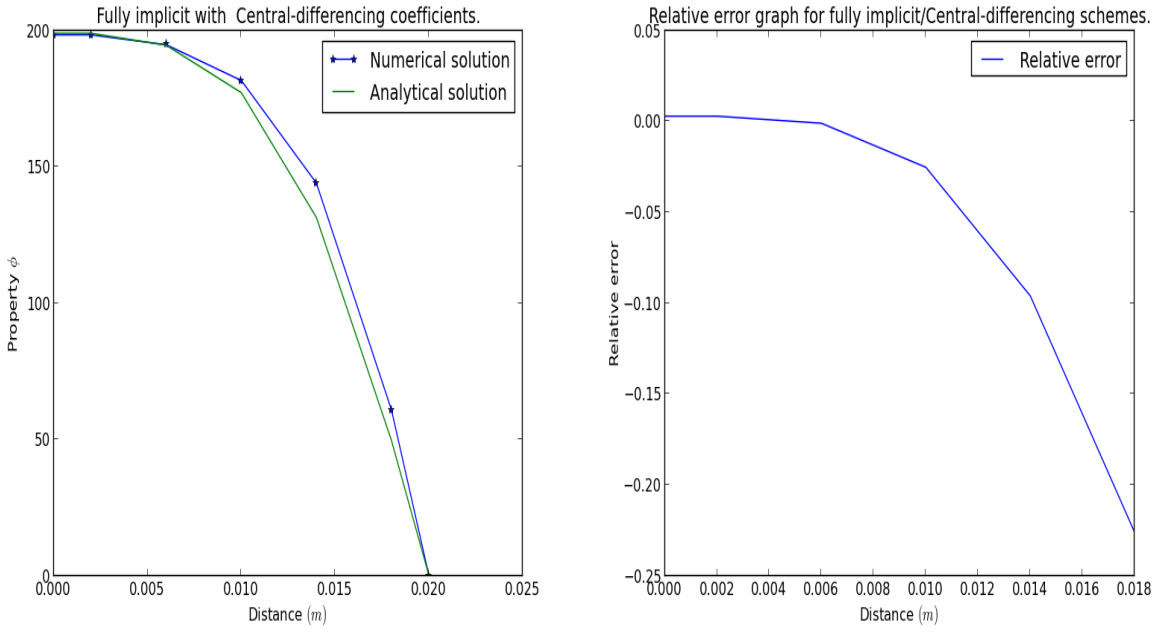

Figure 5.15: Comparing analytical solution 5.1.2 with the implicit solution for a course grid of five points and time step size of 2 s.

It can observed in Figure 5.15 that, the implicit scheme gives a good approximation of the analytical solution 5.1.2 even for a course grid of five (5) points.

Effects of time step size on convergence of the solution is investigated, Figure 5.16 shows a comparison of the analytical solution with the implicit solution for two time step sizes.

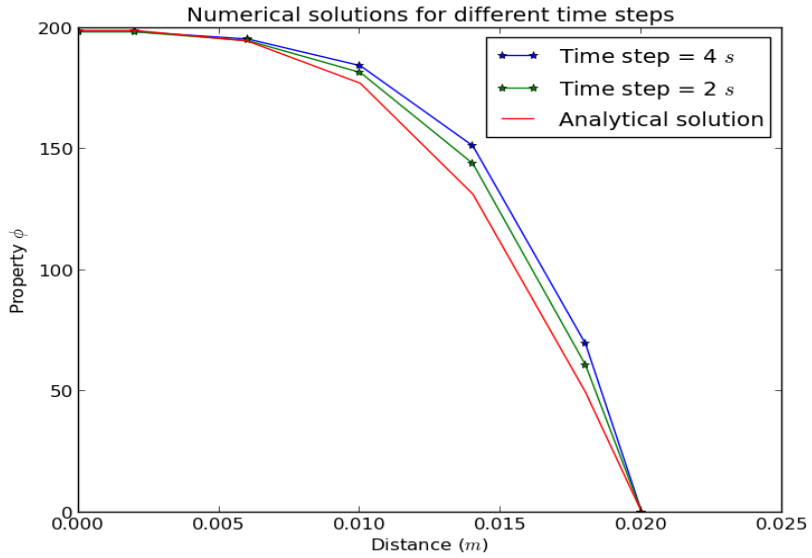

Figure 5.16: Comparing the analytical solution 5.1.2 with the implicit solution for a course grids and for different time steps .

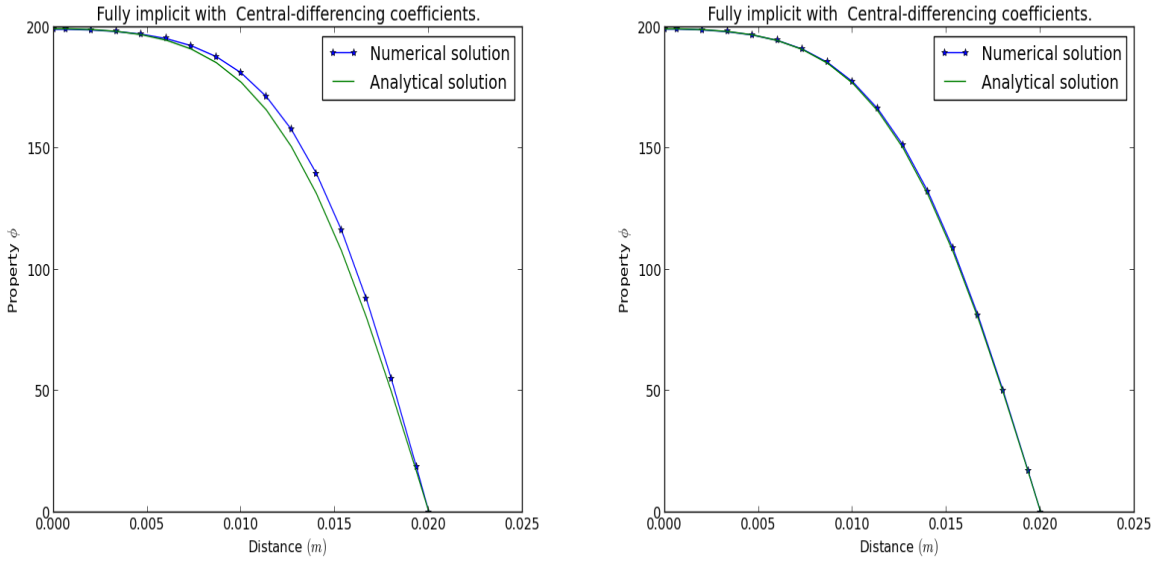

Figure 5.17: Comparing the analytical solution 5.1.2 with the implicit solutions for a fine grid (15 points), and different time step sizes (time steps $= 2, 0.2$ for left and right graphs respectively).

The graph with the smaller time step size in Figure 5.16 gives a better approximation of the analytical solution. Thus using smaller time step sizes will improve the accuracy of the implicit scheme. Since the accuracy of a time-dependent convection-diffusion problems also depends on grid size, we used a fine grid to investigate the effect of grid size on convergence. The numerical solution becomes smoother (as shown the graph at the left hand side of Figure 5.17) compared with a course grid. Overall convergence of the numerical solution is a combined effect of the grid size and the time step-size as shown by the graph at the right hand side of Figure 5.17.

The stability of the implicit scheme is investigated by setting the time step to 10 s. The results are given by Figure 5.18.

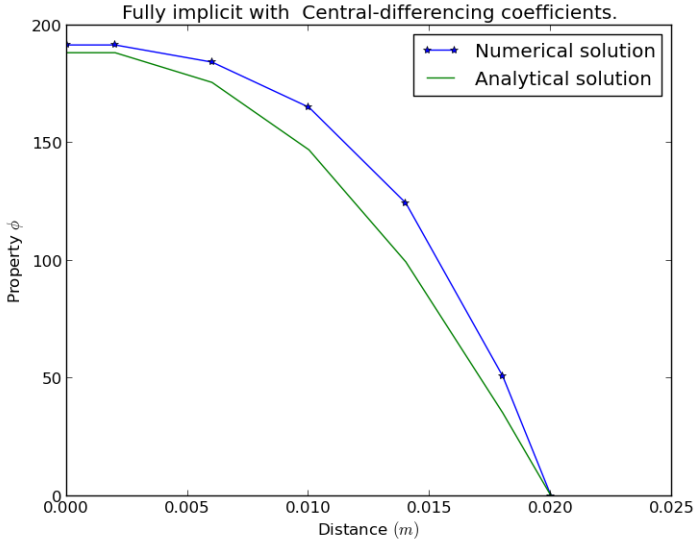

Figure 5.18: Comparing implicit solution with analytical solution for a large time step size (10 s).

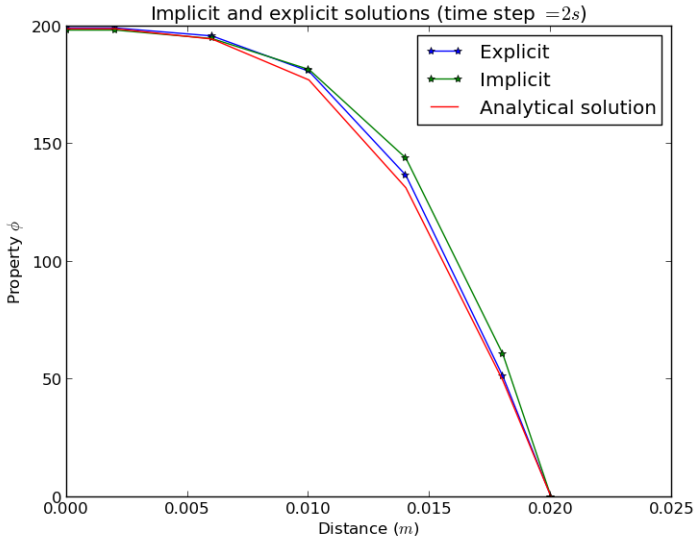

Figure 5.19: Comparison of the explicit, implicit and analytical solutions for time step size of 2 s.

Although the solution given by Figure 5.18 is not very accurate, it does not contain oscillations. Thus the implicit scheme is reliable. We investigated the performance of the explicit and implicit schemes for the same time step (2 s) and grid size (0.004 m). Figure 5.19 shows the results of the investigation.

The results show that the explicit scheme performs better than the implicit scheme for the given problem and test data. All the validated numerical schemes will be applied to obtain solutions to the model derived in Chapter 3.

5.2 Validation of computer code

In this section, we investigate the validity of our computer code that is used for the numerical experiments. Three test cases are used, these include a rotating body problem, transportation of a pulse and an oblique inflow convection-diffusion-reaction problem.

5.2.1 Rotation of bodies

The rotating-body problem is a pure-convective transport problem. The rotating bodies deteriorate with time as the rotation occurs. However if a fine grid is used, the deterioration minimizes and shapes of the bodies do not change significantly. The data for this test case is taken from [56]. Figure 5.20 shows the initial condition and exact solution for this test case.

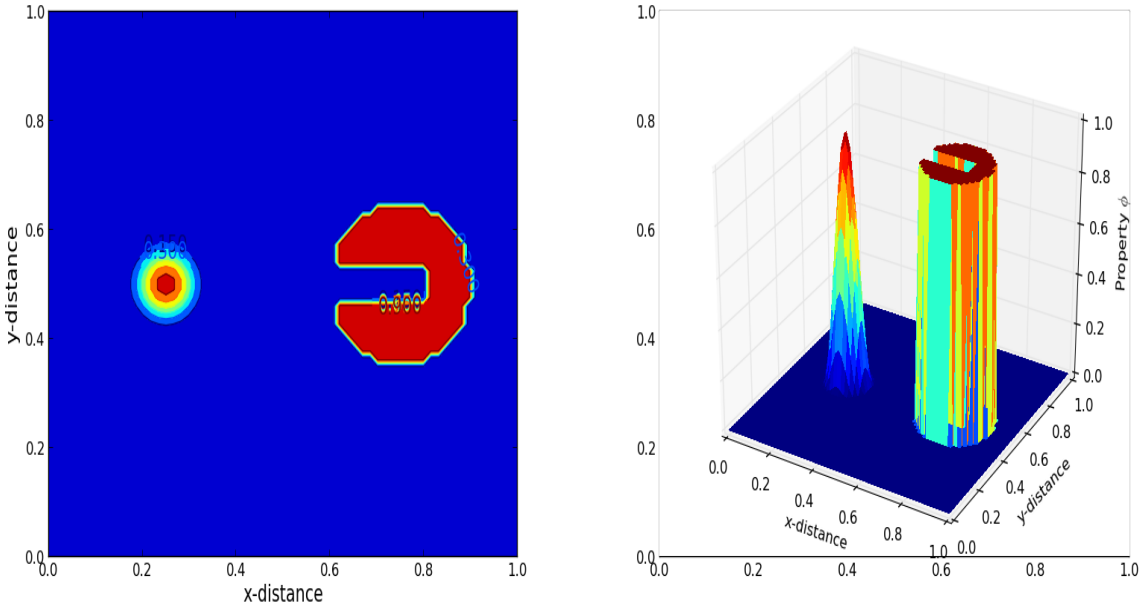

Figure 5.20: Initial condition and exact solution for the rotating-body problem.

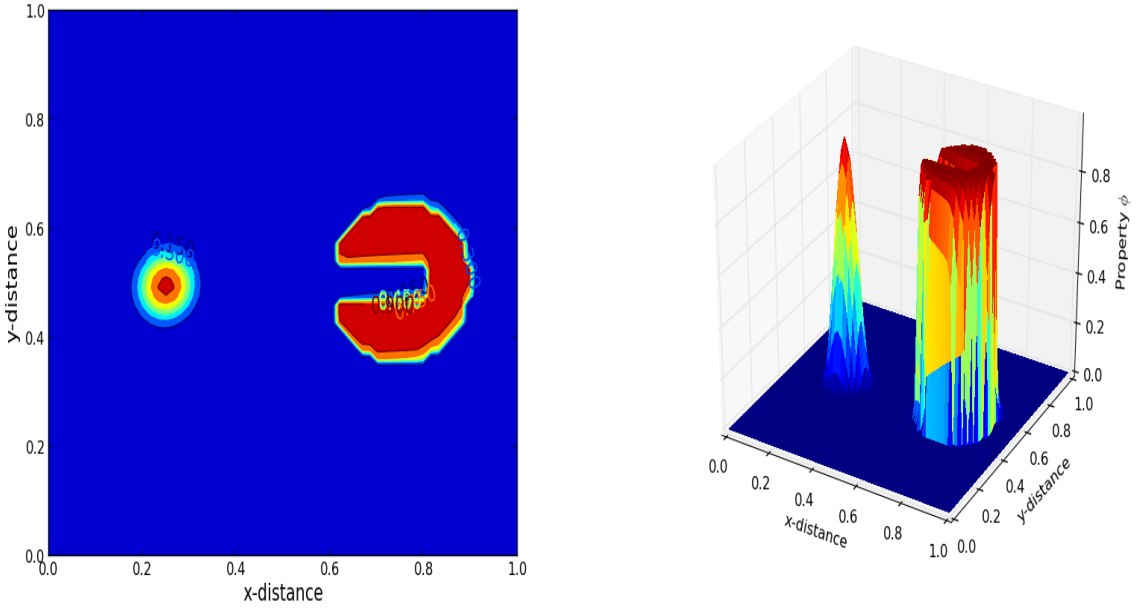

Figure 5.21: Shapes of the cylinder and cone after one cycle.

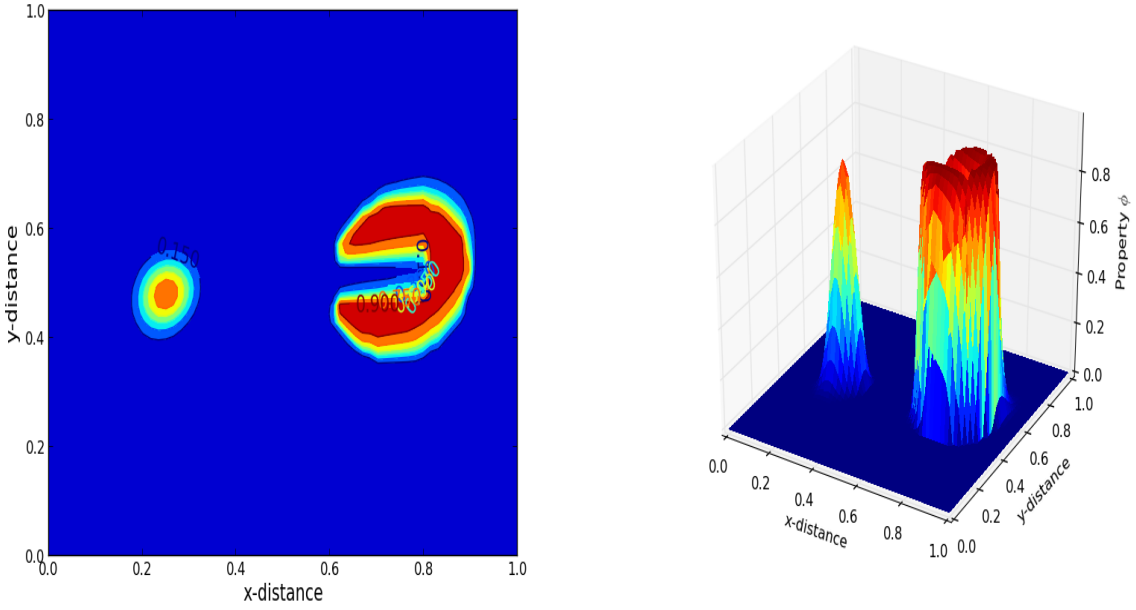

Figure 5.22: Shapes of the cylinder and cone after four cycles.

5.2.2 Transportation of a pulse

Transportation of a pulse involves advection and diffusion. The pulse flattens-out with time, while moving across the domain. The data for this test case is taken from [56]. Figure 5.23 shows the initial condition for this test case.

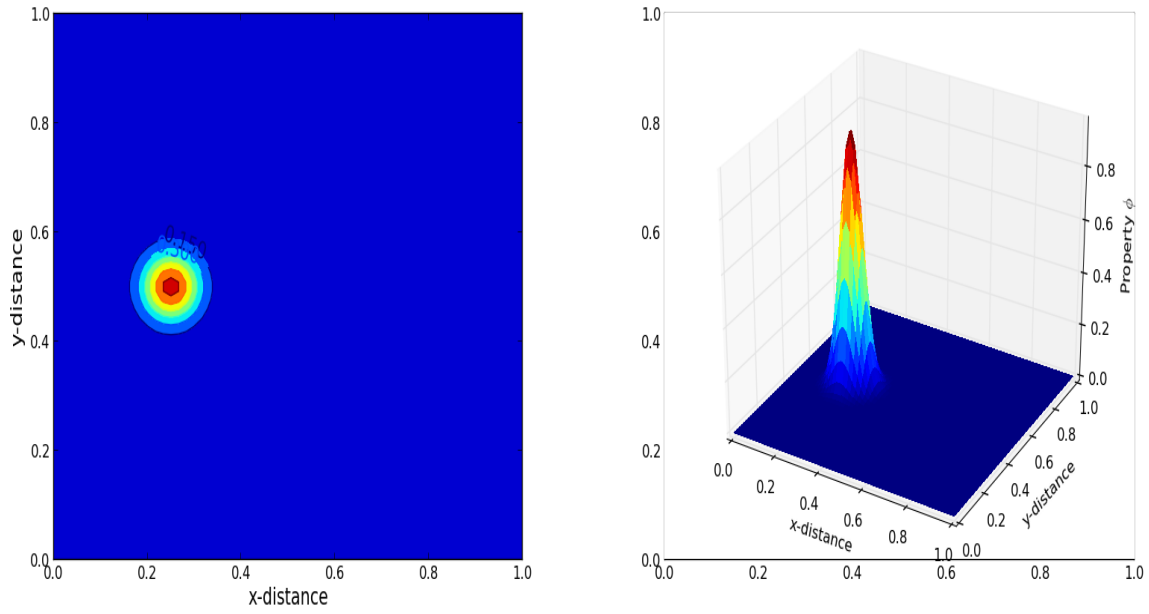

Figure 5.23: Initial condition and exact solution for the rotating-body problem.

Since this problem is not a high Peclet number problem, we couple each spatial scheme with implicit or explicit time discretization schemes. The results obtained by coupling all the spatial scheme with the time schemes are given by Figures 5.24 and 5.25 for a grid size of $\frac{1}{64} \times \frac{1}{64}$.

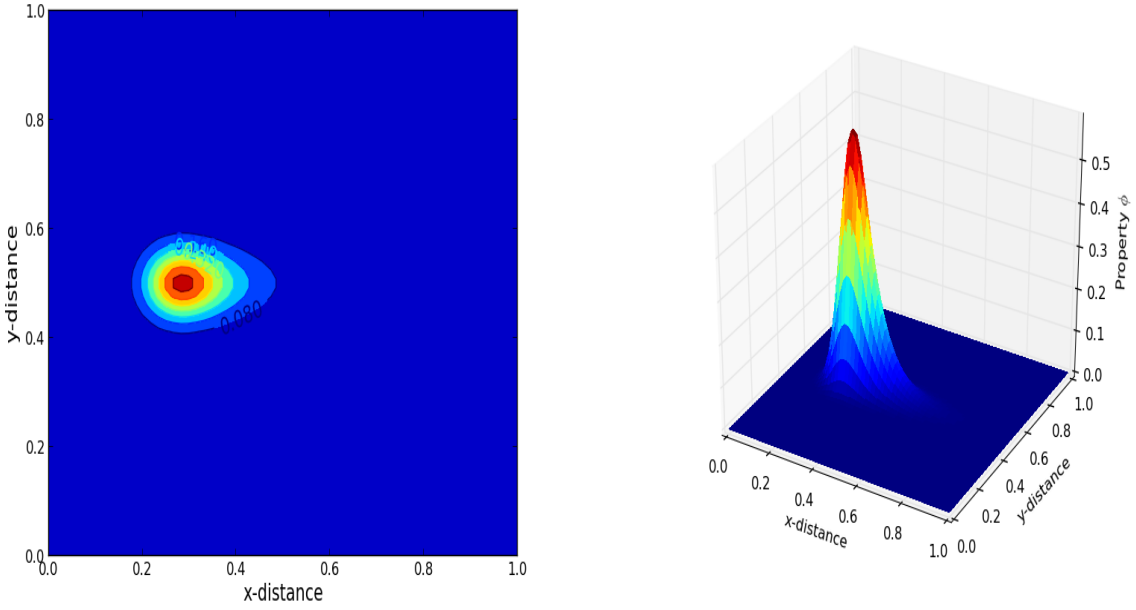

Figure 5.24: Shape of the pulse after 0.25 s.

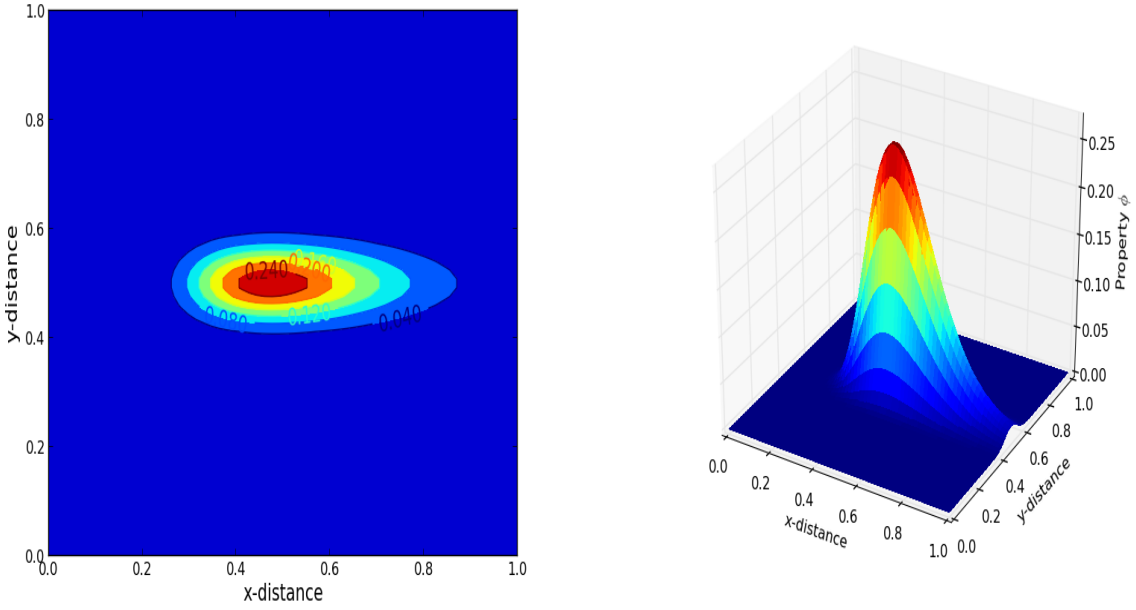

Figure 5.25: Shape of the pulse after 1 s.

5.2.3 Oblique inflow convection-diffusion-reaction problem

The oblique inflow convection-diffusion-reaction problem is a transport equation with a linear source term. The initial condition used in this test case is zero. Figure 5.26 shows the initial condition for the oblique inflow case. Figure 5.27 shows the distribution of ϕ in the domain after 0.5 s, and Figure 5.28 shows the distribution of ϕ after $t = 1$ s.

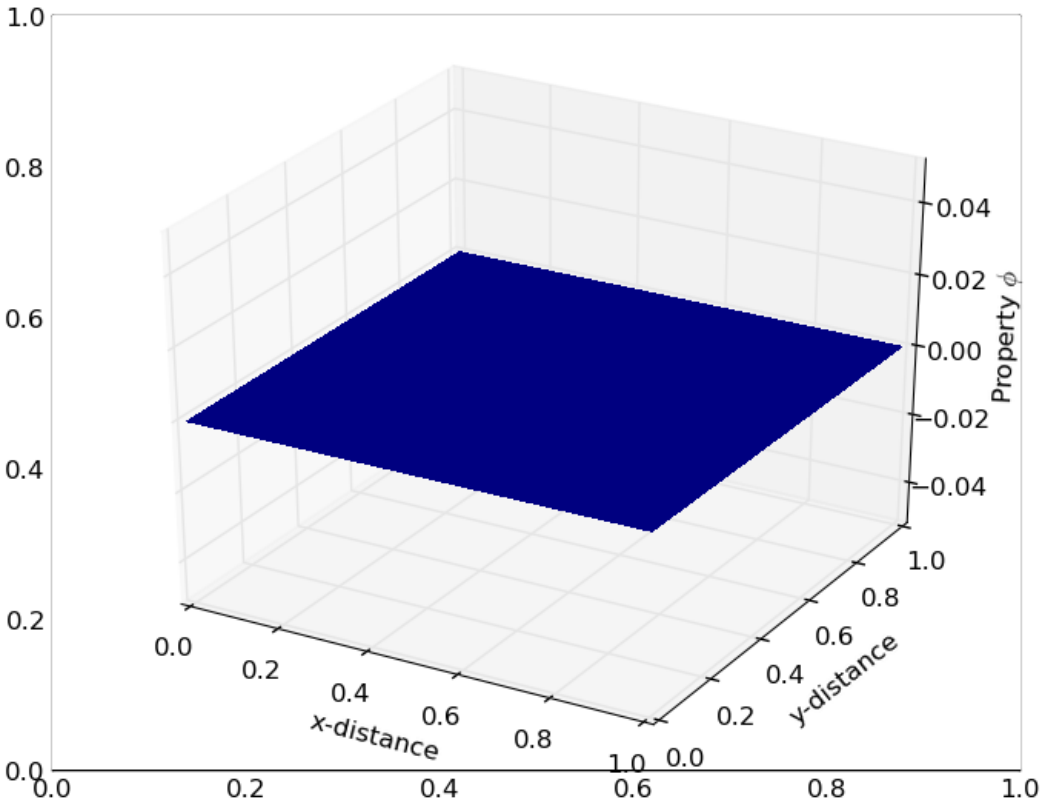

Figure 5.26: Initial condition for the convection-diffusion-reaction problem.

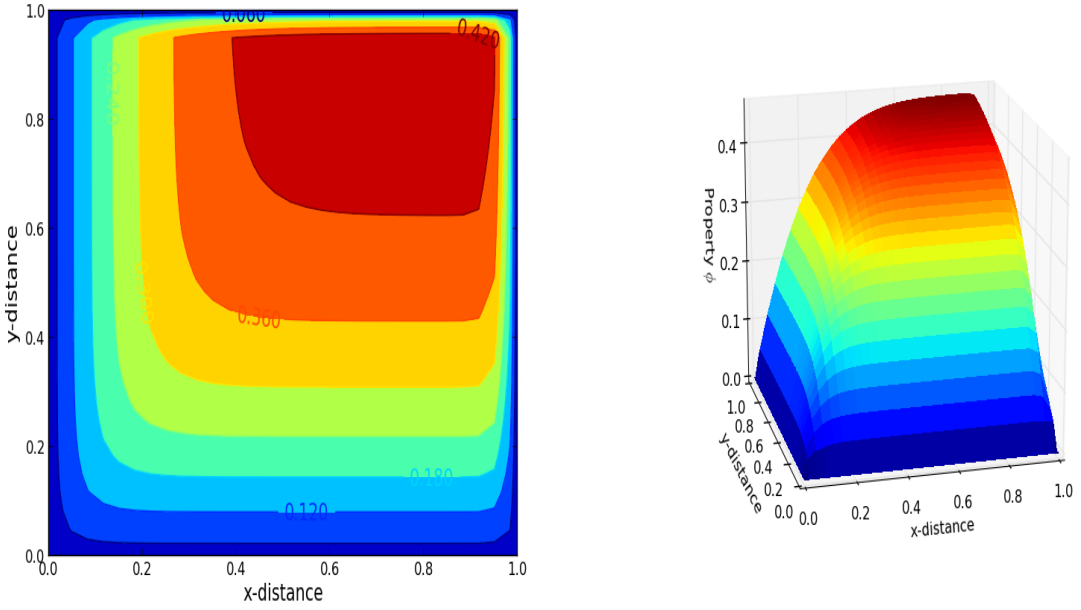

Figure 5.27: ϕ distribution after 0.5 s

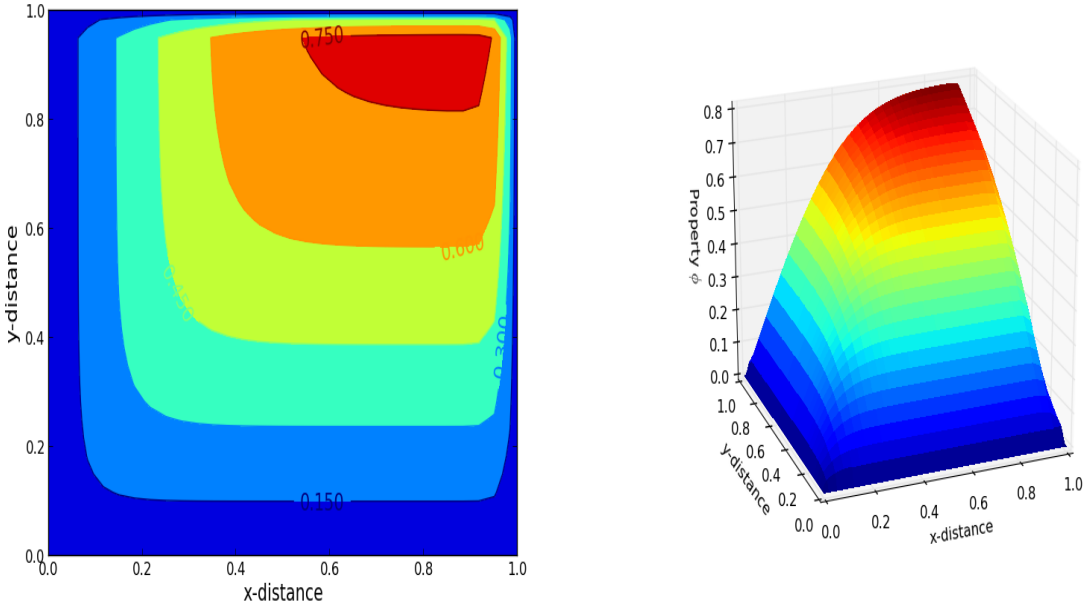

Figure 5.28: ϕ distribution after 1 s

All the results obtained in this section are similar to those obtained in [56]. Thus we have confidence that our numerical code is valid for our experiments.

The parameters used to obtain results in this section are given in Appendix B. A uniform flow profile is coupled with the species and energy transport equations. All boundaries were set to zero except the southern boundary, which was set to 80 ^oC.

The initial concentrations of the species are 0.01 g/m^3 of hydrogen ions, 10^{-13} g/m^3 of ferric ions, 10^{-3} g/m^3 of ferrous ions, 0.02 g/m^3 of iron hydroxide, 10^{-3} g/m^3 of sulfate, 10^{-7} g/m^3 of calcium ions, 0.002 g/m^3 of oxygen, 10^{-13} g/m^3 of hydro-carbonate ions, and 80 ^oC for temperature. The initial concentrations are distributed uniformly throughout the domain as shown in Figure 5.29.

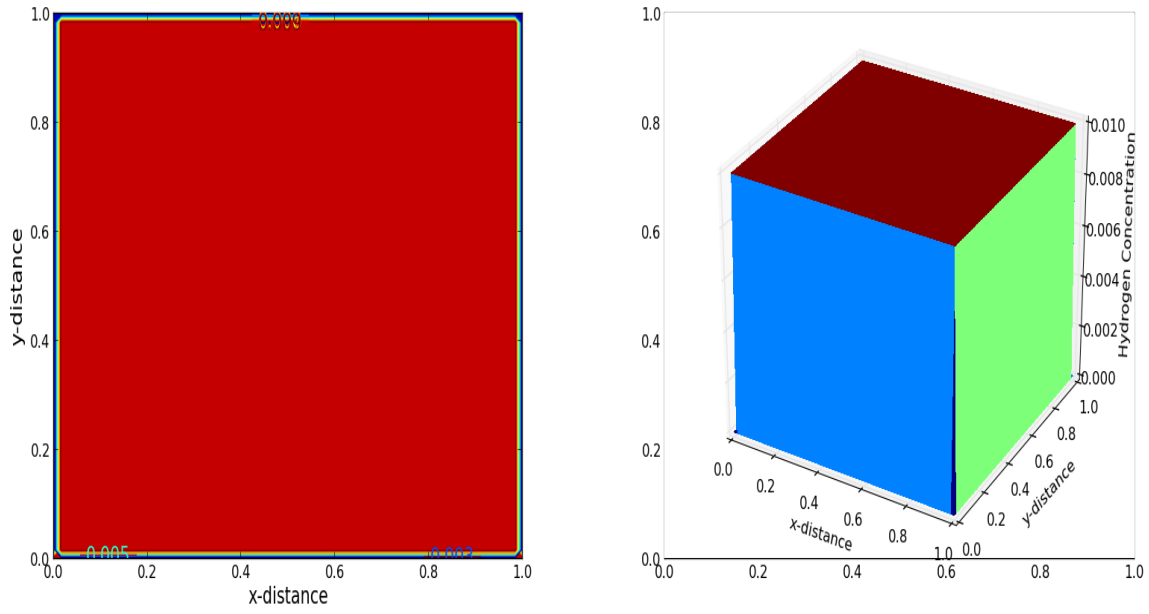

Figure 5.29: Initial hydrogen ion distribution.

In this section, we present results of our numerical experiments. The investigations that are carried out include effects of dispersion and convection on chemical species and temperature distributions, and the changes in concentration of species with time. All appropriate numerical schemes that were discussed earlier were applied in each investigation

and the results showed no significant differences. Thus we do not specify the schemes used to obtain the results.

5.2.4 Effects of equal convection and dispersion

The magnitudes of the velocity and dispersion coefficient were set equal to 10^{-2}, and the grid cell size was set to $\frac{1}{25} \times \frac{1}{25}$. The distributions of chemical species and temperature after 2 min, using a time-step size of 0.1 are given by Figures 5.30 to Figure 5.38.

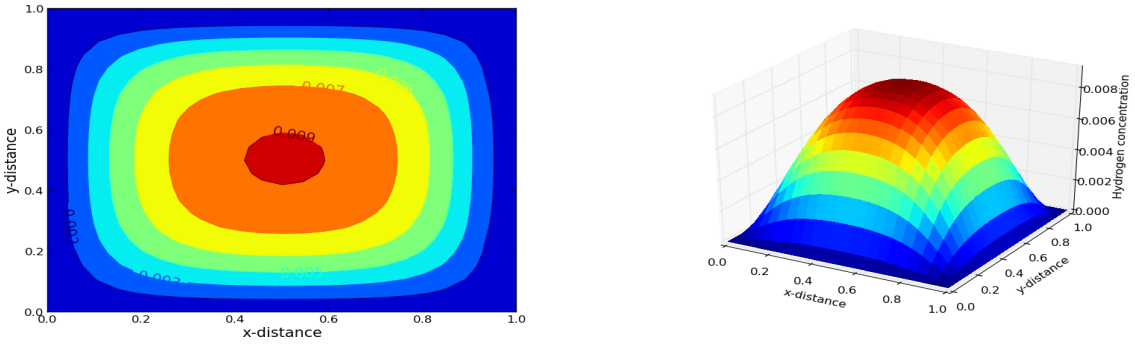

Figure 5.30: Hydrogen ion distribution, velocity 10^{-2} m/min.

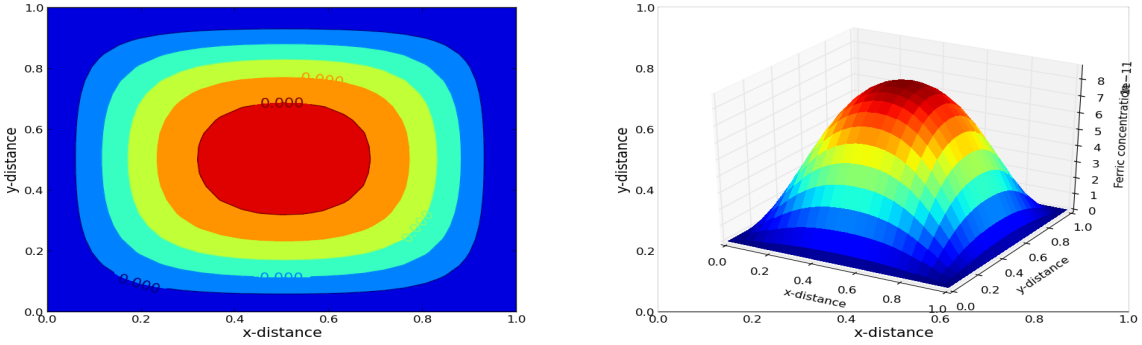

Figure 5.31: Ferric ion distribution, velocity 10^{-2} m/min.

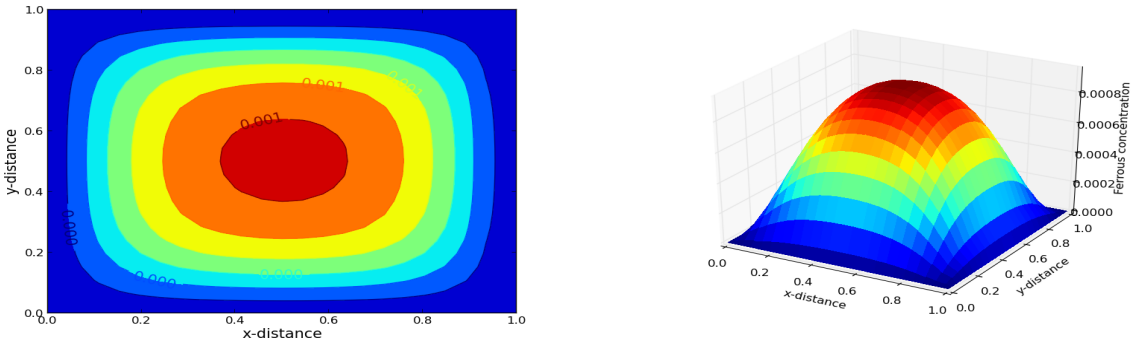

Figure 5.32: Ferrous ion distribution, velocity 10^{-2} m/min.

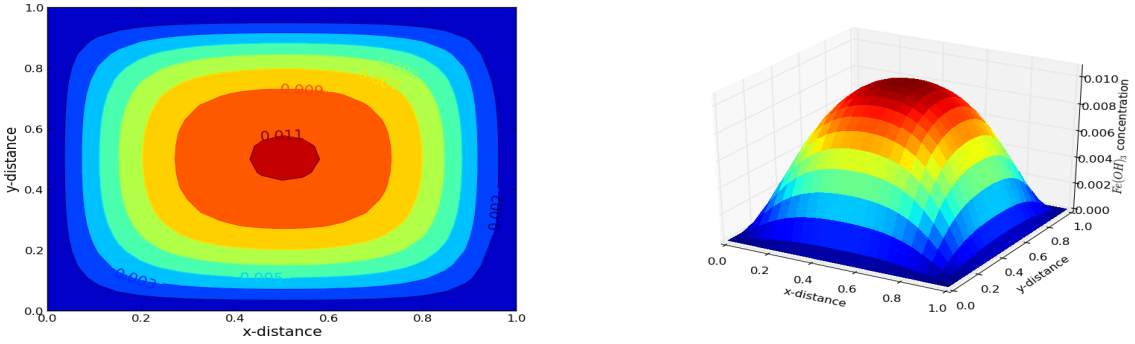

Figure 5.33: Iron hydroxide distribution, velocity 10^{-2} m/min.

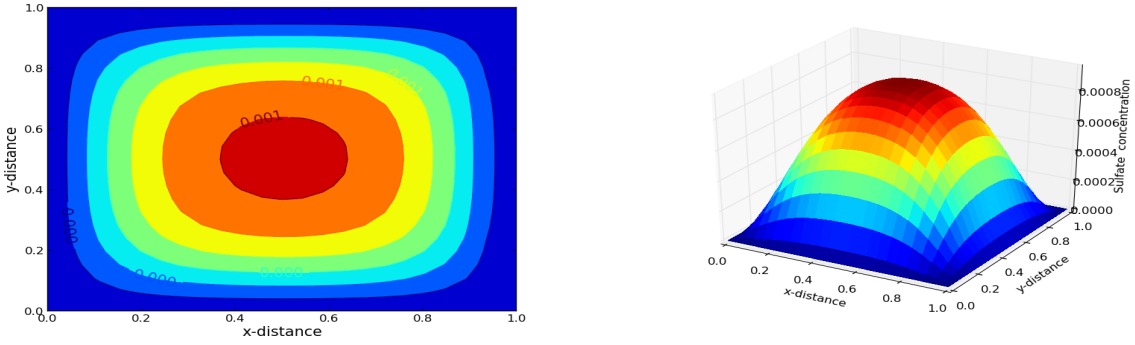

Figure 5.34: Sulfate distribution, velocity 10^{-2} m/min.

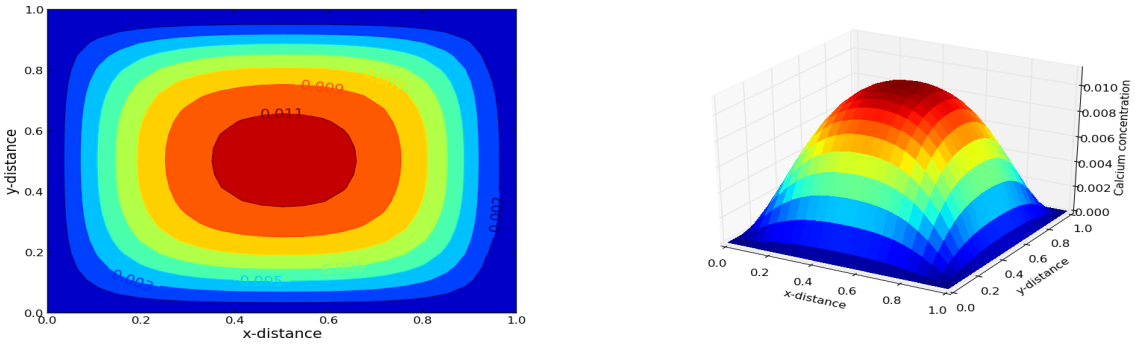

Figure 5.35: Calcium distribution, velocity 10^{-2} m/min.

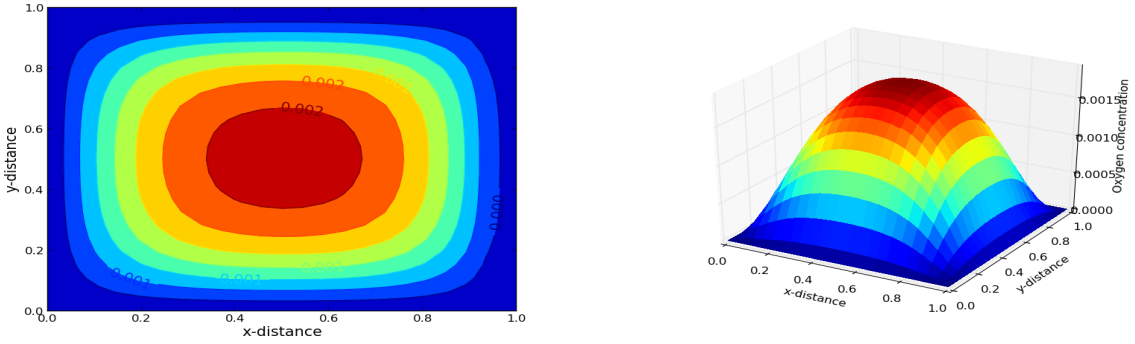

Figure 5.36: Oxygen distribution, velocity 10^{-2} m/min.

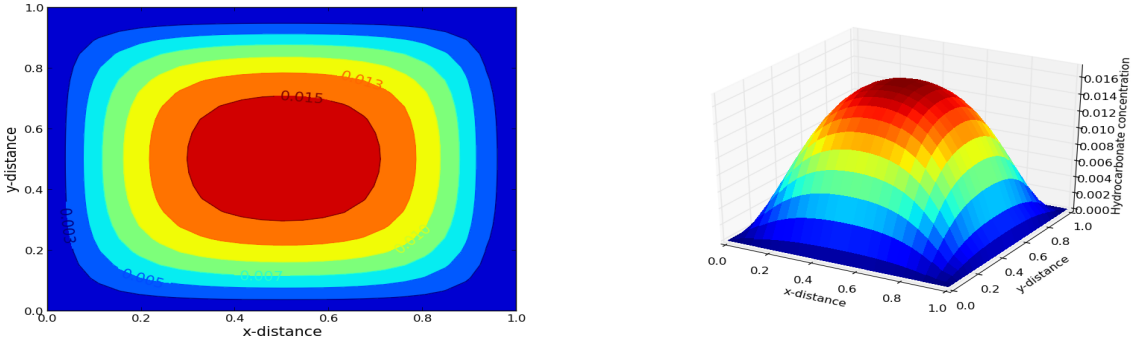

Figure 5.37: Hydro-carbonate distribution, velocity 10^{-2} m/min.

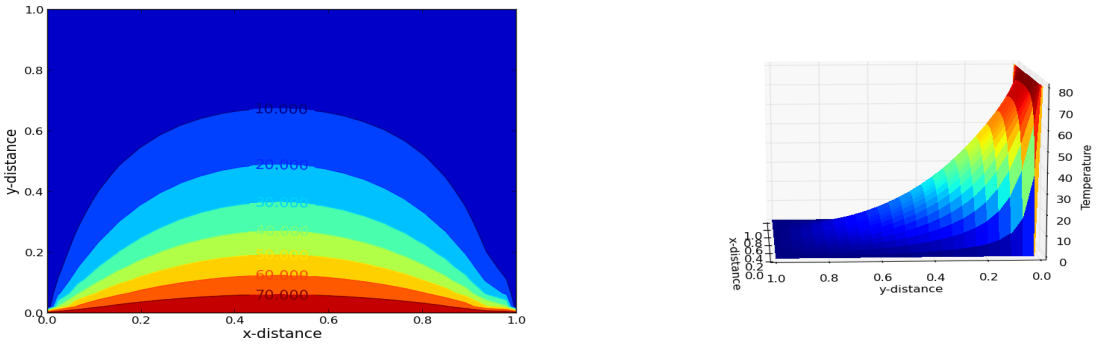

Figure 5.38: Temperature distribution, velocity 10^{-2} m/min.

From Figures 5.30 to 5.37, it can be observed that the initial uniform species distributions have been transformed into Gaussian distributions. However, Figure 5.38 shows a different profile because of the imposed non-zero constant boundary. Thus equal convection and dispersion will transform a uniform distribution into a normal (Gaussian) distribution when all boundaries are zero. The difference between the chemical species profiles is the heights and area covered by the remaining unreacted, unfiltered and undispersed species (indicated by red). The changes in heights is attributed to reaction, production and filtration of the species.

Further, we investigated the effects of different magnitudes of equal convection and dispersion on the species distribution. Figures 5.39 to 5.47 show the distributions of chemical species and temperature after 20 min, using a time-step size of 2. The magnitudes of the velocity and dispersion coefficient are equal to 10^{-4}, and the grid cell size is $\frac{1}{25} \times \frac{1}{25}$.

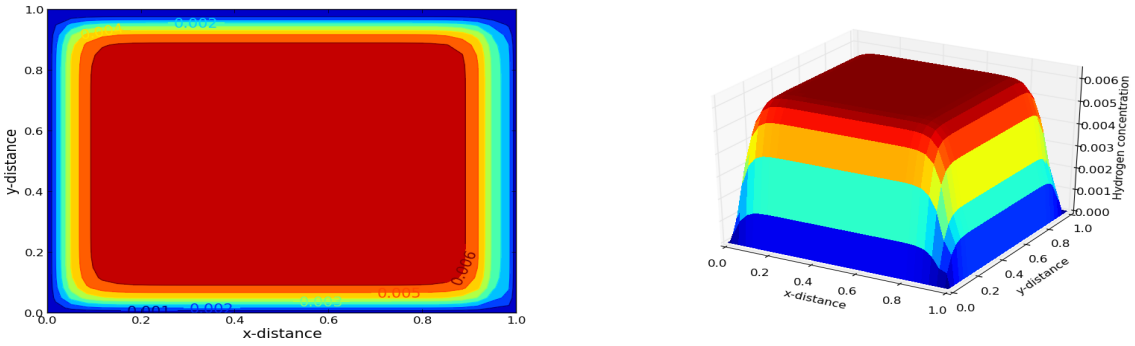

Figure 5.39: Hydrogen ion distribution, velocity 10^{-4} m/min.

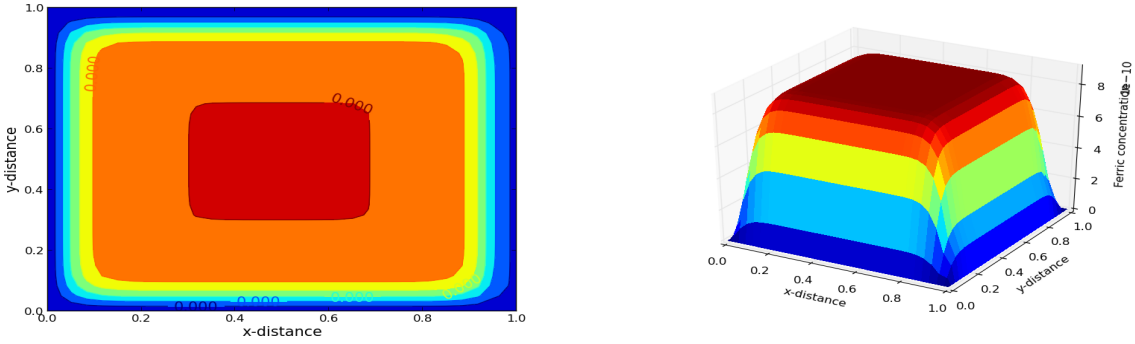

Figure 5.40: Ferric ion distribution, velocity 10^{-4} m/min.

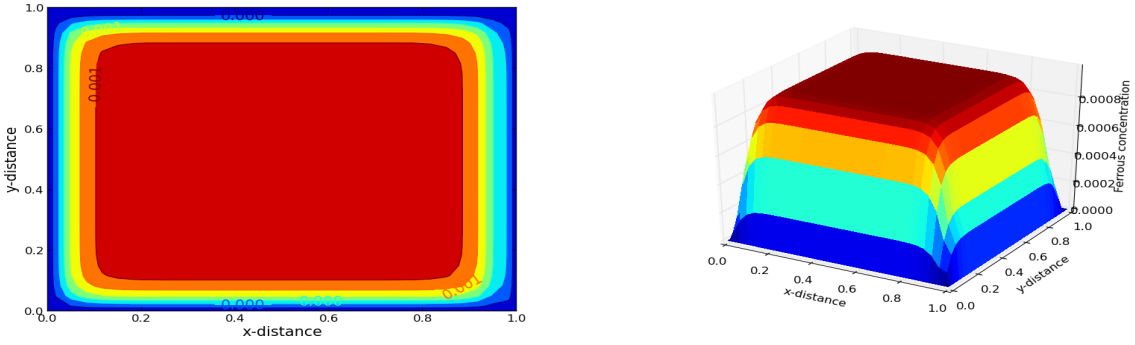

Figure 5.41: Ferrous ion distribution, velocity 10^{-4} m/min.

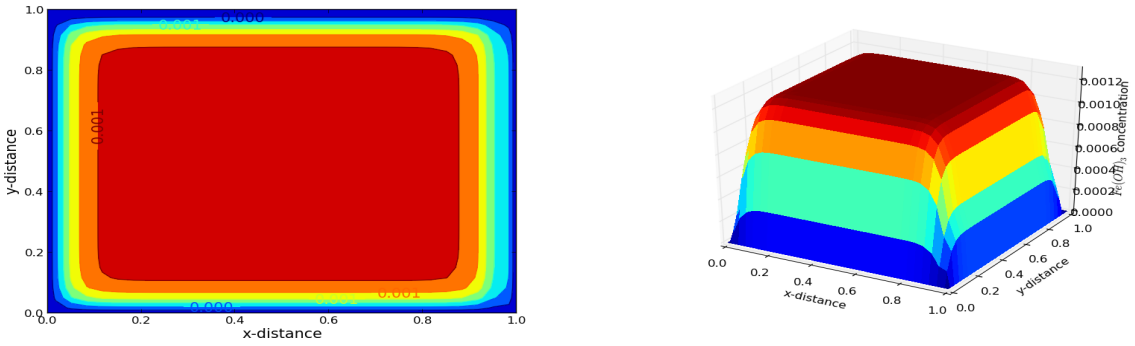

Figure 5.42: Iron hydroxide distribution, velocity 10^{-4} m/min.

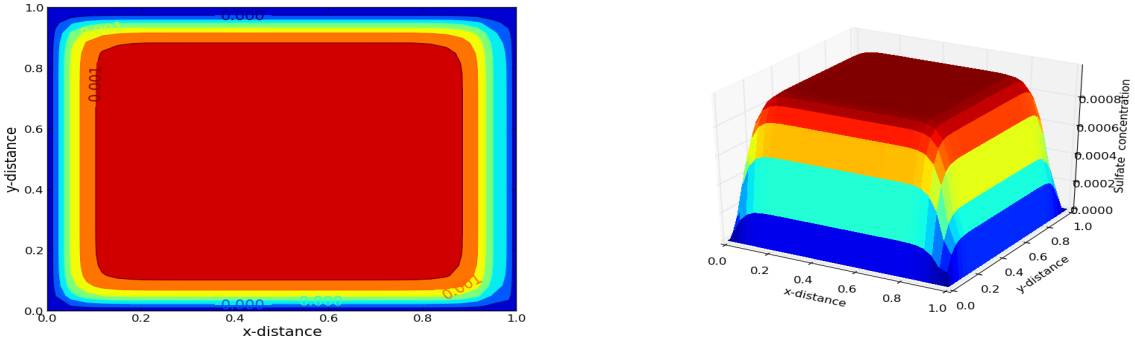

Figure 5.43: Sulfate distribution, velocity 10^{-4} m/min.

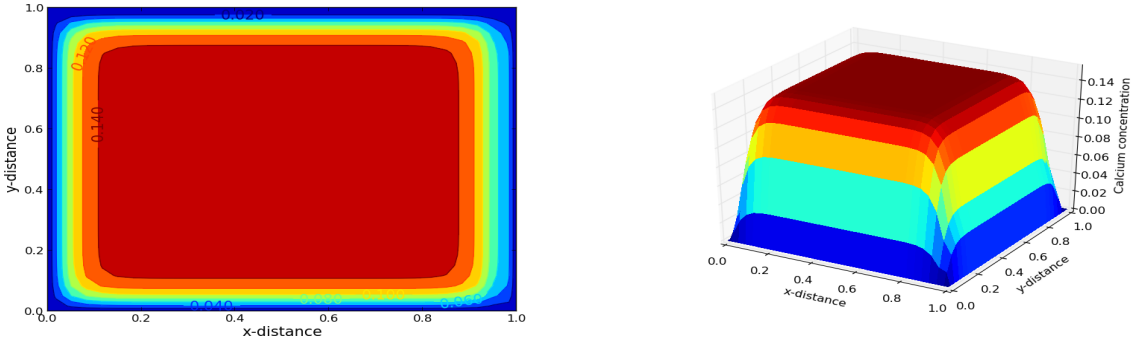

Figure 5.44: Calcium distribution, velocity 10^{-4} m/min.

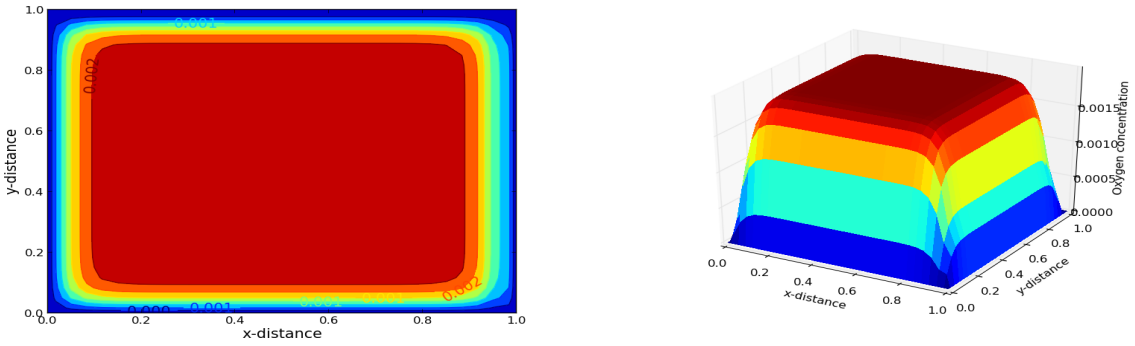

Figure 5.45: Oxygen distribution, velocity 10^{-4} m/min.

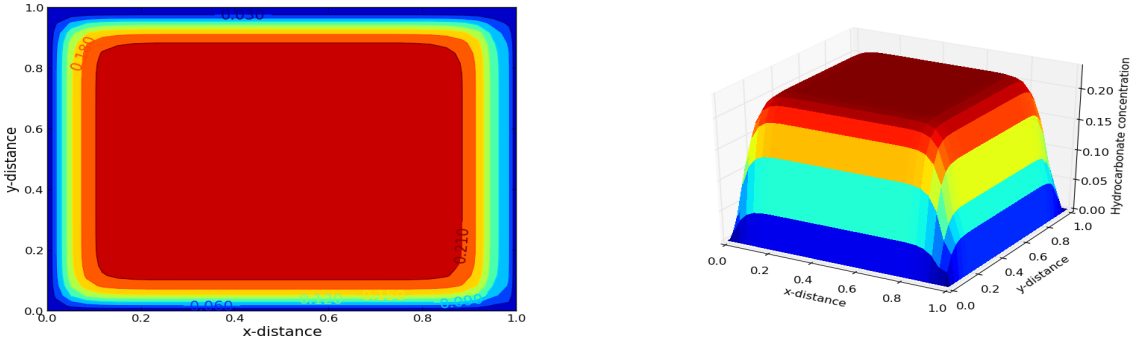

Figure 5.46: Hydro-carbonate distribution, velocity 10^{-4} m/min.

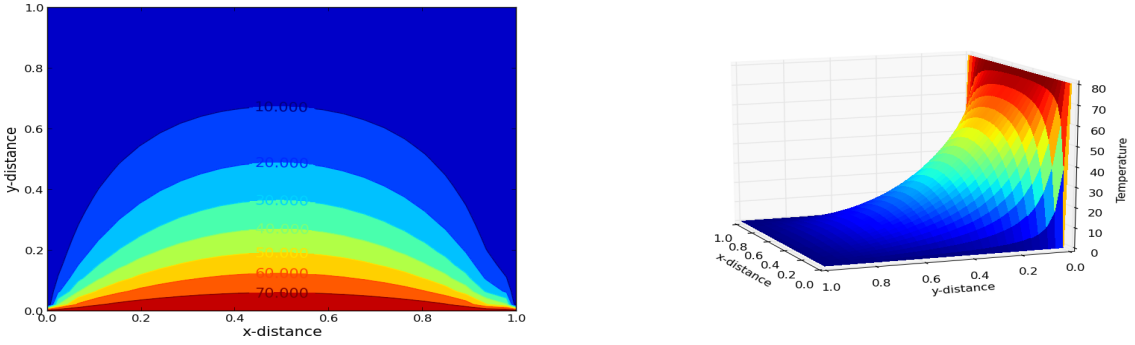

Figure 5.47: Temperature distribution, velocity 10^{-4} m/min.

From Figures 5.39 to 5.47, it can be observed that a larger part of the domain remains uniform even after twenty (20) minutes. Thus the rate at which the uniform distribution transforms into a Gaussian depends on the magnitude of convection and dispersion.

In this section, we present results for a case where convection is greater than dispersion. The velocity was set to $10^{-2}m/min$, dispersion coefficient set to $10^{-4}m^2/min$, and the reaction constants maintained. The distributions of chemical species after 2 min, using a time-step size of 0.1 and a grid cell size of $\frac{1}{25} \times \frac{1}{25}$, are given by Figures 5.48 to 5.55.

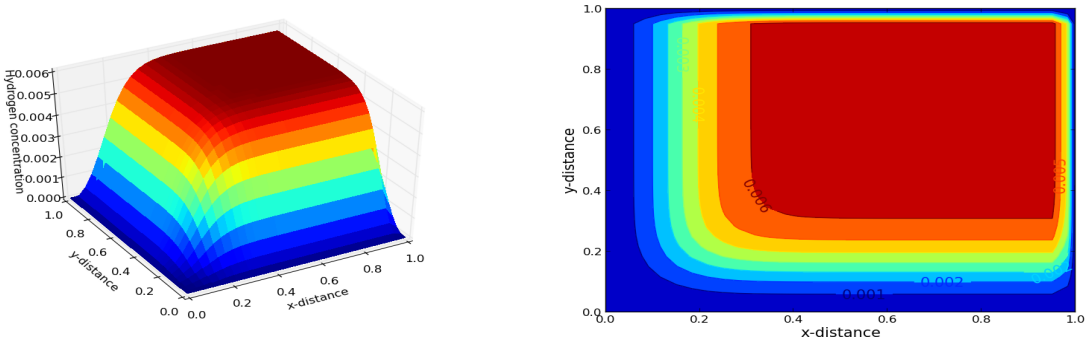

Figure 5.48: Hydrogen ion distribution, convection-dominated transport.

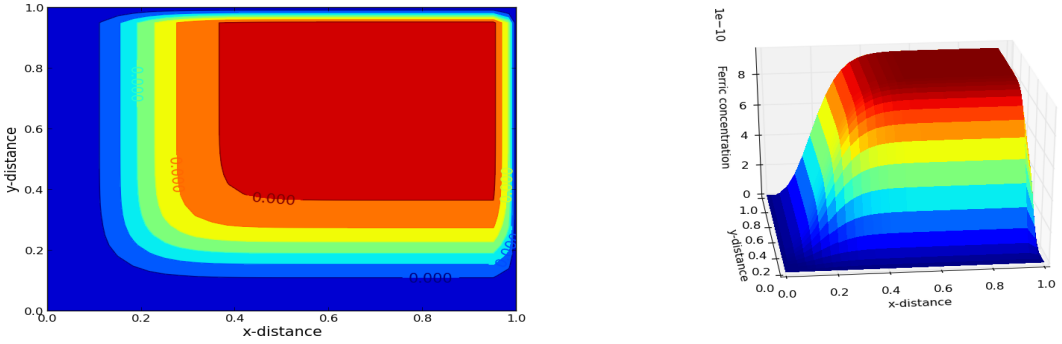

Figure 5.49: Ferric ion distribution, convection-dominated transport.

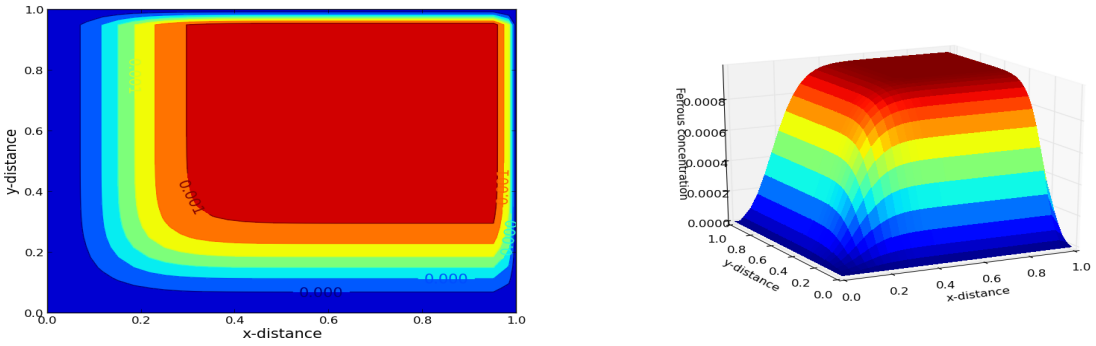

Figure 5.50: Ferrous ion distribution, convection-dominated transport.

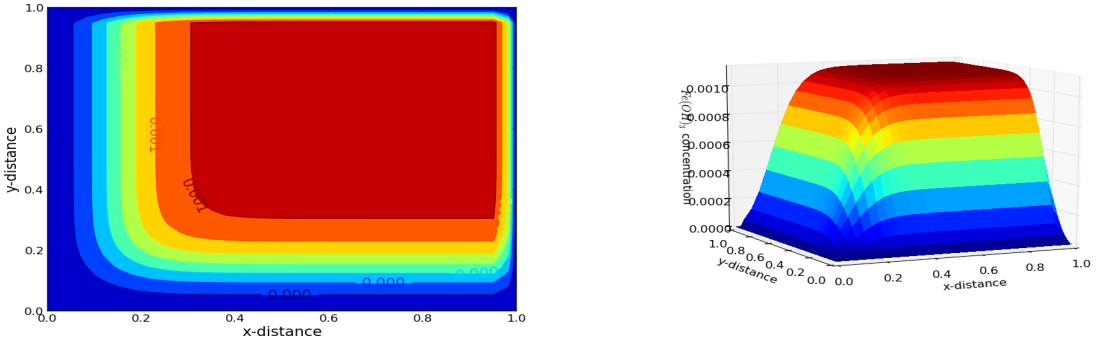

Figure 5.51: Iron hydroxide distribution, convection-dominated transport.

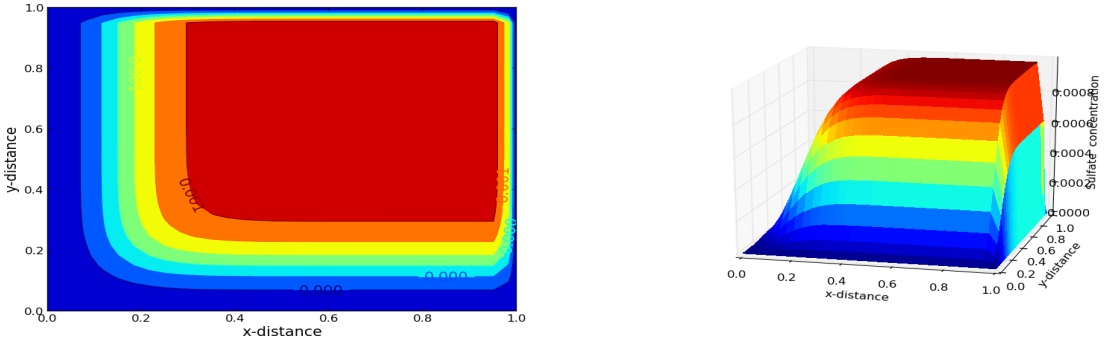

Figure 5.52: Sulfate distribution, convection-dominated transport.

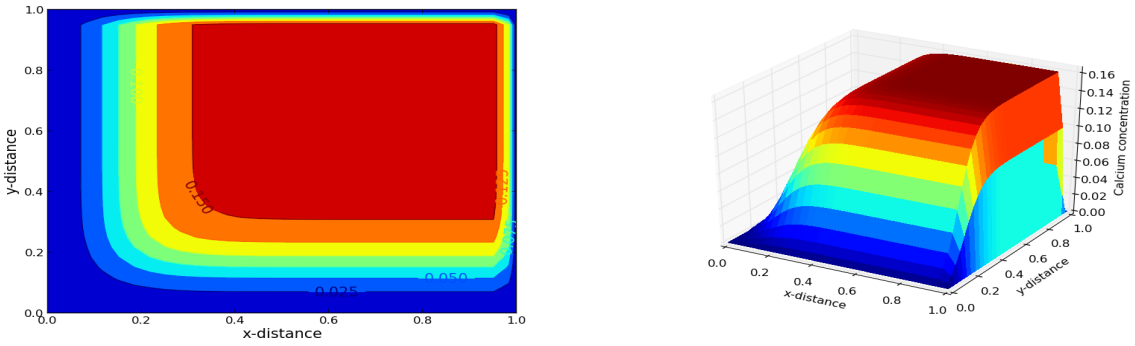

Figure 5.53: Calcium distribution, convection-dominated transport.

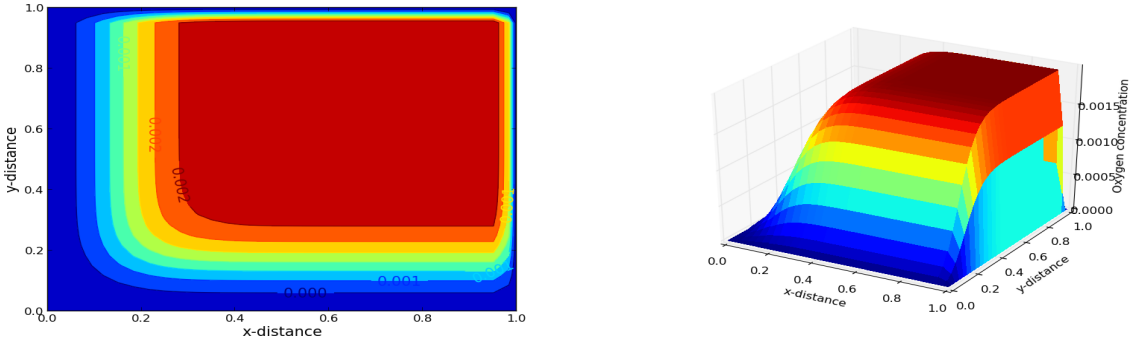

Figure 5.54: Oxygen distribution, convection-dominated transport.

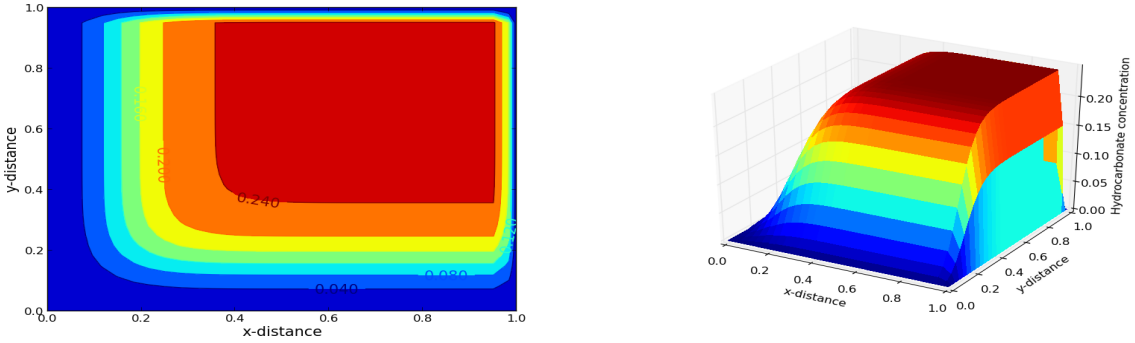

Figure 5.55: Hydro-carbonate distribution, convection-dominated transport.

From Figure 5.48 to 5.55, it can be observed that the unreacted, unfiltered and undispersed species (indicated by the red area in the Figures) is exiting the domain at one corner of the domain. Thus when convection is dominant, a large quantity of the unreacted, unfiltered and undispersed species will exit the domain. The species profiles differ in height, this is attributed to reaction, formation and filtration of the species.

In this section, we present results for a case where dispersion is greater than convection. The velocity was set to $10^{-30}m/min$, dispersion coefficient set to $10^{-2}m^2/min$, and the reaction constants maintained. The distributions of chemical species after 2 min, using a time-step size of 0.1 and a grid cell size of $\frac{1}{25} \times \frac{1}{25}$, are given by Figures 5.56 to 5.63.

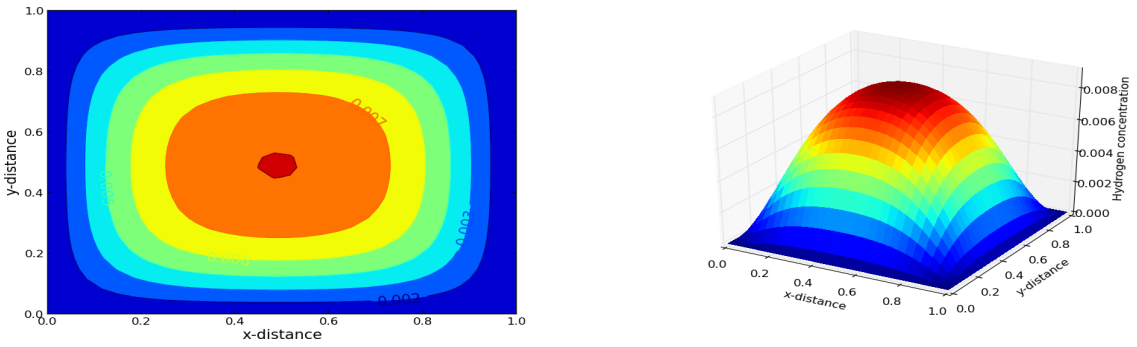

Figure 5.56: Hydrogen ion distribution, dispersion-dominated transport.

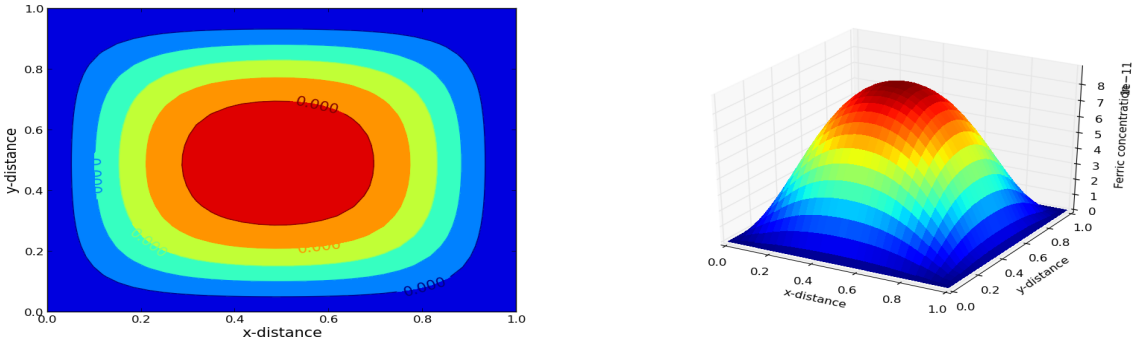

Figure 5.57: Ferric ion distribution, dispersion-dominated transport.

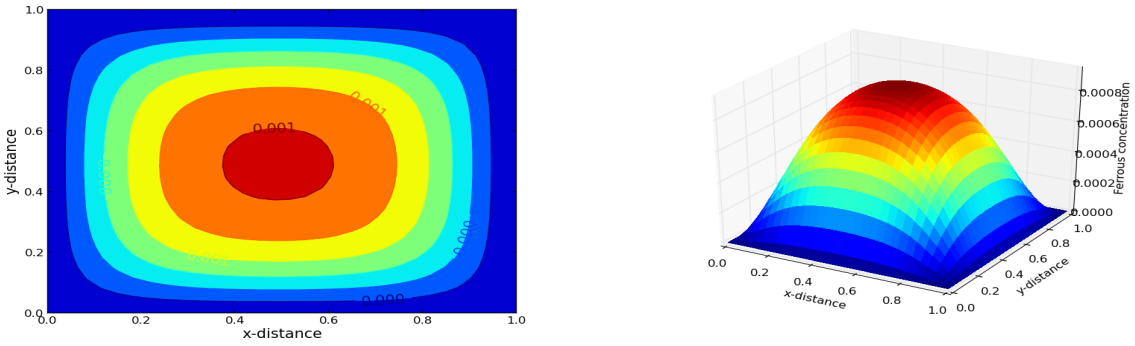

Figure 5.58: Ferrous ion distribution, dispersion-dominated transport.

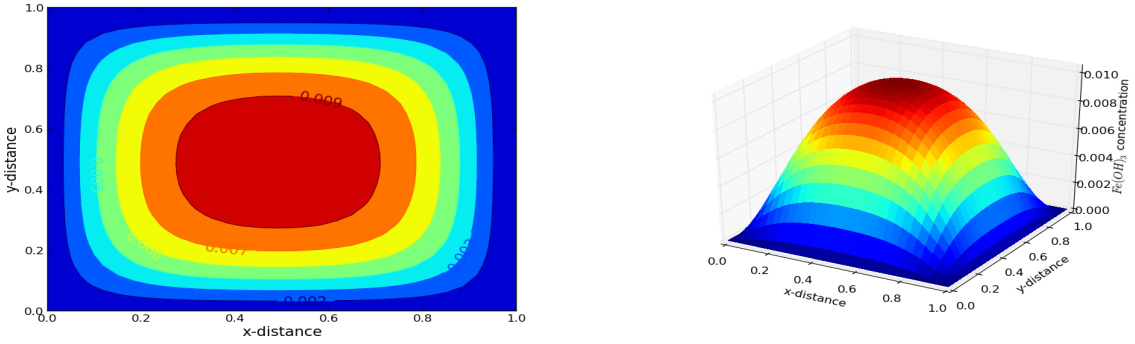

Figure 5.59: Iron hydroxide distribution, dispersion dominated

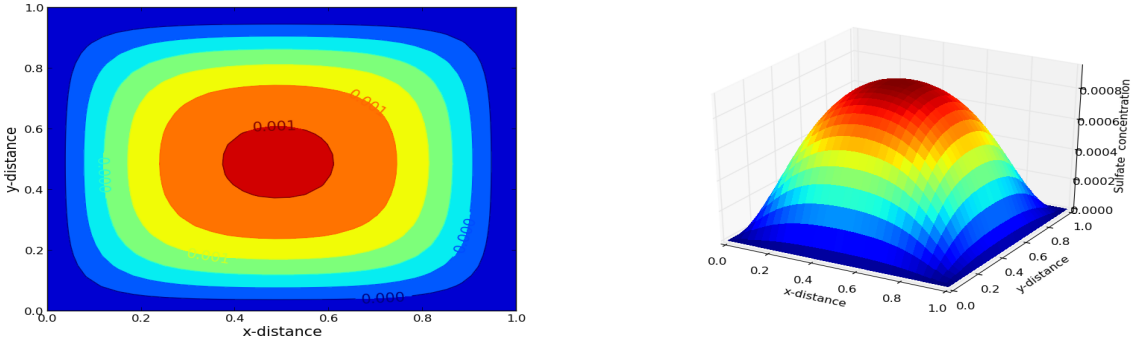

Figure 5.60: Sulfate ion distribution, dispersion-dominated transport.

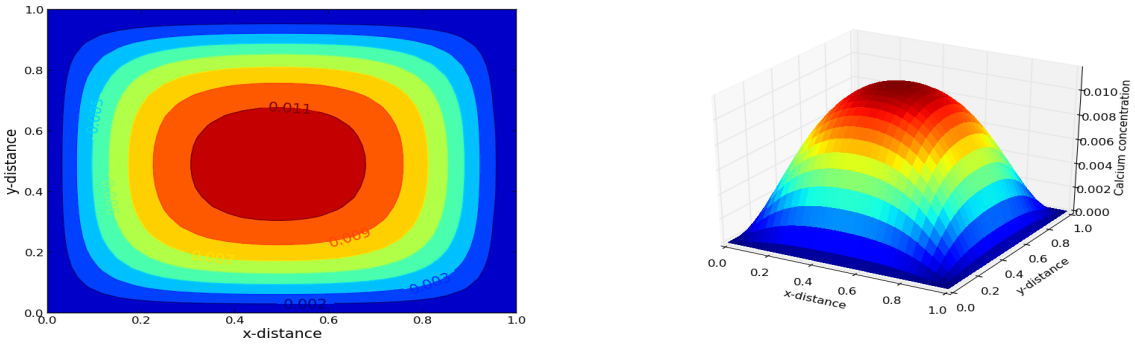

Figure 5.61: Calcium ion distribution, dispersion-dominated transport.

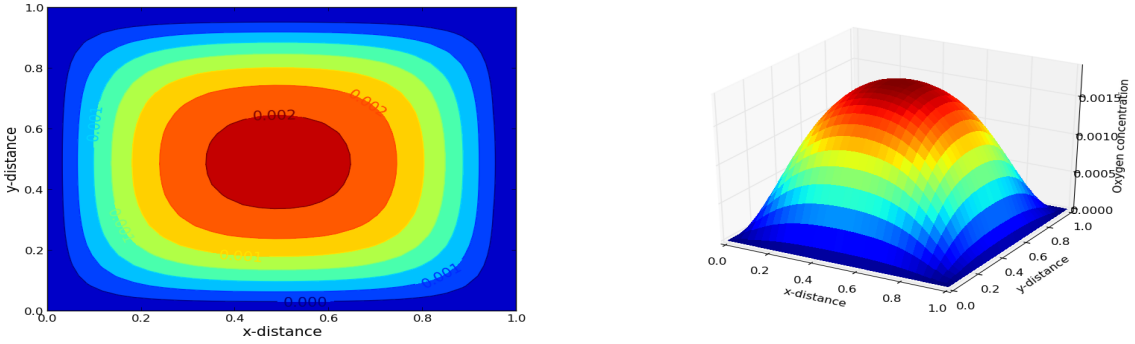

Figure 5.62: Oxygen distribution, dispersion-dominated transport.

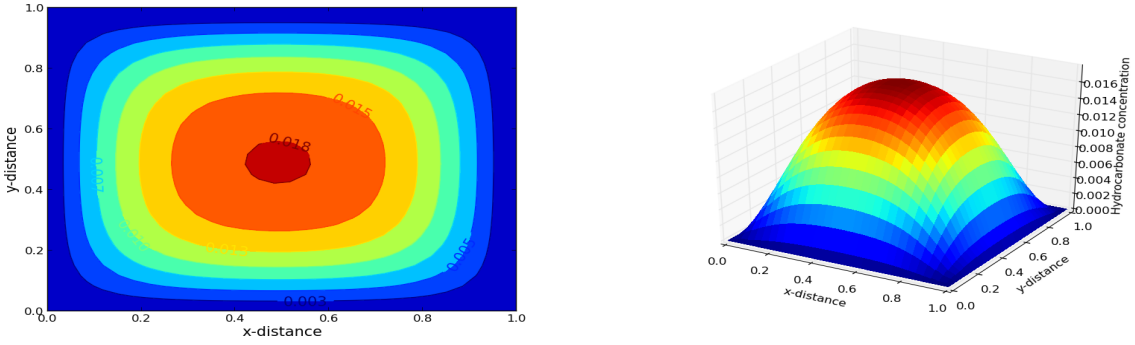

Figure 5.63: Hydro-carbonate ion distribution, dispersion-dominated transport.

The results shown by Figures 5.56 to 5.63 imply that for an isotropic medium and the given boundary conditions, a Gaussian distribution of the species will be obtained. The heights of the Gaussian distribution differ due to reaction, production and filtration of species.

In this section, we present results for a case where dispersion and convection less than the rate of reaction. The velocity was set to $10^{-30}m/min$, dispersion coefficient set to $10^{-30}m^2/min$, and the reaction constants maintained. The distributions of chemical species after 5 min, using a time-step size of 0.5 min and a grid cell size of $\frac{1}{25} \times \frac{1}{25}$, are given by Figure 5.64 to 5.71.

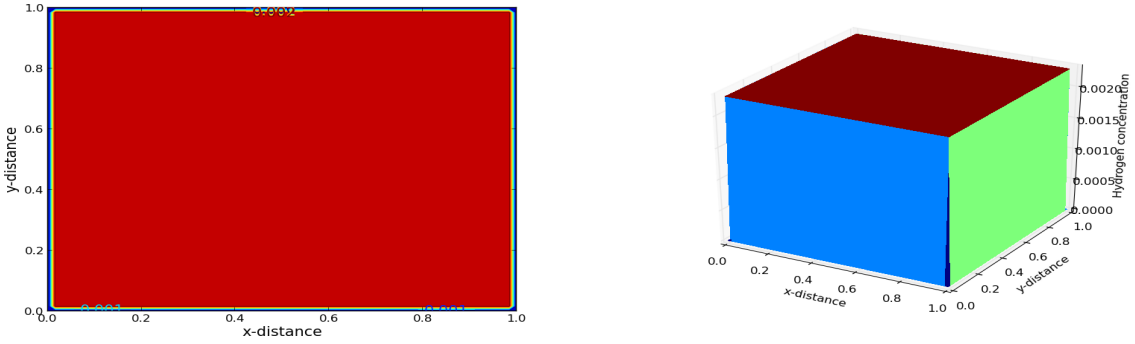

Figure 5.64: Hydrogen ion distribution, reaction-dominated process.

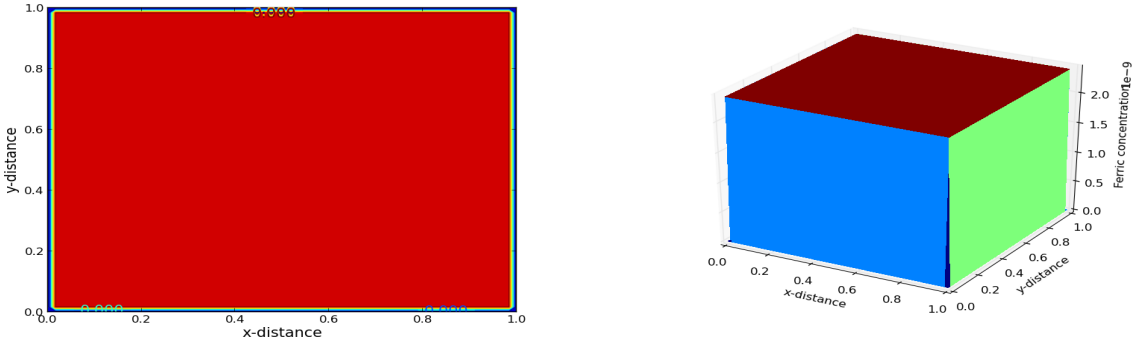

Figure 5.65: Ferric ion distribution, reaction-dominated process.

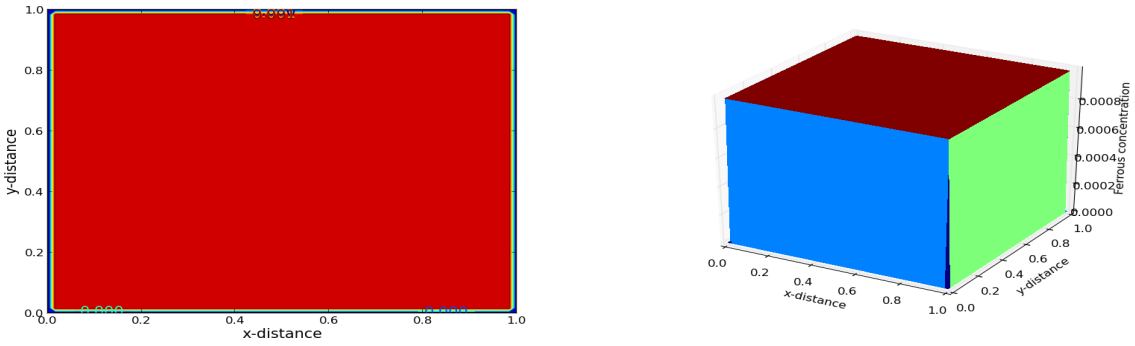

Figure 5.66: Ferrous ion distribution, reaction-dominated process.

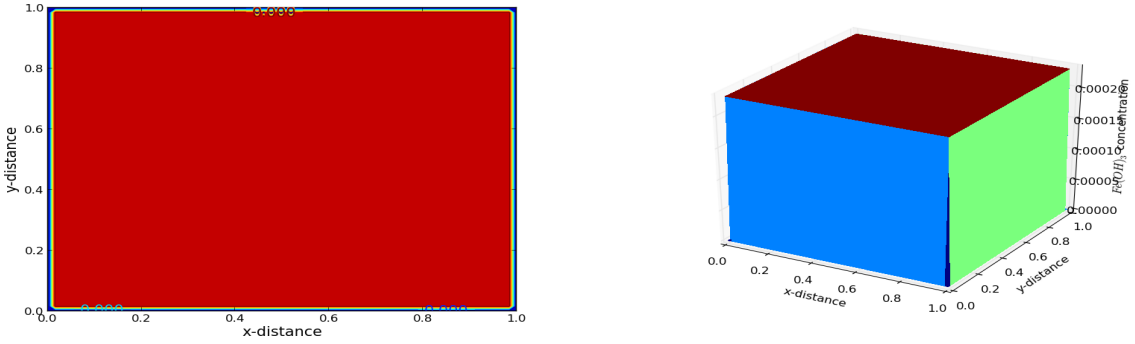

Figure 5.67: Iron hydroxide distribution, reaction-dominated process.

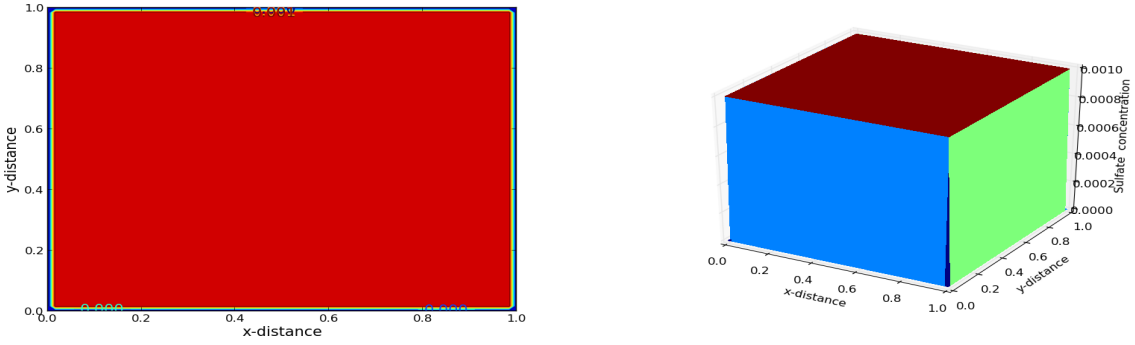

Figure 5.68: Sulfate ion distribution, reaction-dominated process.

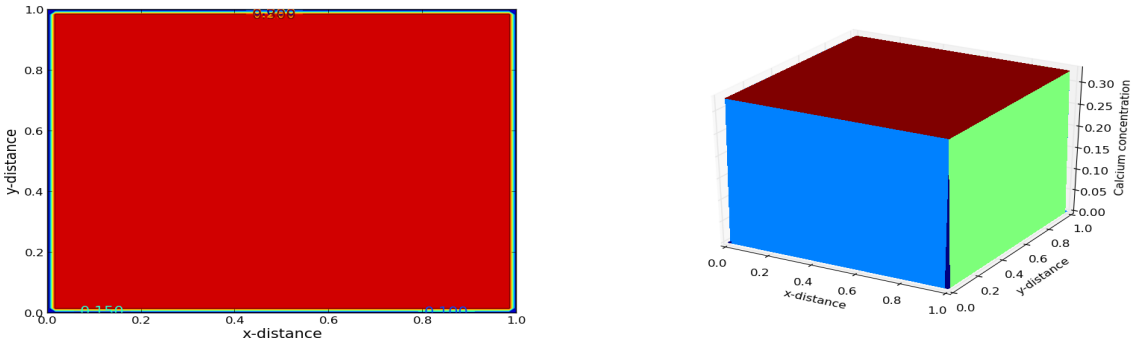

Figure 5.69: Calcium ion distribution, reaction-dominated process.

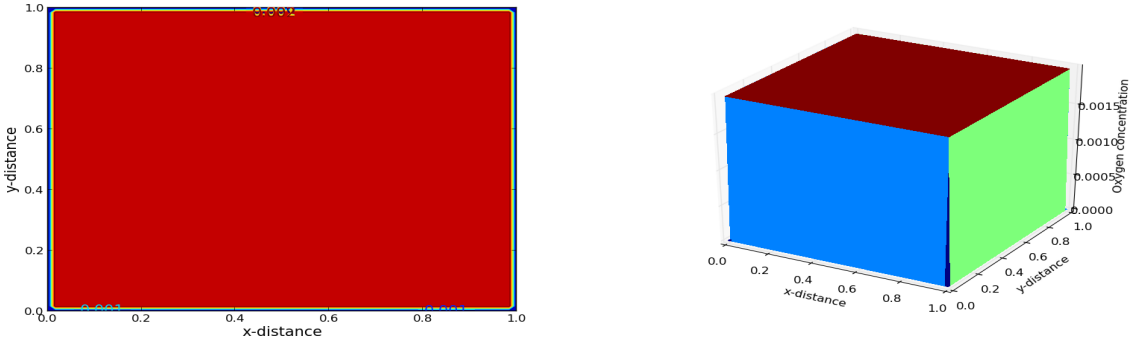

Figure 5.70: Oxygen distribution, reaction-dominated process.

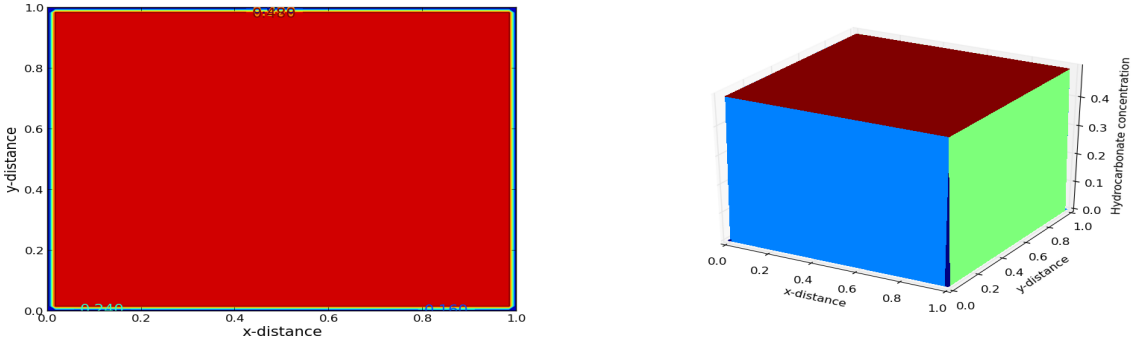

Figure 5.71: Hydro-carbonate ion distribution, reaction-dominated process.

From Figures 5.64 to 5.71, it can be observed that the initial uniform distributions of species have not changed. Thus without convection and dispersion, the initial distributions will be maintained. Comparing the final concentrations of species with their corresponding initial concentrations, it can be observed that the final concentrations are different from the initial concentrations. The observed behaviour is attributed to reactions, production and filtration of species.

5.2.5 Concentration of chemical species with time.

In this section, we present and discuss the results related to changes in concentrations of chemical species with time.

Neutralization implies raising the pH of the effluent water by removing the hydrogen ions. Thus it is expected that the concentration of hydrogen ions decreases in with time in the treatment process. Figure 5.72 shows the concentration of hydrogen ions with time.

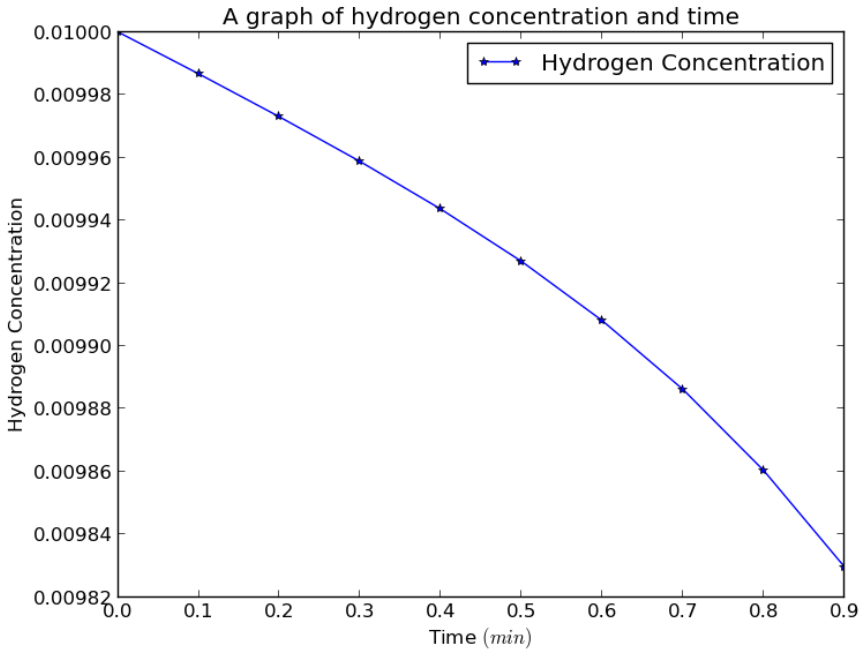

Figure 5.72: Hydrogen ion concentration plotted against time.

The final pH of the water is less than 3.5, this conforms with our earlier assumption.

Figure 5.72 shows the expected behaviour of hydrogen in the treatment method. The graph is not exactly linear because a reversible rate law is used.

Oxidation of ferrous iron implies reduction of ferrous ions. Thus it is expected the that concentration of ferrous ions decrease with time. Figure 5.73 shows the concentration of ferrous ion with time.

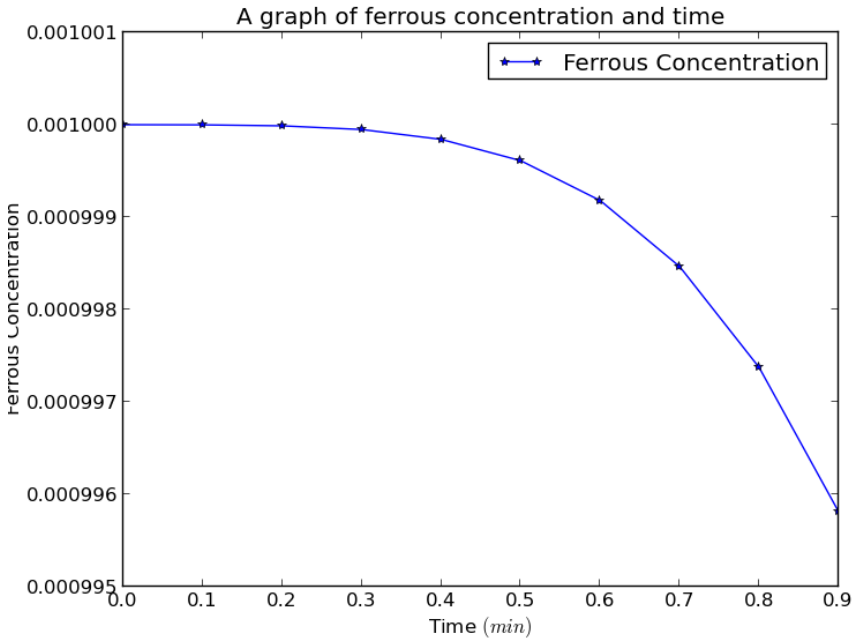

Figure 5.73: Ferrous ion concentration plotted against time.

It can observed that from Figure 5.73 that the concentration of ferrous ion decreases with time.

Filtration of the iron hydroxide implies a reduction in concentration of iron hydroxide with time. Figure 5.74 shows the concentration of iron hydroxide with time.

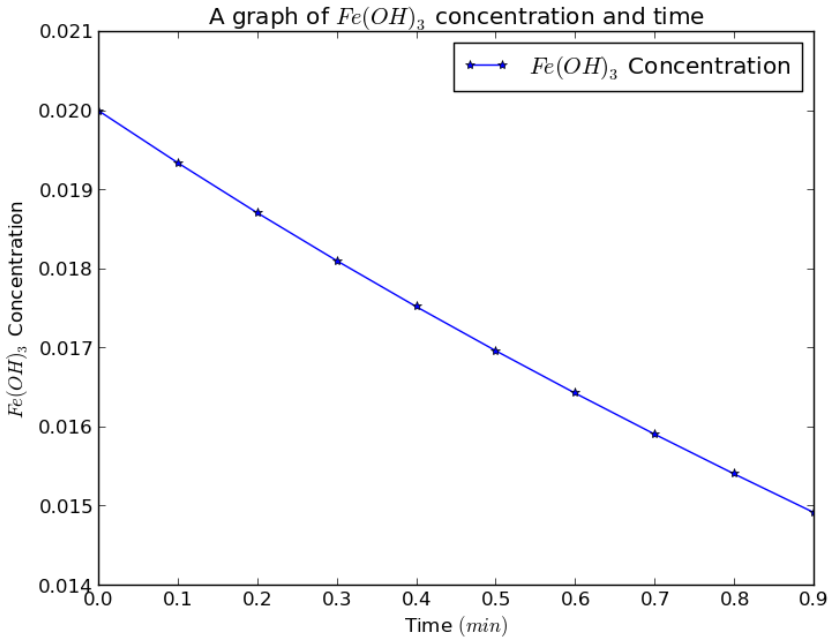

Figure 5.74: Iron hydroxide concentration plotted against time.

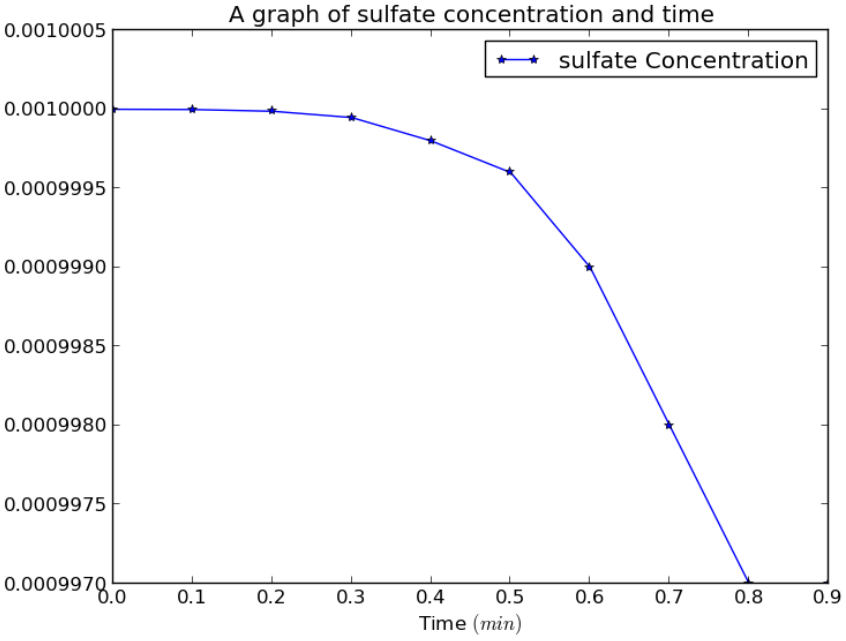

Figure 5.75: Sulfate ion concentration plotted against time.

It can be observed that the concentration of the iron hydroxide decreases with time as expected.

The concentration of sulfate ions is not expected to decrease with time since the ions are neither produced nor reacted. Thus the expected behaviour is a linear. Figure 5.75 shows the concentration of sulfate ions with time. The observed non-linear behaviour is attributed to rounding errors.

Ferric ions are produced in the oxidation of ferrous ion, thus the concentration of ferric ions is expected to increase with time. Figure 5.76 shows the concentration of ferric ions with time.

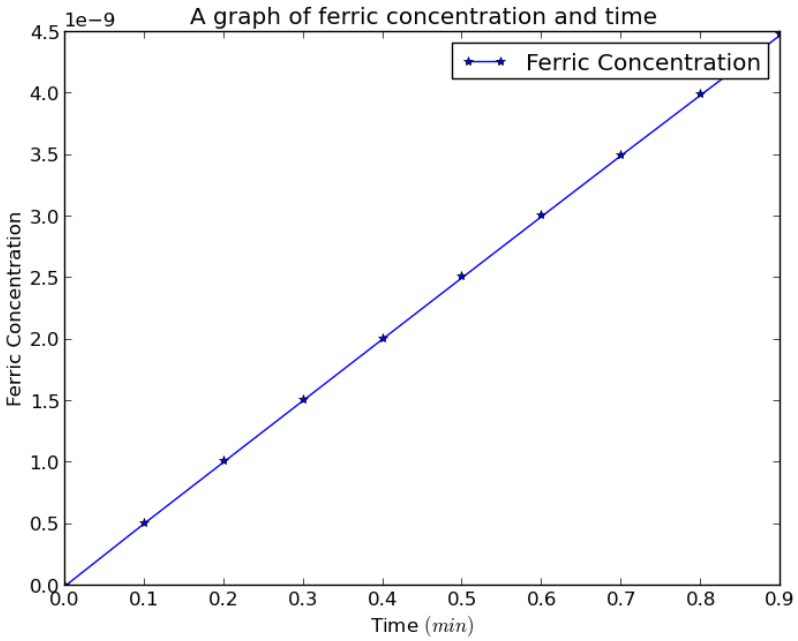

Figure 5.76: Ferric ion concentration plotted against time.

Figure 5.76 shows that the concentration of ferric ions increases linearly with time. The neutralization process involves dissolution of calcite, thus the concentrations of calcium ions and hydro-carbonate ions are expected to increase with time. Figures 5.77 and 5.78 show the concentrations of calcium and hydro-carbonate ions with time.

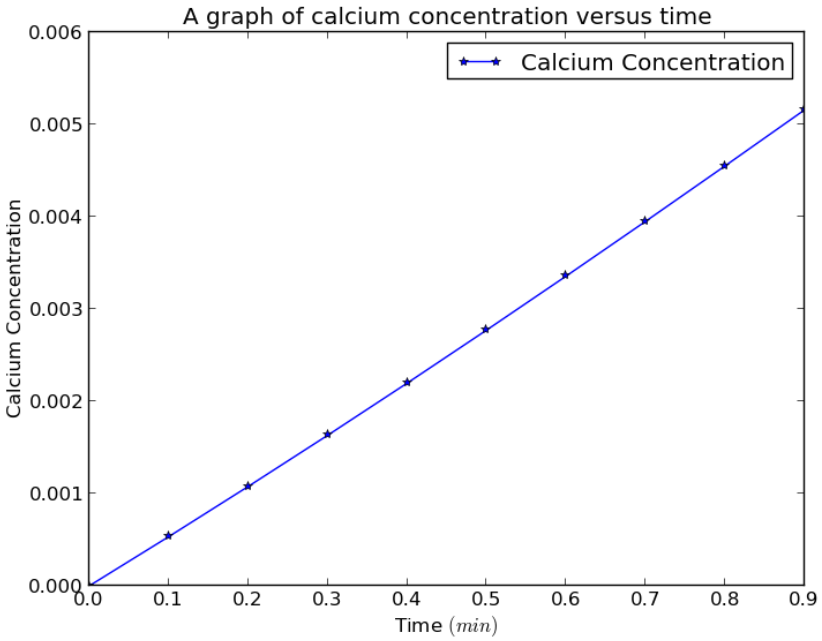

Figure 5.77: Calcium ion concentration plotted against time.

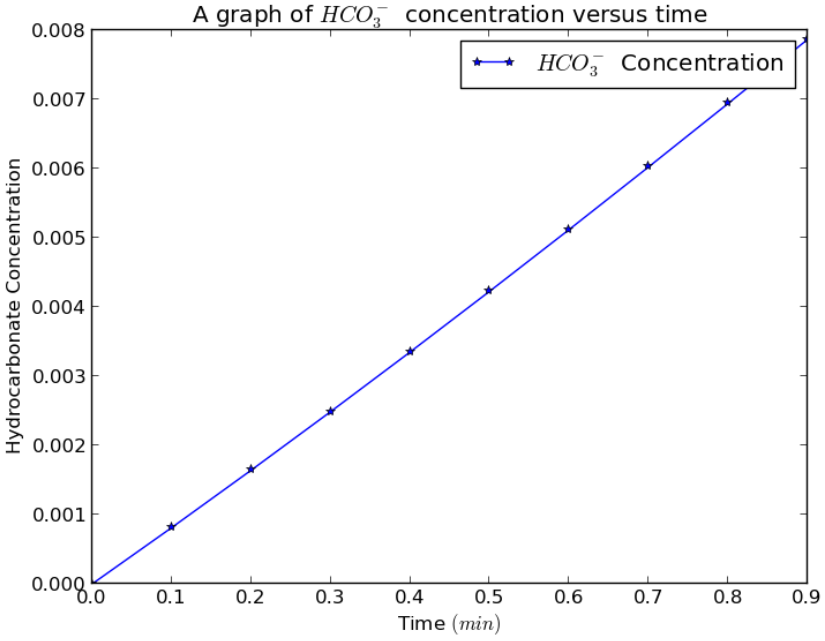

Figure 5.78: Calcium ion concentration plotted against time.

The concentration of oxygen is expected to decrease with time since it take part in the oxidation reaction. Figure 5.79 shows the concentration of oxygen with time.

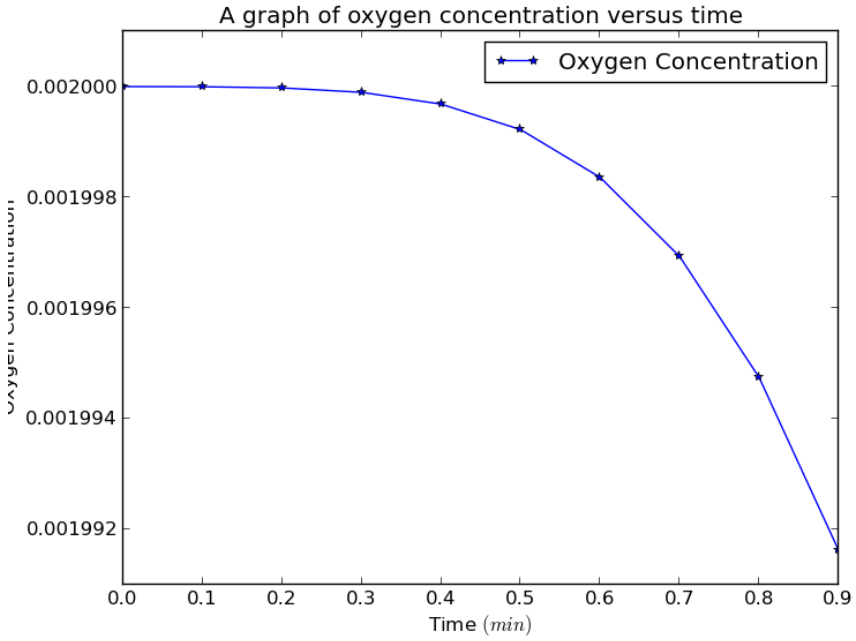

Figure 5.79: Oxygen concentration plotted against time.

In this Chapter, numerical schemes were verified by comparing solutions obtained by the central differencing, upwind and hybrid schemes to an analytical solution. The code used for numerical experiments is validated by three test examples. Numerical experiments are carried out for coupled uniform flow, energy and contaminant transport. The investigations were based on Peclet number. The results from the experiments were discussed.

Chapter 6

Conclusion and recommendation

A passive treatment method called Open Limestone Channnel treatment has been modelled and simulated on a two dimensional domain. The results show that the pH of the effluent water increases with time, the concentration of ferrous ion decreases with time and the iron hydroxide ('yellowboy') decreases with time as expected. There was no significant changes in the initial temperature profile. We suspect this to be due to source term approximation and further investigations are recommended. The results also show that the model can be used to predict information inside the domain unlike other models that do not include spatial information. Thus the open limestone channel treatment is recommended for implementation.

Each numerical scheme was validated and the code used for the numerical experiment was validated by three test examples. We have confidence in our results because we used a validated computer code and verified numerical schemes for simulation/experiment, and all the schemes yielded similar results. Further, the experiments were conducted within the pH limit as stated in our assumptions.

However, the results may not be very accurate due to rounding errors. The model has not been validated due to lack of field and laboratory experimental data. Some of the assumptions are unrealistic and would be relaxed in future modelling studies. The rate laws used in our study are simplified forms of very complicated rate laws, thus our results may not fit well with field data. We will consider more complicated rate laws in future.

The model is a large system of equations, this will be reduced by decoupling techniques in future. Neutralization involves chemical interaction of the solid matrix and interstitial fluid. According to [36], reaction gradients, reaction fronts and mixing zones are the main scenarios that are identified with solid-fluid reactions. We will also investigate these scenarios in future studies.

In summary, a brief discussion on Acid Mine Drainage hazards and the main assumptions used in our modelling studies were given in Chapter 1. Oxidation of pyrite, calcite dissolution, ferrous oxidation, filtration and treatment methods were discussed in Chapter 2. The mathematical model for the open channel limestone treatment was derived in Chapter 3. In Chapter 4, numerical modelling studies were discussed. Verification of numerical schemes and validation of the numerical code (used for our experiments) were discussed in Chapter 5. Finally, we concluded our discussion in Chapter 6. Based on our results, we recommended the open limestone channel treatment method for implementation. We also stated possible research topics for future studies.

Appendix A

Basic Chemistry

A.1 Weathering

Weathering refers to the disintegration or alteration of rocks into products that are compatible with environmental conditions [37]. Rocks are formed deep down the earth's surface under conditions that are very different from conditions in shallow depths, and conditions on the surface of the earth. Thus when rocks from underground are exposed to different conditions due to natural or anthropogenic influences (e.g. erosion and mining), they tend to breakdown physically and chemically [37]. Weathering contributes to many biochemical and geomorphic processes including; formation of soil and supply of nutrients to plants [37]. There are three broad mechanisms involved in the weathering process, these include: chemical, physical and biological processes.

Rocks are aggregates of minerals composed of chemicals Elements. When the chemical composition is altered, then chemical instability occurs in the rock thus resulting in disintegration, this is called chemical weathering. Each of the products of this weathering process has different chemical and mineralogical properties from the parent rock. The products become different from the parent rocks due to chemical changes that occur as a result chemical processes such as; oxidation, reduction, hydrolysis, hydration, carbonation and solution [37].

Physical weathering refers to the mechanical breakdown of rocks. Some of the forces that

cause mechanical weathering are internal and other are external. The stresses from both external and internal sources, exerted on and in rocks destabilizes equilibrium, which may lead to distortion and eventual rapture of rocks. Some of the processes that cause physical weather include: thermal isolation, abrasion, wetting and drying, crystallisation and pressure release [37].

Through some life processes, living organisms also cause weathering of rocks. When weathering occurs as a result of the activities of living organisms, it is known as biological weathering. Many organisms in the soil cause movements among rock particles, which results in the collision of particles, thus making the soil particles to the disintegrate into smaller fragments. An example of biological weathering is when the roots of some plants grow through rocks and force the rock particles to break apart [37].

Weathering of rocks occurs through natural processes and anthropogenic activities. Weathering through anthropogenic activities is the major contributor of environmental hazards. Since rocks are aggregates of minerals, chemical weathering is the major weathering process in rocks. Among the chemical weathering mechanisms, Oxidation is the most common chemical weathering mechanisms identified with chemical metals.

A.2 Chemical kinetics

Chemical kinetics refer to the study of how molecules of substances (reactants) collide and interact to form other substances called products. It involves determining the rate at which the reaction takes place [8, 59].

The rate of a chemical reaction simply refers to the quantity of a reactant consumed or product formed per unit time [8, 53, 59]. For a general chemical equation:

$$aA + aB \longrightarrow products\ (cC) \tag{A.2.1}$$

the rate of reaction (R) is given by:

$$R = -\frac{1}{a}\frac{d[A]}{dt} = -\frac{1}{b}\frac{d[B]}{dt} = \frac{1}{c}\frac{d[C]}{dt}, \tag{A.2.2}$$

where a, b, c are stoichiometric coefficients with respect to reactants A, B, and product C. The symbol $[i]$, is used to denote concentration of the i^{th} chemical species, and the negative (-) implies decreasing reactant concentration. The rate of a chemical reaction is proportional to the rate at which each chemical species is either consumed or formed. However the individual chemical species react in different stoichiometric proportions, thus the rate of reaction of each chemical species in the system is multiplied by the inverse of its stoichiometric number as indicated in Equation A.2.2 [8, 53, 59, 16, 30]. Thus the rate of a chemical reaction is given by the weighted rate of reaction of each chemical species.

However, the rate of a reaction is related to the concentrations of the reactants by a principle called mass action [8, 53, 59]. When the principle of mass action is applied to determine the rate of a reaction, the resulting equation is called rate law [8, 53, 59]. For the general chemical equation given above (Equation A.2.1), the rate law is given by:

$$R = K[A]^{ox}[B]^{oy}, \tag{A.2.3}$$

where K is a constant called the rate constant which depends on temperature, concentration, surface area and pressure. The indices ox, oy are called orders of the reactants A and B respectively [8, 53, 16, 30]. The sum of all the orders of the reactants is called order of the reaction [8, 53, 16, 30]. The orders of the chemical species can only be determined by Laboratory experiment [8, 53, 16, 30, 59].

Many reactions do not occur in a single reaction step, a sequence of steps or reactions by which an overall reaction occurs is called a reaction mechanism [8, 53]. Each of the steps is called an elementary reaction and has its own rate law [8, 53]. The products formed in each elementary reaction that also become reactants in subsequent reaction steps, but do not appear in the overall reaction are called intermediates [8]. Among these reactions, the slowest reaction step limits the overall rate of reaction, as a result, the overall rate of reaction is determined by that elementary reaction, this rate-limiting elementary reaction is called rate-determining step [8, 53, 16, 30].

In a reaction mechanism, if the rate-determining step is the first elementary reaction, then the overall rate of reaction is simply equal to the concentration of the reactants in that elementary reaction, raised to their respective orders [8, 53, 16, 30]. Otherwise,

all the reaction intermediates in the rate law have to be substituted with appropriate non-intermediates [53, 8].

According to [59], the basic unit of any chemical process is the elementary reaction. Since an elementary reaction occurs due to molecular events, all the physical factors (including temperature, pressure and ionic strength) affecting molecular motion also affect the elementary reaction [59]. The physical factors affect elementary reaction through the rate constant. The *Activated Complex Theory (ACT)* also known as *Transition State Theory (TST)* was developed to study the relationship between physical factors and elementary reactions [59].

Ions are chemical reacting species with charges. These charges interact electrostatically with each other in a solution, which may affect the availability of the ion for reaction. As a result of the electrostatic interaction, the effect concentration of the ion is specially called activity. The activity and concentration are proportional to each other, the constant of proportionality is called activity coefficient. Mathematically the relationship between activity (a_i) and concentration (C_i) on ion (i) is given by:

$$a_i = \eta_i C_i \tag{A.2.4}$$

where η is the activity coefficient which depends on pressure and temperature. When the solution is dilute, the activity coefficient is taken as one, due minimal interaction ions.

A collection of elementary reactions (a mechanism) that is describes a full chemical process may be classified as parallel, series or reversible reactions [59]. A parallel system of elementary reactions is a chemical process in which, one reactant is common to all the elementary reactions. When the products formed by one elementary reaction are reactants in the next step of the mechanism, then the elementary reactions are in series. A reversible system describes a chemical process where the products formed by an elementary reaction, undergo reaction to form the reactants of that same elementary reaction.

A.3 Pyritic oxidation

According to [50, 47], the chemical oxidation of Pyrite is described by three steps such as: oxidation of Pyrite to sulphate and ferrous iron by molecular oxygen; oxidation of ferrous iron to ferric iron by molecular oxygen; and the oxidation of ferric iron to sulphates and ferrous iron.

Electrochemical oxidation of pyrite has been described by [50] as reactions involving anodic and cathodic reactions on the Pyrite's surface. It is stated in [50] that the mechanism for the electrochemical oxidation process is not well known, this statement is supported by [15, 55]. The elementary reactions that are involved in the electrochemical oxidation processes are complicated by the reaction environment [15, 55]. In red-ox reactions the elementary steps involve transfer of a single electron at a time. This implies that, monosulphite minerals (e.g. Gelena, Sphalerite) requires eight elementary steps to release a sulphate, and disulphite minerals (e.g. Pyrite and Marcasite) require seven steps [15, 55]. Pyrite is a semiconductor, which implies that electrons can migrate from one site to another on the mineral's surface, this implies that reactions can occur at different sites, thus it is very difficult to provide a consistent description due to the randomness of events [15, 55]. The semiconductor properties critically depend on the composition of the Pyrite sample, or the region or zone of the sample [15]. According to [15], the electrochemical oxidation of Pyrite occurs in three broad steps including: cathodic reaction, electron transfer and anodic reaction.

When an aqueous species (oxidant) accepts electron on the surface of the mineral, the reaction is cathodic [15]. Natural oxidants include O_2 and Fe^{3+}, which oxidise Pyrite in reactions described by the following chemical equation [15]:

$$FeS_2 + 3.5O_2 + H_2O \rightleftharpoons Fe^{2+} + 2H^+ + 2SO_4^{2-} \tag{A.3.1}$$

and

$$FeS_2 + 14Fe^{3+} + 8H_2O \rightleftharpoons 15Fe^{2+} + 16H^+ + 2SO_4^{2-}. \tag{A.3.2}$$

The chemical Equations A.3.1 and A.3.2 are balanced overall chemical reactions that occur in several elementary steps [15]. According to [15], Sulphur is the reducing agent instead of iron (ferrous ion).

A.4 Transport mechanisms for particle removal

Filtration mechanism refers to all the physical processes that result in filtration due. Some of the physical processes include; straining, interception, inertia, sedimentation, and orthokinetic flocculation [64, 6, 43].

The first and most common transport mechanism is straining. When a porous material is placed in a flowing fluid, due to larger size of suspended particles relative to the pore size of the material, the suspended particles (or solutes) are trapped on the surface of the material. If all the solutes in the solution are larger than the pore sizes, then no particle would be able to go through the material surface, but are trapped on the surface of the material like a mat [64, 6, 43].

Solid grains or struts are sometimes in the radii of the advecting solutes, thus the advecting particles come to a halt when in contact with solid grains or struts. This is referred to as filtration by interception [64, 6, 43].

During fluid flow through the porous material, some particles are streamlined with the solid grains of the material. The streamlines diverge at the point of contact with the solid grains, however, if the advecting particles have sufficient inertia, the particle trajectory remain unchange, thus resulting in a collision and coalition with the solid grains. This filtration mechanism is referred to as inertia [64, 6, 43].

Another important filtration transport mechanism is sedimentation. Due to larger density of particles, the gravitational force acting on the particles is greater than the surface tension, thus the solute particles are subjected to a velocity (in response to resultant force) relative to the motion of the fluid until the resultant force is neutralize [64, 6, 43].

Appendix B

Transport Parameters

A uniform flow is coupled with the chemical species transport equations. Table B.1 contains the data, used to obtain the concentration profiles for the chemical species and temperature.

Parameter	**Numerical value**	**Unit of measurement**
Domain	$(0,1) \times (0,1)$	m^2
Specific heat capacity (limestone)	0.908 [5]	J/gK
Porosity	0.2 [5]	
Density of limestone	2.3 [5]	g/cm^3
Thermal conductivity of limestone	1.26 [5]	W/mK
Specific heat capacity water	1.996 [5]	J/gK
Density of water	1 [5]	g/cm^3
Thermal conductivity of water	0.016 [5]	W/mK
Deposition rate constant	6.4×10^{-3}	m/min
Dissolution rate constant	10^{-4}	m/min
Precipitation rate constant	2.5×10^{-9}	m/min
Ferrous oxidation rate constant	2.5×10^{-5}	m/min
Grain diameter	0.3	m
Colloid radius	0.000015	m
a_1, a_2, a_3	$4, 3.308, 1.4069$ [44]	
θ_{max}	0.345	

Table B.1: Parameters used to obtain concentration and temperature profiles.

List of References

[1] Braley S. A. Research summary report on fellowship. Technical report, Mellon Institute, 1953.

[2] Nimick D. A. and Moore J. N. Stratigraphy and chemistry of sulfidic flood-plain sediments in the upper clarke valley, montana. *American society symposium series*, 292:139–152, 1994.

[3] Williamson M. A. and Rimstidt. The kinetics and electro-chemical rate determining step of aqueous pyrite oxidation. *Geochimica et Cosmochimica Acta*, 58:5443–5454, 1994.

[4] U. S. Environmental Protection Agency. Technical document: Acid mine drainage prediction. Technical report, Environmental Protection Agency, Office of Solid Waste, Special Waste Branch, 401 M Street, SW Washington, DC 20460, 1994.

[5] Alden Andrew. Densities of common rock types, 2013. http://geology.about.com/cs/rock-types/a/aarockspecificgravity.htm.

[6] aquavarra.ie/Utbkpdf/chap6.pdf. Particle removal by filtration processes, August 2012. http://www.aquavarra.ie/Utbkpdf/chap6.pdf.

[7] Jacob Bear. *Dynamics of Fluids in porous Media*. Dover Publications, Department of Civil Engineering, Technion-Isreal Institute of technology , Haifa, 1988.

[8] Capellos C. and Bielski B. H. J. Kinetic systems, mathematical description of chemical kinetics in solution. 1972.

[9] Hustwit C. C., Ackman T. E., and Erickson P. M. Role of oxygen transfer in acid mine drainage treatment. Technical report, United States Department of interior Bureau of Mines, 1992.

[10] Singer P. C. and Stumm W. Acidic mine drainage, the rate determining step. *Science*, 167:1121–1123, 1970.

[11] C.F. Conaway. *The Petroleum Industry: A Nontechnical Guide*. PennWell Nontechnical Series. PennWell Publishing Company, 1999.

[12] Arthur T. Corey. *Mechanics of heterogeneous fluids in porous media*. Water resource publications, Water resource publications, Colorado 80522, 1977.

[13] Ardejani F. D., Baafi E., Panahi K. S., Singh R. N., and Shokri. Application of computational fluid dynamics (cfd) for simulation of acid mine drainage generation and subsequent pollutant transportation through groundwater flow systems and rivers. pages 17–23.

[14] Kupka D. and Skvarla J. Kinetics of chemical oxidation of ferrous iron by oxygen in acid sulphate solution. 2013.

[15] Rimstidt J. D. and Vaughan D. J. Pyrite oxidation a state-of-the-art assessment of the reaction mechanism. *Geochimica et Cosmochimica Acta*, 67:873–880, 2003.

[16] Langmuir Donald. *Aqueous Environmental Geochemistry*. Prentice-Hall, Inc., Colorado School of mines, 1997.

[17] Jean G. E. and Bancroft G. M. An xps and sem study of gold deposits at low temperature on sulphite minerals. *Geochimica et Cosmochimica Acta*, 49:979–987, 1985.

[18] Smith E. E. and Shumate K. S. Water pollution control research series. Technical report, U. S. Department of interior, 1970.

[19] Sozer E. and Shyy W. Modelling of fluid dynamics and heat transfer through porous media for liquid rocket propulsion. Technical Report AIAA 2007-5549, University of Michigan, Ann Arbor, MI, 4819, July 2007.

[20] Saracusa L. Emily. A mathematical model for acid mine drainage removal and hydroxide crust formation. Technical report, 2011.

[21] Anderson Greg. *Thermodynamics of Natural Systems*. Cambridge University Press, New York, 2005.

[22] Ennaoui A. Fietchter S. Jaegermann W. Trbutsch H. Photochemistry of highly quantum efficient single-crystalline $n - fes_2$ (pyrite). *Journal of the electrochemical society*, 133:97–106, 1986.

[23] Appelo C. A. J. and Schafer. A hydrogeochemical transport model for an oxidation experiment with pyrite/calcite/organic matter containing sand. *Elsevier Science Ltd.*, 13:257–268, 1998.

[24] Bear J. and Bachmat Y. A generalized theory on hydrodynamic dispersion in porous media. *I. A. H. S. symposium*, 72:7–16, 1967.

[25] Fripp J., Ziemkiewicz P. F., and Charkavork H. Acid mine drainage treatment. Technical Report ERDC TN-EMRRP-SR-14, U. S. Army Engineer research and development center, Vicksburg, MS., 2000. www.wes.army.mil/el/emrrp.

[26] Yogesh Jaluria. *Natural convection Heat and Mass transfer*. Pergamon Press, Department of Mechanical Engineering, Indian Institute of Technology, Kanpur, India, 1980.

[27] Hubbert M. K. Darcy law and the field equations for the flow of underground fluids. 207:222–239, 1956.

[28] Versteeg H. K. and Malalasekera W. *An introduction to Computational fluid Dynamics: The finite Volume Method*. Pearson Prentice Hall, 2007.

[29] Tsutomu Kambe. *Elementary Fluid Mechanics*. World Scientific Publishing Co. Pte. Ltd., 2007.

[30] VENIAMIN G. LEVICH. *PHYSIOCHEMICAL HYDRODYNAMICS*. Prentice-Hall, Inc. Englewood Cliffs, N. J., 1962.

[31] William Lowrie. *Fundamentals of Geophysics*. Cambridge University Press, 2007.

[32] Bakken B. M., Hochella M. F., Marshall A. F., and Turner A. M. High resolution microscopy of gold in unoxidized ore from the carlin mine. *Geochimica et Cosmochimica Acta*, 84:171–179, 1989.

[33] Eggleston C. M., Ehrhardt J., and Werner S. Surface structural controls on oxidation kinetics : An xps-ups, stm, and modeling study. Technical report, Lawrence Livermore National Laboratory, Calfornia, Universite Mixte de Recherche France, Swiss Federal institute of Technology, 1996.

[34] Garrels R. M. and Thompson M. E. Oxidation of pyrite by iron sulphate solution. *American Journal of Science*, 258:57–67, 1960.

[35] Kays W. M. *Convective Heat and Mass Transfer*. McGraw-Hill, Inc., 1966.

[36] Phillips Owen M. *Geophysical fluid dynamics sub-surface flow and Reactions*. Cambridge University Press, 2009.

[37] Pidwirny M. and Scott J. "weathering" fundamentals of physical geography, 2006. http://www.physicalgeography.net/fundamentals/10r.html.

[38] Reddy M. M., Plummer L. N., and Busenberg E. Crystal growth of calcite from calcium bicarbonate solution at constant p_{CO_2} and 25^oc : a test of calcite dissolution model. *Geochimica et Cosmochimica*, 45:1281–1289, 1981.

[39] Buckley A. N. and Woods R. The surface oxidation of pyrite. *Applied surface Science*, 27:437–452, 1987.

[40] Moore J. N. and Luoma S. N. Hazardous waste from large-scale metal extraction. Technical report, 1990.

[41] Nikolaevski V. N., Gorbunov A. T., and Zotov G. A. Mechanics of saturated porous media. 1970.

[42] Plummer L. N., Wigley T. M., and Parkhurst D. L. The kinetics of calcite dissolution in co_2- water systems at 5^oc to 60^oc and 0.0 to 1.0 atm co_2. *American Journal of Science*, 278:179–216, 1978.

[43] Pontikakis G. N., Koltsakis G. C., and Stamatelos A. M. A mathematical model for the dynamics of particulate filtration in diesel foam filters. *Particulate Science and Technology*, 173:179–200, 2007.

[44] Sun N., Elimelech M., Ne-Zheng S., and Ryan J. N. A novel two-dimensional model for colloid transport in physically and geochemically heterogeneous porous media. *Contaminant Hydrology*, 49:173–199, 2001.

[45] Barton P. The acid mine drainage. in j. o. nriagu, ed. sulphur in the environment part ii. ecological impacts. *Wiley InterScience, Newyork*, pages 313–358, 1978.

[46] Baveye P. and Sposito G. The operational significance of the continuum hypothesis in the theory of water movement through soils and aquifers. *Water resource*, 20:521–530, 1984.

[47] Chandra A. P. and Gerson A. R. The mechanisms of pyrite oxidation and leaching: a fundamental perspective. *Elsevier*, 65:293–315, 2004.

[48] Plessis J. P. and Masliyah J. H. Mathematical modelling of flow through consolidated isotropic porous media. pages 145–161, 1988.

[49] Ziemkiewicz P., Skousen J., and Lovett R. Open limestone channels for treating acid mine drainage : A new look at an old idea. Technical report, West Virginia University, 2013.

[50] Zheng C. Q., Allen C. C., and Bautista R. G. Kinetic study of the oxidation of pyrite in aqueous ferric sulfate. Technical report, Ames Laboratory USDOE, Mining and mineral resource research institute, Department of Chemical Engineering, Iowa State University, 1986.

[51] Bird B. R., Stewart W. E., and Lightfoot E. N. *Transport Phenomena*. John Wiley and Sons, Chemical Engineering Department, University of Wisconsin-Madison, second edition, 2002.

[52] Kriegman-King M. R. and Reinhard M. Transformation of carbon tetrachloride by pyrite in aqueous solution. Technical report, 1994.

[53] Cheng Raymond. Physical chemistry with applications to biological systems. 1977.

[54] Garland Rebecca. Acid mine drainage: the chemistry. Report, Senior Researcher, CSIR Pretoria., 2012.

[55] Karthe S. and Suoninen E. Oxidation of pyrite surfaces: A photochemical spectroscopic study. *Applied surface Science*, 72:157–170, 1993.

[56] Phongthanapanich S. and Dechaumphai P. Finite volume method for convection-diffusion-reaction equation on triangular meshes. *John Wiley and Sons*, 26:716–727, 2008.

[57] Prager S. Viscous flow through porous media. *Physical fluids*, 4:1477–1482, 1968.

[58] Werner S. and Lee F. G. Oxygenation of ferrous iron. *American Chemical Society*, 53:143–146, 1961.

[59] Werner S. and James J. M. *Aquatic Chemistry: An introduction emphasizing chemical equilibria in natural waters.* WILEY-INTERSCIENCE, Harvard University and California Institute of Technology, 1970.

[60] F. W. Schwartz and H. Zhang. *Fundamentals of ground water.* John Wiley and sons, The Ohio State University, 2003.

[61] Geological Survey. U. s. geological survey water-supply paper issues. Report, Department of Geological Survey, 1988.

[62] Lowson R. T. Aqueous oxidation of pyrite by molecular oxygen. *Chemical reviews*, 82:461–497, 1982.

[63] Ramontja T. Mine water management in the witwatersrand gold fields with special emphasis on mine drainage. Technical report, The Council for Geoscience, Department of Water Affairs, Department of Mineral Resource Mintek, Water Research Commission, 2010.

[64] Jegatheesan V. and Vigneswaran. Mathematical modelling of deep bed filtration. 2012.

[65] Patankar Suhas V. *Series in computational methods in mechanics and thermal Sciences: Numerical Heat Transfer and Fluid Flow.* Hemisphere Publishing Corporation, 1980.

[66] Calmano W., Forstner U., and Hong J. Mobilization scavenging of heavy metals following re-suspension of anoxic sediments from the elbe river. *American society symposium series*, 550:298–321, 1994.

[67] Morse J. W. Release of toxic metals via oxidation of authigenic pyrite in resuspended sediments. *American Chemical Society symposium series*, 550:289–297, 1994.

[68] Bachmat Y. Spatial macroscopization of processes in heterogeneous systems. 10:391–403, 1972.

[69] Bachmat Y. and Bear J. Macroscopic modelling of transport phenomena in porous media 1: the continuum approach. *D. Reidel publishing company*, pages 213–240, 1986.

[70] Bachmat Y. and Bear J. Macroscopic modelling of transport phenomena in porous media 2: Application to mass, momentum and energy transport. pages 241–269, 1986.